

A HYBRID PLATFORM FOR WIDEBAND RECONFIGURABLE NONLINEAR METAMATERIALS

A Dissertation
Presented to
The Academic Faculty

by

Muliang Zhu

In Partial Fulfillment
of the Requirements for the Degree
Doctor of Philosophy in the
School of Electrical and Computer Engineering

Georgia Institute of Technology
December 2022

COPYRIGHT © 2022 BY MULIANG ZHU

A HYBRID PLATFORM FOR WIDEBAND RECONFIGURABLE NONLINEAR METAMATERIALS

Approved by:

Dr. Ali Adibi, Advisor
School of Electrical and Computer
Engineering
Georgia Institute of Technology

Dr. Benjamin D.B. Klein
School of Electrical and Computer
Engineering
Georgia Institute of Technology

Dr. Stephen E. Ralph
School of Electrical and Computer
Engineering
Georgia Institute of Technology

Dr. Hayk Harutyunyan
Department of Physics
Emory University

Dr. Phillip N. First
School of Physics
Georgia Institute of Technology

Date Approved: November 29, 2022

*To my beloved parents, Xiang Zhu & Haiping Xie, maternal grandmother, Chunying Liu,
and in memory of my paternal grandparents, Fosheng Zhu & Huilan Fan,
my maternal grandfather, Chengxuan Xie.*

谨以此文献给我敬爱的父母朱翔和谢海萍，外祖母柳春英；
怀念我的祖父母朱佛生和范惠兰，外祖父谢承玄。

ACKNOWLEDGEMENTS

I would like to express my deepest and cordial gratitude to my advisor, Prof. Ali Adibi, for his endless support and encouragement in my Ph.D. studies at Georgia Tech. He trusted my potential in research and gave me abundant freedom to explore and grow as an independent thinker. On the other hand, he always inspired me with insightful advice when I could not resolve a difficulty. And he taught me numerous skills not only as a researcher on the state of the art, but also as a good presenter and writer. I believe these qualities will be of great help to my career in the future.

I would also like to thank my thesis committee members, Prof. Benjamin D.B. Klein, Prof. Stephen E. Ralph, Prof. Hayk Harutyunyan, and Prof. Phillip N. First, for their willingness to serve on the committee and their time examining my thesis and presentation. Moreover, I am extremely grateful to Prof. Gee-Kung Chang and Prof. Klein who served as my dissertation proposal committee members, reviewed the proposal, indicated defects of the proposal presentation, and offered many helpful suggestions toward this thesis.

I am indebted to Sajjad Abdollahramezani and Dr. Tianren Fan for being most supportive senior fellows to me throughout my Ph.D. journey, that I would frequently discuss novel research observations and the obstacles encountered with. They are very knowledgeable and generous. It has been my great pleasure to study with them, and I have been fortunate learning from their creativity and problem-solving skills. I am also thankful to Dr. Xi Wu and Mohammadreza Zandehshahvar for their generous support in various aspects that I have been lucky to learn useful skills from them and enjoy fruitful discussions with them. I have been fortunate to discuss with and learn from many other excellent

teammates in the Photonics Research Group (PRG): Dr. Yashar Kiarashinejad, Omid Hemmatyar, Dr. Ali A. Eftekhar, Jiaqi Yuan, Tyler A. Brown, Zhongdi Peng, Daqian Bao, Dr. Hossein Taghinejad, Kirsten Masselink, Sai Rakesh Moha Vangapandu, Dr. Amir H. Hosseinnia, Dr. Ali E. Dorche, Hossein Maleki, Dr. Mohammad H. Javani, Mahmoodreza Marzban, Dr. Ashkan Zandi, Vishal B. Dhurgude, Abeer A. Alsaggaf, Dr. Spencer D. Fallek, Mohammadreza Tavakol Harandi, Abhirupa Saha, Mohammad H. Enjavi.

My deep gratitude also goes to Prof. Hayk Harutyunyan of Emory University Department of Physics for collaborating on all experimental characterizations in this thesis. I am extremely grateful to Dr. Chentao Li advised by Prof. Harutyunyan, for helping with most characterizations, which takes substantial amount of time. With deep knowledge in photonics, they also bring many insightful thoughts to my research, which improves the comprehensiveness of this work. I would also like to express my gratitude to their teammates Yuankai Tang and Dr. Guoce Yang for additional help and advice on characterizations.

Sample fabrication is a substantial part of my thesis. I have been fortunately supported by our dedicated staff engineers and scientists from the Institute for Electronic and Nanotechnology (IEN) and Materials Characterization Facilities (MCF) at Georgia Tech. I would like to thank Prof. Olive Brand, Dr. David Gottfried, Walter E. Henderson, and Gary Spinner for their leadership that IEN and MCF are world-renowned for facilitating top-level research. My special thanks go to Dr. Chris (Yeyuan) Yang, Todd J. Walters, Devin K. Brown, Andrew B. Watkins, Tran-Vinh D. Nguyen, and Yolande Berta for their direct support to my research projects. I also appreciate the staff Charlie A. Turgeon, Eric V. Woods, Dr. Hang Chen, Charlie Suh, Dr. Durga R. Gajula, Benjamin P.

Hollerbach, Alexander L. Gallmon, and Dr. Mikkel A. Thomas, for helping in different ways.

I would also like to thank great Georgia Tech ECE and Office of International Education (OIE) staff, especially Dr. Daniela Staiculescu and Libby Davis for continuous support to me as an international student through my Ph.D. studies.

My gratitude also goes to my friends met at Georgia Tech: Dr. Cheng Qi, Dr. Mohammad Taghinejad, Dr. Ruxiu Liu, Dr. Zhaocheng Liu, Dr. Yifei Fan, Dr. Zheng Wang, Dayu Zhu, Yuming Zou, Yiliang Guo, Dr. Kyutae Lee, Yuanzheng Zhu, Dr. Rui Zhang, Tianchong Jiang, Siyuan Liu, Xinyu Wei, Dr. Jiahao Yan, Dr. Sean P. Rodrigues, Andrew S. Kim, Dr. Anosh D. Daruwalla, Kaijie Huang, Genyi Luo, Dr. Jia Wei, Xiyu Ouyang, Haoting Li, Yang Jiang, Dr. Sicheng Wang, Jianning Cui, Dr. Congshan Wan, Dr. Hongmo Li, Shengtao Yu, Prof. Zhongkun Ouyang, Lakshmi R. Raju, Conghai Liu, Dr. Qian Yang, Prof. Bobin Deng, Dr. Qi Zhou, Zhenming Liu, Hua Chen, Chengming Yuan.

Last but not the least, I would like to express special thanks to my family and girlfriend. My parents and grandparents have always supported and encouraged me through ups and downs of the Ph.D. adventure. Their unconditional love fosters my confidence and courage to overcome challenges in life. I have been especially fortunate to meet my beloved girlfriend Yutong Sun at Georgia Tech, who is also a yellow jacket ECE Ph.D. student. She celebrates with me at every success, and always shares insights when there is a crucial decision to make. She has been the brightest star that lightened this adventure full of unknowns in the dark.

TABLE OF CONTENTS

ACKNOWLEDGEMENTS	iv
LIST OF TABLES	ix
LIST OF FIGURES	x
LIST OF SYMBOLS AND ABBREVIATIONS	xvii
SUMMARY	xxii
CHAPTER 1. Introduction and Background	1
1.1 Metamaterials and Metasurfaces	1
1.1.1 Resonances in MSs	2
1.1.2 Dielectric MSs	4
1.1.3 Tunable Linear MMs	5
1.2 Nonlinear MMs and MSs	7
1.2.1 Tunable NL MMs	8
1.2.2 Frequency Conversion MSs	9
1.2.3 Frequency Preserving NL MMs	12
1.3 Machine Learning in Metaphotonics	13
1.4 Thesis Outline	15
CHAPTER 2. Broadband-Tunable THG with an Asymmetric F-P GST Cavity	17
2.1 Introduction to Dynamically Controlled THG with Chalcogenide Nanodevices	17
2.2 Design and Fabrication of the F-P GST Cavity	19
2.3 Results and Discussion on the Device	23
2.4 The Characterization Setups and THG-Excitation Power Dependence	30
2.5 Conclusion and Outlook	33
CHAPTER 3. Dynamically Tunable Harmonic Generation Using Hybrid Plasmonic Metasurfaces with GST	34
3.1 Numerical Study of Wideband-Tunable THG Using Hybrid MSs with GST	34
3.1.1 Design and Simulations of the MIM MM	35
3.1.2 Results and Discussion	37
3.1.3 Conclusion and Outlook	39
3.2 Switchable SHG Using Hybrid Plasmonic MSs with GST	40
3.2.1 Introduction to Dynamically Controlled SHG and THG with Nanodevices	41
3.2.2 Design and Fabrication of the MIM MM	43
3.2.3 Results and Discussion on the Structure	47
3.2.4 The Characterization Setups and SHG-Excitation Power Dependence	54
3.2.5 Conclusion and Outlook	56

CHAPTER 4. Dynamically Tunable THG with a GST-Modulated a-Si MS	58
4.1 Introduction to All-Si THG MSs	58
4.2 Numerical Study of Tunable THG with a GST-Modulated a-Si MS	60
4.2.1 Design and Simulations of the GST-Modulated NL MS	60
4.2.2 Results and Discussion on the Numerical Design	65
4.3 Experimental Study of Tunable THG with a GST-Modulated a-Si MS	66
4.3.1 Fabrication and Characterizations of the Device	66
4.3.2 Results and Discussion	69
4.4 Conclusion and Outlook	70
 CHAPTER 5. Numerical Study of Reconfigurable Linear and NL Focusing Sb₂S₃ Metasurfaces	 72
5.1 Brief Introduction to NL All-Dielectric Metalenses	72
5.2 Design of the NL All-Sb₂S₃ Metalens	73
5.3 Simulation Results and Discussion	74
 CHAPTER 6. Quasi-BIC for Bidirectional Breaking-Symmetry NL Metasurfaces	 76
6.1 Introduction to BIC-based NL MSs	76
6.2 Theoretical Ultrahigh-Q a-Si MSs that Experimentally Reconfigure THG	79
6.2.1 Introduction to Optical Kerr Effect in NL MSs	79
6.2.2 Design and Fabrication of the a-Si MSs	80
6.2.3 Results and Discussion	84
6.2.4 The Characterization Setups	91
6.2.5 Conclusion and Outlook	92
 CHAPTER 7. DL-based Prediction of THG Resonance for Si Metasurfaces	 94
7.1 Brief Introduction	94
7.2 Simulations and the CNN	95
7.3 Results and Discussion	97
7.4 Conclusion and Outlook	99
 CHAPTER 8. Epilogue	 100
8.1 Brief Summary of Contributions	100
8.2 Future Directions	101
8.2.1 Optimization of Fabrication Processes	101
8.2.2 Expansion to More NL Processes	103
8.2.3 Imaging and Holography Applications	104
 REFERENCES	 106
 VITA	 124

LIST OF TABLES

Table 1	– Examples of tunable linear MMs based on VO ₂ , GST, and Sb ₂ S ₃ .	7
---------	---	---

LIST OF FIGURES

Figure 1	– Schematic of a THG MS made of a-Si. ω is the angular frequency of FH.	11
Figure 2	– (a) Schematic of the planar F-P-based NL device with operation under the normal-reflection mode. The thicknesses of the layers in this multilayer structure from bottom to top for all simulations in this subsection are 500 nm (Si), 100 nm (Au), 10, 20, or 50 nm (SiO ₂), 15-35 nm (GST), and 10, 50, or 100 nm (SiO ₂). The inset shows the schematic of GST in crystalline and amorphous states. T_g and T_m are the glass and melting temperatures of the PCM in schematic pictures throughout this thesis. (b) Real (n , solid curves) and imaginary (k , color-correspondent dashed) parts of refractive index of the 3 different crystallinity states of GST with different percent crystallization shown by L . The data for the amorphous and fully crystalline states is measured by ellipsometry of deposited GST samples. The property of the intermediate state is calculated using the Lorentz-Lorenz formula.	20
Figure 3	– Fabrication process for the as-grown asymmetric F-P cavity structure, in which e-beam evaporations and RF-sputtering were conducted.	22
Figure 4	– Simulated (a) reflectance spectra, and (b) THG spectral responses of the asymmetric F-P structure in Figure 2(a) for different GST crystallinities (L) with $t_{bo} = 25$ nm, $t_{GST} = 20$ nm, and $t_{to} = 50$ nm. Measured (c) reflectance spectra and (d) THG spectral responses of the corresponding fabricated sample with $t_{GST} = 25$ nm, considering the GST oxidation effect.	24
Figure 5	– Simulated (a) reflectance spectra, and b) THG spectral responses of the asymmetric F-P structure in Figure 2(a) with different L , $t_{bo} = 25$ nm, $t_{GST} = 10$ nm, and $t_{to} = 50$ nm. Measured (c) reflectance spectra, and (d) THG spectral responses of the corresponding fabricated samples with $t_{GST} \sim 15$ nm, considering the GST oxidation effect.	25
Figure 6	– Simulated (a) reflectance spectra, and (b) THG spectral responses of the structure in Figure 2(a) of different L , $t_{bo} = 25$ nm, $t_{GST} = 15$ nm, and $t_{to} = 50$ nm. Measured (c) reflectance spectra, and (d) THG spectral responses of the corresponding fabricated samples with $t_{GST} \sim 20$ nm, considering the GST oxidation effect.	26

Figure 7	– Plots of simulated resonant THG intensity and THG Q at different resonant fundamental wavelengths for the asymmetric F-P structure in Figure 2(a) with different values of L, with (a) $t_{\text{GST}} = 10$ nm (asterisk), $t_{\text{GST}} = 15$ nm (cross), $t_{\text{GST}} = 20$ nm (diamond), and with $t_{\text{bo}} = 25$ nm and $t_{\text{to}} = 50$ nm for all cases; (b) $t_{\text{bo}} = 10$ nm (asterisk) and $t_{\text{bo}} = 25$ nm (cross), $t_{\text{bo}} = 50$ nm (diamond), and with $t_{\text{GST}} = 20$ nm and $t_{\text{to}} = 50$ nm for all cases; and (c) $t_{\text{to}} = 10$ nm (asterisk), $t_{\text{to}} = 50$ nm (cross), $t_{\text{to}} = 100$ nm (diamond), and with $t_{\text{bo}} = 25$ nm and $t_{\text{GST}} = 20$ nm for all cases. The arbitrary units (a.u.) in (a), (b), and (c) represent the same normalization for the conversion efficiency.	29
Figure 8	– Plots of simulated linear nearfield normalized to the incidence (left) and THG nearfield in an a.u. (right) for the asymmetric F-P structure in Figure 2(a) for the (a) a-GST state and (b) c-GST state with $t_{\text{bo}} = 25$ nm, $t_{\text{GST}} = 20$ nm, and $t_{\text{to}} = 50$ nm. The extent of all materials is marked by solid lines. ω_a and ω_c are angular frequencies for the fundamental wavelengths of 1050 nm and 1500 nm at THG resonances for the a-GST and c-GST states, respectively.	30
Figure 9	– The setup schematic for the reflectance measurement of the GST F-P cavity devices, where ‘M’ and ‘10× MO’ represent a mirror and the 10× microscopic objective lens, respectively.	31
Figure 10	– The setup schematic for the THG measurement of the GST F-P cavity devices, where ND, LPF, and SPF represent neutral density, long-pass filter, and short-pass filter, respectively.	31
Figure 11	– Excitation power (i.e., pump power) dependence of the measured THG intensity from the a-GST sample of the structure in Figure 2(a) with deposited GST thickness ~ 20 nm at the excitation $\lambda_f = 1215$ nm. A power-law fit is applied to the measured data. The slope of the fit is 2.93 ± 0.15 at a confidence level of 95%, in agreement with the expected slope of 3 for THG. The excitation power was measured immediately after the ‘10× MO’ in Figure 10 without the sample. All fittings in this thesis are estimated at the 95% confidence.	32
Figure 12	– (a) Schematic of the Ag-GST-Ag device on a Si substrate. The square lattice period and the diameter of the nano-disk are 250 nm and 100 nm, respectively, for all simulations in this numerical study. (b) Real (n , solid curves) and imaginary (k , color-correspondent dashed) parts of refractive index of the 6 different crystallinity states of GST with different percent crystallization shown by L. The data for the extreme and intermediate states are the same and calculated in the same way as Figure 2(b).	36
Figure 13	– Simulated side-view normalized nearfields to incidence at resonances (top: linear; bottom: $\text{THG} \times 10^4$) for $T_{\text{Ag}} = 90$ nm and (a)	37

a-GST state and (b) c-GST state. Nearfields are calculated in the same ways for the a-GST state with (c) Ag plasmonic material with $T_{Ag} = 50$ nm and (d) Au plasmonic material with $T_{Au} = 50$ nm. λ_f values for different nearfield plots are (a) 1120 nm, (b) 1645 nm, (c) 1115 nm, and (d) 1115 nm. All material components of the nano-disks are marked in the plots. The nano-disks are placed on the same metal as the plasmonic nano-disk and surrounded by air for all plots.

- Figure 14 – Simulated (a) reflectance and (b) THG spectra of the structure in Figure 12(a) for the 6 different GST crystallinities (L). 38
- Figure 15 – (a) Schematic of the Au-GST-Au device composed of an array of Au (35-nm-thick) / GST (25-nm-thick) nano-disks on an Au reflector (100-nm-thick) and a Si substrate. The diameter of the nano-disk is selected as 120 nm, and the period of the MS is marked as p . (b) Schematic of the asymmetric F-P structure to be measured SHG and compared with the Au-GST-Au device. The Au reflector is also 100-nm thick, the bottom SiO₂ is 25-nm thick, the GST is 20-nm thick, and the top SiO₂ is 50-nm thick. (c) Fabrication process for the as-grown Au-GST-Au structure, in which e-beam evaporations of Au, spin coating of the e-beam resist, EBL, development of the resist, RF-sputtering of GST, lift-off, and ALD of an ultrathin SiO₂ protective layer were conducted. (d) A top-view SEM image of micron-scale area of an Au-GST-Au sample. (e) A top-view SEM image of submicron-scale area of another Au-GST-Au sample. All SEM images in this thesis are with a scaling measure marked. 45
- Figure 16 – (a) Simulated and (b) measured reflectance spectra for the structure in Figure 15(a) with cases of $p = 220$ nm, $p = 250$ nm, and $p = 280$ nm at the a-GST state. 47
- Figure 17 – (a) Simulated and (b) measured reflectance spectra for the structure in Figure 15(a) with $p = 220$ nm at investigated GST states. (c) Simulated reflectance spectra of the structure with parameters for Figure 17(a) at the visible wavelengths. (d) Measured SHG response of the correspondent fabricated samples, where λ_{SH} represents the SH wavelength, and the inset shows a zoomed-in view of the weak SHG signal for the a-GST case. 49
- Figure 18 – Measured (a) linear reflectance spectrum for the structure in Figure 15(b) at the c-GST state ($L = 100\%$); (b) c-GST state SHG spectra of the structure in Figure 15(a) with $p = 220$ nm, and the structure in Figure 15(b); (c) reflected NL emission intensity spectra, at the visible wavelengths, of the asymmetric F-P structure for the a-GST and c-GST states at a pump wavelength of 1150 nm. TPL: two-photon luminescence. 51

Figure 19	– Middle cross-sectional plots of simulated normalized nearfields in a plane parallel to the polarization direction (i.e., the incident polarization is in the plane of this figure) in (a) Figure 15(a) and (b) Figure 15(b) for the c-GST state at $\lambda = 1260$ nm. The fields are normalized to the incident field. Figure 19(a) and Figure 19(b) are in the same scale, and the maximum value of the scale bar is set to the maximum normalized nearfield in the Au-c-GST-Au structure at $\lambda = 1260$ nm. Figure 19(c) shows the normalized nearfield plot for the incidence wavelength of $\lambda/2$ (i.e., SH wavelength) under the same way of excitation. The mode overlap between nearfields in Figure 19(a) and Figure 19(c) is plotted in Figure 19(d) in terms of normalized inner-product of the nearfields to the square of incident field. Solid lines show the extent of all materials. All material components of the structures are marked in the plot except for the GST oxide, which is represented by unmarked areas (on top of the c-GST layer) in the plots.	53
Figure 20	– The setup schematic for the SHG measurement of the Au-GST-Au and F-P GST devices, where ND, ‘M’, ‘100× MO’, LPF, and SPF represent neutral density, a mirror, the 10× microscopic objective lens, a long-pass filter, and a short-pass filter, respectively.	55
Figure 21	– Excitation power (i.e., pump power) dependence of the measured SHG intensity from the sample of the structure in Figure 15(a) with $p = 220$ nm and the excitation $\lambda_f = 1080$ nm. A power-law fit is applied to the measured data. The slope of the fit (b) is 1.83 ± 0.24 , in acceptable agreement with the expected slope of 2 for SHG. The excitation power was measured immediately after the ‘100× MO’ in Figure 20 without the sample.	55
Figure 22	– Schematic of the reconfigurable NL MS; the device structure includes (on top of a Si handle layer) successive layers of 100-nm-thick Au, 10-nm-thick bottom buffer SiO ₂ , 50-nm-thick GST, 450-nm-thick top SiO ₂ , and a-Si with thickness $T_{a-Si} = 150$ nm. The dimensions of the a-Si MS are $p_1 = p_2 = 910$ nm, $a = 240$ nm, $b = 850$ nm, $g_1 = 75$ nm, and $g_2 = 85$ nm. T_g and T_m are the glass and melting temperatures of GST.	61
Figure 23	– (a) The linear transmission efficiency plot, and (b) simulated middle-z-plane nearfield plot at $\lambda_f = 1552.5$ nm of the a-Si MS on infinitely thick SiO ₂ at plane-wave normal incidence from air exhibiting EIT. The nearfields are normalized to the incident field (E_0), geometric dimensions of the MS are the same as those in the captions of Figure 22. (c) Simulated normalized middle-z-plane nearfield plots for the same MS on top of a 570-nm-thick SiO ₂ on the same Au reflector as in Figure 22 at $\lambda_f = 1550$ nm.	62

Figure 24	– Simulated normalized nearfield at the middle-z-plane of the MS for the structure in Figure 22 with (a) a-GST and (b) c-GST states. Simulated normalized nearfield plots of asymmetric (c) a-GST and (d) c-GST F-P cavity of $T_{\text{GST}} = 50$ nm sandwiched between two SiO_2 layers with thicknesses $T_{\text{to}} = 450$ nm and $T_{\text{bo}} = 10$ nm without the a-Si MS. Solid lines show the extent of all materials. The example planes of interference observations are marked with dashed lines. All plots are for plane-wave normal incidence at $\lambda_f = 1550$ nm. The large difference between the field enhancements in (a) and (b) is due to the constructive and destructive interference between the incident and reflected beams at ~ 200 nm above the top SiO_2 layer as seen in (c) and (d) for the a-GST and c-GST case, respectively.	64
Figure 25	– Simulated (a) linear reflectance spectra and (b) vertical-component THG efficiency plots for fundamental C-band for the 6 GST crystallinity percentages (L). THG efficiencies of this device are calculated in comparison to the simulation result in Ref. [101].	66
Figure 26	– Fabrication process for the as-grown structure in Figure 22, in which e-beam evaporations, PECVDs, RF-sputtering, ALD, spin coating of the e-beam resist, EBL and resist development, and ICP etching were conducted.	67
Figure 27	– A top-view SEM image of a few unit cells of an a-Si MS in a sample for the structure in Figure 22.	68
Figure 28	– Measured reflected NL emission intensity spectra, at the visible wavelengths, of the structure in Figure 22 for the a-GST, semi-c-GST, and c-GST states at a pump wavelength of 1600 nm.	69
Figure 29	– (a) Schematic of the designed linear and NL tunable-foci MS. (b) Real (solid curves) and imaginary (dashed curves) parts of the refractive indices of a-Sb ₂ S ₃ and c-Sb ₂ S ₃ extrapolated from data in Ref. [41].	73
Figure 30	– Simulated middle-incident-plane nearfields for the MS of (a) a-Sb ₂ S ₃ state @ $\lambda_f = 950$ nm and (b) a-Sb ₂ S ₃ state @ $\lambda_{\text{TH}} = 317$ nm, in relative field and a.u., respectively; (c) c-Sb ₂ S ₃ state @ $\lambda_f = 950$ nm and (d) c-Sb ₂ S ₃ state @ $\lambda_{\text{TH}} = 317$ nm, in relative field and a.u., respectively, with length scale in the orientation normal to the MS and dashed ellipses enclosing regions of focus marked.	75
Figure 31	– (a) Unit cell schematic of the normal-reflection-mode MS that comprises two identical nano-blocks with two mirror-symmetric corners cut in each nano-block on a SiO_2 substrate. Critical dimensions are marked as denotations. The square lattice period of unit cell p is 740 nm and the respective corners of adjacent parallel	82

nano-blocks are $p/2$ distant. The height of the nano-blocks is 300 nm, and the width of the nano-blocks W is in the range of 220 nm to 230 nm to fit the linear resonance to 1200–1400 nm. The length of the nano-blocks is $2W$. The perimeter of all cut corners is 360 nm and those from the left nano-block are squares. The width d of cut-corners in the right nano-block is 80 nm, 70 nm, or 60 nm, which makes the parallel cut-corner nano-blocks very similar in planar size with a minimum area difference of 200 nm². (b) A control structure unit cell also evolved from the identical nano-blocks of $W = 220$ nm as in (a), but the width of its right nano-block is 210 nm, resulting in a planar area difference between the symmetry-breaking nano-blocks of 4400 nm². The square lattice period of unit cell p is 740 nm and the respective corners of the parallel nano-blocks are $p/2$ distant, same as in (a).

- | | | |
|-----------|--|----|
| Figure 32 | – Fabrication process for the a-Si MS samples with left-over HSQ, in which low-temperature PECVD of a-Si, EBL of spin coated HSQ, and ICP etching with Cl ₂ were conducted. | 84 |
| Figure 33 | – Top-view SEM images of a unit cell of the fabricated structure in Figure 31(a) with $W = 220$ nm (left, Sample 1) and $W = 230$ nm (right, Sample 2), with the scaling measure marked. The left/right image shows the square-corner-cut nano-block on the right/left. | 84 |
| Figure 34 | – Simulated plots of the normalized nearfields at middle-plane interceptions to all axes based on each pre-symmetry-breaking nano-block, due to incidence at the quasi-BIC resonances (a) ~ 1217.24 nm for the structure in Figure 31(a) with $W = 220$ nm and $d = 80$ nm; (b) ~ 1248.8 nm for the structure in Figure 31(b). Simulated reflectance spectra (c) and (d) marked with Q factors in the vicinity of (a) and (b). The reflectance Qs are defined as the ratio of the dip frequency to the FWHM of the dip in the reflectance spectrum. The half-maximum level of a reflectance dip is approximated by averaging the dip reflectance and the highest reflectance in the vicinity of the dip. | 86 |
| Figure 35 | – Simulated cross-planar plots of the normalized nearfields for incidence at the quasi-BIC resonances (a) ~ 1217.24 nm (simplified from Figure 34(a) of $W/d = 220$ nm / 80 nm), (b) ~ 1217.9 nm for the structure in Figure 31(a) with $W/d = 220$ nm / 70 nm, and (c) ~ 1219.4 nm for the structure in Figure 31(a) with $W/d = 220$ nm / 60 nm. | 87 |
| Figure 36 | – Simulated reflectance spectra in the range of the quasi-BIC resonance and inset middle intercept planar plots of the normalized nearfields for incidence at the resonances (a) ~ 1217.24 nm for the base structure of $W/d = 220$ nm / 80 nm, (b) ~ 1230.16 nm for the structure in Figure 31(a) with $W/d = 225$ nm / 80 nm, (c) ~ 1242.24 | 88 |

nm for the structure in Figure 31(a) with $W/d = 230 \text{ nm} / 80 \text{ nm}$. The reflectance Qs are marked in the plots and planar contours of the cut-corner nano-blocks are marked by solid lines. The reflectance Qs are defined as the ratio of the dip frequency to the FWHM of the dip in the reflectance spectrum. The half-maximum level of a reflectance dip is approximated by averaging the dip reflectance and the highest reflectance in the vicinity of the dip.

- | | | |
|-----------|--|----|
| Figure 37 | – Measured right-y-axis-calibrated linear reflectance spectrum (dashed) joint with THG efficiency spectra at peak pump intensities (I _{PPS}) of $\sim 1.33 \text{ GW/cm}^2$ and $\sim 3.34 \text{ GW/cm}^2$, for (a) Sample 1 and (b) Sample 2. | 90 |
| Figure 38 | – The setup schematic for the linear reflectance measurement of the a-Si BIC MS samples, where ‘M’ and ‘10× MO’ represent a mirror and the 10× microscopic objective lens, respectively. | 91 |
| Figure 39 | – The setup schematic for the THG measurement of the a-Si BIC MS samples, where ND, LPF, and SPF represent neutral density, long-pass filter, and short-pass filter, respectively. | 92 |
| Figure 40 | – (a) Example schematic of the unit cell of a square-lattice MS with a single random binary-pixelated contractible Si nano-resonator on a SiO ₂ substrate, which works at plane-wave normal incidence from air and a transmission mode. (b) An illustration of the CNN structure for predicting the THG response of the MS with a unit cell as that in (a). The CNN is composed of 3 blocks of convolutional layers (each one includes 2 convolutional layers with ReLU activation function and a maximum pooling layer); a fully connected layer with 512 nodes; and fully connected layers with 256 nodes, 128 nodes, and 3 nodes (2 layers for each number of nodes in a layer). | 96 |
| Figure 41 | – Model prediction accuracies and confusion matrices for (a) the THG resonance wavelength and (b) the resonant THG output intensity data of the binary-pixelated MSs. | 98 |

LIST OF SYMBOLS AND ABBREVIATIONS

Ag	silver
AI	artificial intelligence
ALD	atomic layer deposition
Au	gold
a.u.	arbitrary unit
a-GST	amorphous germanium antimony telluride
a-Sb ₂ S ₃	amorphous antimony sulfide
a-Si	amorphous silicon
BIC	bound states in the continuum
Cl ₂	chlorine
CNN	convolutional neural network
C-band	conventional band
c-GST	crystalline germanium antimony telluride
c-Sb ₂ S ₃	crystalline antimony sulfide
c-Si	crystalline silicon
DFG	difference-frequency generation
DL	deep learning
EBL	electron-beam lithography
EFISH	electric field induced second-harmonic generation
EIT	electromagnetically-induced transparency
ENZ	epsilon-near-zero
E _g	bandgap

E_0	incident electric field
e-beam	electron-beam
FEM	finite element method
FH	fundamental harmonic
FWHM	full-width- at-half-maximum
FWM	four-wave mixing
F-P	Fabry-Perot
GaAs	gallium arsenide
GSST	$\text{Ge}_2\text{Sb}_2\text{Se}_4\text{Te}_1$
GST	germanium antimony telluride
HHG	high-harmonic generation
HSQ	hydrogen silsesquioxane
high-Q	high-quality-factor
ICP	inductively coupled plasma
ITO	indium-tin oxide
I	optical intensity
I_{PP}	peak pump intensity
I_{PPH}	higher peak pump intensity
I_{PPL}	lower peak pump intensity
k	refractive index (imaginary part)
L	crystallinity percentage
LPF	long-pass filter
M	mirror
M	maximum nearfield enhancement
MEMS	micro-electromechanical system

MIM	metal-insulator-metal
MIR	mid-infrared
ML	machine learning
MM	metamaterial
MO	microscopic objective
MS	metasurface
M_d	modulation depth
NA	numerical aperture
ND	neutral density
NIR	near-infrared
NL	nonlinear
NP	nanoparticle
n	refractive index (real part)
n_0	refractive index at zero optical intensity
n_2	second-order nonlinear refractive index
OPO	optical parametric oscillator
PCM	phase-change material
PECVD	plasma-enhanced chemical vapor deposition
PMMA	poly (methyl methacrylate)
\mathbf{P}	electric polarization
p	unit cell period
poly-Si	polycrystalline silicon
Q	quality factor
ReLU	rectified linear unit
RF	radio-frequency

SEM	scanning electron microscopy
SFG	sum-frequency generation
SH	second-harmonic
SHG	second-harmonic generation
SPF	short-pass filter
SPR	surface plasmon resonance
Sb ₂ S ₃	antimony sulfide
Si	silicon
Si ₃ N ₄	silicon nitride
SiO ₂	silicon dioxide
TH	third harmonic
THG	third-harmonic generation
TMAH	tetramethylammonium hydroxide
TPA	two-photon absorption
TPL	two-photon luminescence
TiO ₂	titanium dioxide
T _g	glass transition temperature
T _m	melting point
t _{Au}	gold reflector thickness
t _{bo}	bottom SiO ₂ layer thickness
t _{GST}	GST layer thickness
T _{a-Si}	amorphous silicon layer thickness
T _M	metallic nano-disk thickness
t _{to}	top SiO ₂ layer thickness
VO ₂	vanadium dioxide

W	tungsten
1D	one-dimensional
2D	two-dimensional
3D	three-dimensional
$\chi^{(n)}$	nth-order optical susceptibility
λ	wavelength
λ_f	fundamental wavelength
λ_{SH}	second-harmonic wavelength
λ_{TH}	third-harmonic wavelength
ω	angular frequency
ϵ_0	vacuum permittivity
\propto	proportional to
α	asymmetric factor
ΔA	meta-atom area difference
ΔL	half of meta-atom width difference

SUMMARY

Optical frequency conversion processes, such as second- and third-harmonic generation, are commonly realized in nonlinear (NL) optics, offering application opportunities in photonics, chemistry, material science, and biosensing. Limited by the intrinsic weak NL response of natural materials, optically large samples and complex phase-matching techniques are typically required to realize significant NL conversions. In order to realize efficient frequency conversions in much smaller volumes, current research has been devoted to the quest of synthesizing novel materials with enhanced optical nonlinearities at moderate input intensities. Frequency preserving NL processes, such as the optical Kerr effect and saturable absorption, are more suited for computing applications, due to efficient optical-intensity-dependent operation. In particular, several approaches for engineering the NL properties of artificial materials, metamaterials (MMs), and metasurfaces (MSs) of ordered building block arrays have been introduced to manipulate light at the subwavelength scale. High-refractive-index phase-change materials (PCMs), such as germanium antimony telluride (GST) and antimony sulfide (Sb_2S_3), that inherently exhibit strongly active tunable large optical nonlinearities have the potential to further enhance the tunability of NL MMs and MSs. Passive silicon-based MMs and MSs have various mode engineering opportunities (thanks to the high refractive index of silicon and the ease of fabrication of a variety of nanostructures in it) to realize enhanced optical nonlinearity as well.

This thesis is focused on both numerical designs and experimental demonstrations of PCM- and silicon-based reconfigurable NL MMs and MSs. I demonstrated a broadband-

tunable subwavelength third-harmonic generation (THG) device with an asymmetric Fabry-Perot (F-P) cavity numerically and experimentally, based on both extreme and intermediate crystallinity states of GST. I also extended the numerical study of the THG band tunability of GST to a gap-surface-plasmon hybridized structure with enhanced THG efficiency, and experimentally demonstrated the same structure for intensity tunability of efficient second-harmonic generation (SHG). To mitigate the optical loss of GST, I designed a passive high-quality-factor (high-Q) silicon MS of optical responses modulated by an active subwavelength GST F-P cavity. Large resonant field enhancement can be exhibited in the nano-resonators. Using the resulting elevated conversion efficiency, I have numerically and experimentally demonstrated a THG intensity switch with a large extinction ratio. These tunable NL demonstrations have great potential for applications such as NL optical microscopy and communications due to the strong tunability of GST. The last result in the PCM-based research part is a numerical demonstration of an all-Sb₂S₃ linear and THG MS. The designed MS interchanges foci of the MS at amorphous and crystalline Sb₂S₃ states for the fundamental frequency and the third harmonic frequency, respectively. This structure is of interest for NL imaging and microscopy applications.

The silicon-based research part is focused on the use of higher-Q bounded states in the continuum (BIC) resonance phenomena and the implementation of a deep learning technique for all-silicon MSs. The objectives are physical-driven high nonlinearity and algorithm prediction of NL conversion characteristics of the MSs, respectively. A type of novel bidirectional breaking-symmetry MSs is numerically designed to feature a quasi-BIC resonance for ultra-large field enhancement in the meta-atoms, expecting efficient THG. Experimental optical Kerr effect is observed in efficient THG from the MSs, which paves

the way for variational quasi-BIC designs for switchable NL generation applications. In the other work, to demonstrate a prediction method for resonant THG characteristics of free-form patterned dielectric MSs without time-consuming numerical simulations, classifications of the spectral location and the intensity level of the simulated THG resonance of binary-pixel-patterned silicon MSs using a convolutional neural network are conducted.

CHAPTER 1. INTRODUCTION AND BACKGROUND

This chapter summarizes background research findings and engineering practices that are the building blocks for this thesis as well as an outline of the thesis. The first part is a general review of the photonic metamaterials (MMs) and metasurfaces (MSs). Besides its subwavelength resonant features, the focus is on lossless functional dielectric MSs and dynamic tunability introduced to the MMs in comparison with conventional photonic materials. The second part is a review of the previous works on nonlinear (NL) MMs and MSs. Different types of NL MM and MS device configurations, especially for tunable NL MMs and efficient NL dielectric MSs, will be discussed. The NL dielectric MSs will be reviewed by dividing to categories of frequency conversion (second- / third-harmonic generations, *etc.*) and frequency preserving (all-optical modulation, *etc.*). The last part presents the thesis outline.

1.1 Metamaterials and Metasurfaces

Photonic MMs are three-dimensional (3D) artificial assemblies of subwavelength plasmonic/dielectric building blocks, in another word ‘meta-atoms’, to control light-matter interaction in ways that differs from natural materials [1, 2]. Fine designs of the material and geometry of the meta-atoms can tailor linear optical properties such as the effective permittivity and permeability of the MMs, which break the limits of meta-atom materials’ chemical compositions imposed on the electromagnetic responses of the meta-atoms [3]. Novel optical phenomena such as negative refraction, superlensing, and cloaking have been demonstrated in various MM designs [3]. However, the 3D MMs face challenges of nanofabrication and large optical losses due to multi-layer operations, which affects their

practical applications in the optical regime [3]. MSs, the two-dimensional (2D) counterpart of MMs as structured interfaces with meta-atoms forming spatially varying patterns [3], have attracted tremendous attention from the optics community as highly functional, broadband, and spatial tailoring large-area platforms for flat-optics components [4] and chip-scale nanophotonic devices [5] due to their improved compactness and nanofabrication feasibility with reduced loss compared to 3D MMs. However, MSs of a single layer or only a few layers are restricted by limited functionality of each layer. Despite the limitations of 3D MMs and 2D MSs, these meta-structures have been demonstrated great potentials in emerging applications of cloaking [6], sensing [7, 8], vortex beam generation [9], holography and data storage [10, 11], high numerical aperture (NA) imaging [12, 13], encryption [14], NL optics [3, 15, 16], *etc.*

1.1.1 Resonances in MSs

Resonances play a crucial role in the light interaction with MSs for tailoring linear transmission or reflection amplitude and phase, and NL responses as the resonances allow substantial enhancement of both the electric and magnetic fields [4]. The effects are equivalent to off-resonance excitation of the MSs with a substantially more intense light beam. These resonances include both local and collective resonances. Local resonances are generally exhibited in individual nanoparticles (NPs) such as surface plasmon resonances (SPRs) of metallic (plasmonic) NPs and Mie resonances of dielectric NPs [4]. In comparison, collective resonances such as Fano-type resonances, guided-mode resonances, and bound states in the continuum (BICs) [4] are commonly designed with dense periodic NP arrays.

SPR is the resonant oscillation of conduction electrons at the surface of a plasmonic NP separating negative (metal) and positive (surrounding media) permittivity materials excited by the incident light, which are associated with strong localization of energy in subwavelength regions, but with strong absorption by the plasmonic NPs, typically gold (Au) or silver (Ag) [4]. Mie resonances are conventionally associated with the analytical Mie solutions of Maxwell's equations for spherical particles. This type of resonances is emergingly employed for the light manipulation below the free-space diffraction limit [17] by high-index dielectric NPs supporting electric and magnetic type dipolar (or multipolar) [17, 18] resonances of comparable strengths [4].

Fano resonances are supported by appropriate combinations of NPs generating collective interference between different localized modes and radiative electromagnetic waves [19], and manifesting resonant suppression of the total scattering cross section accompanied by enhanced absorption in the MSs [4]. Fano resonances are promising for nanoscale bio-sensing, switching, and lasing applications due to more efficient light confinement [4] and narrower resonance line-shapes or higher spectral quality factors (Qs). Guided-mode resonances occur when the input light couples to leaky waveguide modes of the MSs [4]. BICs are non-radiating states, characterized by the resonant frequencies embedded to the continuum spectrum of radiating modes of the surrounding space for the designed MSs [20], that aim at infinite radiative Q [21]. Fano- and BIC- type resonances will be applied in this thesis due to their strong light-matter interactions, which are promising for NL optical applications.

1.1.2 Dielectric MSs

Dielectric MSs are attracting increased attention due to their much smaller losses and generally higher light irradiation damage thresholds than the plasmonic counterpart, at the visible and near-infrared (NIR) wavelengths. The relatively low damage thresholds of plasmonic MSs are induced by the intrinsic losses of metal due to heating of the nanostructures [4]. Multiple types of high-Q ($Q > 100$) resonances are supported in dielectric MSs, such as Mie [22], Fano [23], guided-mode [24], and BIC resonances [25, 26], due to the low-loss characteristics of dielectric materials. Dielectric MSs with materials of higher refractive indices are more favorable due to higher optical field confinement in the MS at a lossless condition. A wide range of dielectric materials has been investigated and implemented in MSs. Silicon (Si) is one of the most used materials due to its large refractive index and maturity of nanofabrication, and it has been implemented in MS designs for applications of sensing [8], vortex generation [9], holographic encryption [14], NL optics [16, 27, 28] with Mie and Fano-type resonances, whereas ultra-high-Q ($Q > 1000$) guided-mode [24] and BIC-type [26] resonances haven't yet been discussed about applications due to the requirement of precise operations of highly-collimated optical beam incidence. The operating wavelength range strongly depends on the crystallinity of Si [29]: amorphous and polycrystalline Si devices can efficiently operate in the infrared and near-infrared wavelength ranges [30], while single-crystal Si devices can efficiently function at visible wavelengths due to its relatively low absorption losses [31]. III-V semiconductors with refractive indices comparable to that of Si, such as gallium arsenide (GaAs) and its alloy with indium, i.e., $\text{In}_x\text{Ga}_{1-x}\text{As}$, can also serve in high-efficiency NIR MSs [30, 32, 33], especially for quantum applications [34,

35], although with the drawback of high cost. For devices operating in the visible spectrum and parts of the ultraviolet spectrum, titanium dioxide (TiO_2) [12] and gallium nitride [36] are suitable due to their transparency at those wavelengths, but they have smaller refractive indices than Si [30]. There have also been demonstrations of MSs materials with even lower refractive indices, such as silicon nitride (Si_3N_4) [37] and hafnium oxide [38].

1.1.3 Tunable Linear MMs

Although MMs and MSs have been able to manipulate light at the subwavelength scale, most of the meta-structures are statically designed by the fixed structures and the immutability of the materials used in their construction [39]. Tunability and reconfigurability are significant factors for functional devices using active MMs [40]. Phase-change materials (PCMs) which exhibit reconfigurable changes of refractive indices among different crystallinity states with external stimuli, such as conventional annealing [41], Joule heating [42, 43], and focused-beam irradiation [44], are capturing worldwide linear nanophotonic research efforts due to the fast, repeatable and nonvolatile responses to stimuli [5], and compatibility to chip-based microsystems. Chemical and electrochemical tuning [45], volume-changing materials [46], and external environment reconfiguration (flexible and stretchable substrate [47], shape memory effect [48], and micro-electromechanical system (MEMS) integration [49]) are also widely explored in tunable linear MMs [39]. However, it is either challenging to adopt these tunabilities on chip-based microsystems or limited in performance to implement them compared to PCMs.

Vanadium dioxide (VO_2) is one of the representative PCMs that exhibit an insulator-to-conductor transition at the characteristic temperature of $\sim 69^\circ\text{C}$ [39].

However, only $\sim 10\%$ of spectral tuning scope has been demonstrated in VO₂ MMs at the NIR and visible [5, 39], since VO₂ exhibits limited changes in the optical properties at these spectral ranges compared to more pronounced contrasts at the mid-infrared (MIR) [39, 50]. Phase-change chalcogenides are a class of amorphous semiconductors widely used in phase-change memories [51], which have representatives of germanium antimony telluride Ge₂Sb₂Te₅ (in short, GST) and antimony sulfide (Sb₂S₃) that exhibit large differences of refractive indices between the amorphous states and crystalline states (up to $\sim 50\%$ compared to the low-index amorphous states) at the NIR and visible, respectively [41, 52]. Optical bandgaps of both materials experience are decreased during crystallization. Therefore, their crystalline states are lossier than the amorphous states. GST, which exhibits a glass transition temperature (T_g) of $\sim 130^\circ\text{C}$ [53] and a relatively low melting point (T_m) of $\sim 600^\circ\text{C}$ [42], is promising for ultra-compact nanoscale modulator components of on-chip NIR communication systems. This is due to GST's phase change characteristics of large contrast in the optical and electronic properties, the subwavelength scalability (down to nanometers), reasonably fast switching speed (10's-100's nanoseconds) [52], high switching robustness (potentially up to 10^{15} cycles) [54], nonvolatility (and thus, power efficiency), high thermal stability, and adaptability with the CMOS fabrication technology [55]. Sb₂S₃ has a larger bandgap (E_g) and concomitantly lower absorption loss than GST, however, exhibits both smaller refractive indices change in both real and imaginary parts for most of visible and NIR spectra, and a higher T_g of $\sim 250^\circ\text{C}$, however slightly lower T_m of $\sim 550^\circ\text{C}$ [41]. Nanoscale reprogrammable Sb₂S₃ devices have been demonstrated similarly short phase switching times as nanoscale GST devices [41, 56], and with similar nonvolatility and thermal characteristic as GST, which

are in common for chalcogenide glasses. Thus, Sb_2S_3 has potential for reconfigurable flat optics and micro-optical modulation systems operating at the visible spectrum.

Table 1 compares some reported tunable linear optical MMs based on VO_2 , GST, and Sb_2S_3 . The values of modulation depth/rate are for spectral differences except for two demonstrations of phase shift (in degrees) and geometric broadening (in millimeters), respectively. It is clear that GST-based devices generally exhibit larger spectral modulation depths than Sb_2S_3 at the desired spectral range due to slightly larger tunability of GST and the infancy of research on Sb_2S_3 photonics. Oxidation issues of both GST [42] and Sb_2S_3 [57] can be partially resolved by the deposition of oxide capping layers [42].

Table 1 – Examples of tunable linear MMs based on VO_2 , GST, and Sb_2S_3 .

Active material	External stimuli	Modulation depth/rate	Advantages	Limitations	Refs
VO_2	Thermal annealing	$\sim 80\%$	Low power consumption	MIR operation	[50]
	Electrical heating	$\sim 10^\circ/\text{ms}$			[58]
	Focused beam	$0.03\text{--}2\text{ mm/s}$			[44]
GST	Thermal annealing	$\sim 50\%$	Nonvolatile, thermally stable	Oxidation, absorption loss	[59]
	Electrical heating	$\sim (0.2\text{--}40)\text{ }^\circ/\mu\text{s}$			[60]
	Focused beam	$\sim 70\%$			[61]
Sb_2S_3	Thermal annealing	$\sim 30\%$	Visible spectrum operation	Oxidation at phase conversions	[62]
	Electrical heating	$\sim 10\%/\mu\text{s}$			[41]
	Focused beam	$\sim 0.25\%/\text{ns}$			

1.2 Nonlinear MMs and MSs

Frequency conversion processes (such as second- and third-harmonic generation [63, 64]) and frequency preserving NL phenomena (such as optical Kerr effect [65] and two-photon absorption (TPA) [66]) are commonly realized in NL optics, offering

opportunities for applications in optical signal processing and computing [67, 68], ultra-short pulsed lasing and amplification [69, 70], ultrafast switching [71], sensing [72, 73], high-resolution imaging and microscopy [74, 75], *etc.* Given the inherently weak NL response of natural materials, optically large samples and complex phase-matching techniques for frequency conversion are typically required to realize significant NL responses [76]. To produce similar effects on chip-scale devices, a large portion of research has been devoted to the quest of engineering NL properties of ordered MMs and MSs with stability for enhanced optical nonlinearity at moderate input intensities [76].

1.2.1 Tunable NL MMs

Most reported tunable NL MMs have featured 1) external stimuli to tune the NL responses of nanostructures in real-time [77, 78], or 2) passive components for offline manipulation of the optical nonlinearity [79, 80] with conventional plasmonic or dielectric materials. Traditional stimulating methods, such as global heating and mechanical deformation [81, 82], can rarely meet the demands of high-speed NL modulators/switches for on-chip photonic systems. Stimuli of electric signals are widely used due to their fast operations and high controllability. The electric signals generally bring substantial electric field induced second-harmonic generation (EFISH) to centrosymmetric media [77, 83], or drive carrier movements (such as in indium-tin oxide (ITO) [84] and graphene [85]) to realize tunable operations of NL MMs without the need of voltages more than 10's of volts. All-optical modulations [27, 80, 86] can be deemed a combination of optical stimuli (pump lights with possible excitation of carrier transports) and passive components (typically Kerr NL materials that exhibit traceable NL dispersion at enhanced local optical intensity), which is a trending research topic in MMs for all-optical computing that circumvents less-

efficient electric control signals. However, current demonstrations of all-optical modulations by MMs are mostly limited to transient responses at pulsed laser operations. Ultrahigh-Q Si MSs will be applied in the Si-based research part for Kerr-effect operation to circumvent transient operations.

Since these demonstrations are limited by inherently weak NL optical tunability of the material compositions, there are investigations resorting to high-index PCM GST [87] and $\text{Ge}_2\text{Sb}_2\text{Se}_4\text{Te}_1$ (GSST) [88], an engineered low-loss alloy of GST [89]. These materials exhibit large third-order optical nonlinearity at amorphous states and many-fold increase of the nonlinearity after crystallization, according to empirical Miller's rule [90]. Especially, Cao *et al.* experimentally demonstrated a giant third-harmonic generation (THG) intensity modulation of ~ 400 -fold by GST at a decent THG efficiency of $\sim 10^{-10}$ with a subwavelength cavity device pumped at the NIR [87]. This is an unprecedented NL intensity modulation depth to the best of my knowledge. Since more practical NL optical designs, such as band-tunable frequency conversion and dynamic second-harmonic generation (SHG) switching of high extinction ratios (potential platforms for NL optical microscopy and communication), reconfigurable NL focusing (potential platforms for NL imaging and microscopy), have not been demonstrated with MMs based on high-index PCMs, GST and Sb_2S_3 will be applied in the PCM-based research part for these novel demonstrations.

1.2.2 Frequency Conversion MSs

Although the short NL interaction length in MSs hampers frequency conversion efficiency, these MSs have several other merits over bulk materials than large nearfield

enhancements to make compensations: 1) Phase-matching issue, which originates from material dispersion, is resolved in subwavelength structures; 2) Symmetric-breaking design opportunities to imbalance interference between excited counter-propagating waves, which circumvents macroscopic suppression by symmetries of the materials and fields, for Fano-shape high-Q resonances [4, 91]; 3) Possible dispersion engineering at the harmonic, since subwavelength resonances are sensitive to the composite refractive indices [4].

SHG is a stronger NL process compared to higher-harmonic generations, however, can be only obtained with non-centrosymmetric materials or interfaces [92]. SHG has been initially investigated at the surfaces of noble metal nanostructures in the development of plasmonic MSs [4, 93]. These plasmonic implementations of SHG MSs suffer from intrinsic losses of metals and their relatively low damage thresholds, which in particular limits the applicability of NL applications due to the power-dependent efficiencies [4]. It has been shown that by switching to dielectric MSs, NL efficiencies could be considerably enhanced with MSs made of 1) second-order NL crystals (such as zinc oxide [94] and GaAs [95]) and ferroelectrics (such as lithium niobate [96]) with intrinsic nonlinearity, or 2) breaking-symmetry resonators of high-index non-centrosymmetric materials (such as Si [97]) with surface nonlinearity [4]. In these MSs, SHG efficiency has been increased as compared to homogeneous films by a factor of up to 10^4 [4] and reached up to $\sim 10^{-4}$ [98].

Unlike second-order NL effects, third-order effects do not require non-centrosymmetric structures. Therefore, the widely available high-index material Si has become the material of choice for the realization of efficient THG in MSs [4] for NIR fundamental harmonic (FH). Figure 1 is an example schematic of a THG MS made of amorphous Si (a-

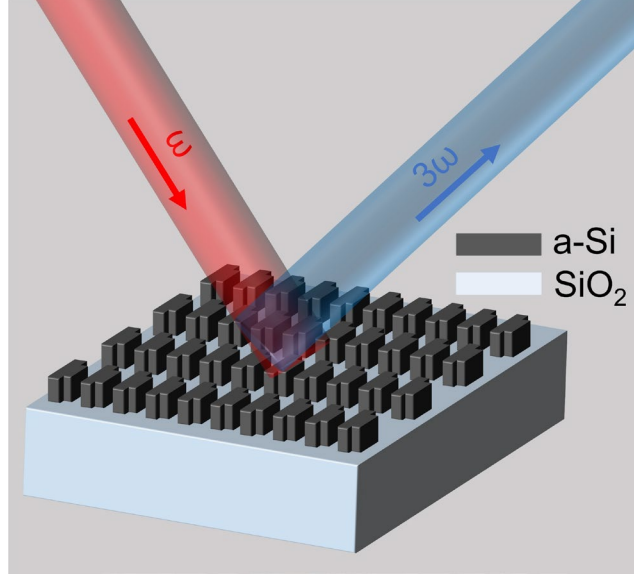


Figure 1 – Schematic of a THG MS made of a-Si. ω is the angular frequency of FH.

Si), where ω is the angular frequency of FH. Due to the large frequency shift from FH to the third harmonic (TH), dispersion in resonant MSs becomes more important for THG than for SHG [4]. It has been discovered that magnetic dipole modes, which exhibit better field overlap with the NL harmonic and higher Q factors [99], should be preferred over electric dipole modes [4]. Further improvement of THG efficiency was achieved by increasing the field trapping based on hybridization of Si nano-resonators with plasmonic Au structures [4, 100]. Based on the maturity and high precision of Si nanofabrication, complicated MS geometries fabricated for collective resonance effects have demonstrated up to 1.5×10^5 -fold THG output intensity enhancement compared to an unpatterned Si film and THG efficiencies up to 1.2×10^{-6} [101]. High-harmonic generation (HHG) and frequency mixing are high-order NL processes applicable to attosecond photonics [102] and supercontinuum generation [103], respectively, requiring ultrahigh pump intensity and thus all-dielectric MSs [4]. High-order odd harmonic generation, not requiring non-centrosymmetric structures [102, 104], is studied more frequently than high-order even

harmonic generation [104]. High-Q all-Si MSs will be designed with giant THG tunability by PCMs in the PCM-based research part, and for the purpose of more efficient THG in the Si-based research.

1.2.3 Frequency Preserving NL MMs

Frequency preserving NL processes are generally more detectable than frequency conversions in MSs. Optical Kerr effect gives rise to an increase of the refractive index with intensity [105] with $n = n_0 + n_2 I$, where n_0 is the refractive index at zero optical intensity, n_2 is the second-order NL index of refraction, I is the optical intensity. It had been conventionally applied to flat self-focusing lenses [106] for high-power Gaussian profile laser beams, creating elongated optical path in the center of the lens, which is analogous to a convex lens. Recently, the Kerr effect has been leveraged in all-optical modulations in MMs [80, 107] and MSs [108, 109] of both plasmonic [110, 111] and dielectric components [109, 112]. There are reported normalized modulation depths (M_d s) of $\sim 40\%$ by gallium phosphide nano-disks [109] and $\sim 20\%$ with epsilon-near-zero (ENZ) ITO hybridized by plasmonic Au [80]. Tremendously enhanced local optical intensity at resonance, especially for ENZ materials that can capacitate infinite electric field in theory [113], enables strengthened Kerr effect compared to conventional material platforms. The optical responses, in turn, gains sensitivity to the Kerr effect due to generally associated high-Q characteristics of the strong resonance.

In addition to all-optical modulations with Kerr effect, there are studies on frequency preserving NL MMs by employing TPA of Si [4, 27] and strong absorption saturation in plasmonic Au ($M_d = 60\%$) [114] and GaAs (M_d of $\sim 15\%$) [115] at the NIR.

However, these finds are generally limited by transient operations of high peak pump intensity at the scale of GW/cm^2 [27, 115], comparable to those for frequency conversion [95, 101, 116].

1.3 Machine Learning in Metaphotonics

Artificial intelligence (AI) has thrived in research areas of computer vision, natural language processing, cyber security, speech and character recognition for decades. In the recent era, AI has also been witnessed to aid designs of microelectronic [117-119] and integrated photonic systems [120, 121]. Besides these system-level implementations, AI techniques have been found accelerating research at the MM and MS devices level, i.e., metaphotonics [122, 123], as well. Machine learning (ML), as a study of algorithms that automate prediction and decision-making based on high-dimensional data, is one of the most effective techniques in the field of AI study [123]. Thanks to recent advances in technologies of fabricating metaphotonic devices, extensive design flexibility exists through selection of constituent materials and geometrical properties of individual meta-atoms [124]. Therefore, ML is emergingly demanded in metaphotonics research to analyze and predict responses under high-dimensional design parameters, where filtering these parameters by numerical simulations can be time-consuming. Since the underlying physics of the electromagnetic nanostructures remains largely elusive, knowledge discovery on photonic interactions with MMs and MSs has been expedited by studies of dimensionality reduction enabled by ML techniques [125, 126].

Inverse design is a more popular topic in leveraging ML techniques in metaphotonics. The purpose of the design is to obtain material or geometric design

parameters of a predefined photonic structure given a desired spectral response, in contrary to the normal forward design of simulating the spectral response under given design parameters. The metaphotonic inverse design is a prediction problem in ML and is usually challenging, due to a large number of parameters in both design and response spaces. ML architectures based on neural networks, which are inspired by the learning patterns in biological nervous systems, [123] and deeper layers of linear and NL learning functions, i.e. deep learning (DL) networks, are essential for this type of problems of prediction. These networks can be conceptually divided to discriminative and generative models. Discriminative models can approximate forward simulations more accurately, whereas generative models can reduce the dimensionality of extraordinarily high-dimensional design space when it is infeasible to generate sufficient data in the original design space for training a discriminative model [123]. Bidirectional neural networks [127, 128] and convolutional neural networks (CNNs) [129, 130] have been reported in metaphotonic inverse designs with deep discriminative models. Generative adversarial networks [131, 132], autoencoders [124, 126], and variational autoencoders [133, 134] have been reported for designs with deep generative models.

Simulations of metaphotonic frequency conversion, which comprise two frequency domains and additional physical assumptions, are susceptible to relatively larger numerical errors and are even more time-consuming than linear simulations. Hence, it is worth studying forward prediction of the NL responses based on DL. Designed for data with spatial structure, CNNs have conventional employment in digital image classifications [135]. Labeling the rough NL responses of training data with discrete classes can be an effective way to estimate the responses for complex geometric patterns of the structure

with a CNN. An image-classification CNN will be explored to predict range and level for THG resonance wavelength and intensity of pixelated MSs, respectively, in the Si-based research part.

1.4 Thesis Outline

This dissertation is devoted to the development of a hybrid platform for wideband reconfigurable photonic MMs and MSs based on PCMs and Si, which has potential for applications of NL imaging, microscopy, communication, computing, and information processing.

Chapter 2 numerically and experimentally demonstrates an asymmetric Fabry-Perot (F-P) cavity device with subwavelength features for broadband-tunable THG using the GST. The structure demonstrated provides the first truly wideband-tunable THG devices and paves the way for the design of NL optical structures with improved efficiency and functionality for a wide range of applications, such as a combined band-and-phase modulation for THG imaging and microscopy.

Chapter 3 numerically designs a wideband tunable THG device and experimentally demonstrates an efficient tunable SHG device by integrating GST with a plasmonic MM. This advocates more sophisticated designs for further improved frequency conversion efficiency, which might be applicable to NL microscopy, communication, and computing.

Chapter 4 numerically and experimentally demonstrates an a-Si MS tuned by an asymmetric F-P GST subwavelength cavity device for a large THG modulation depth. The

results show the high potential of PCM-based devices for realization of fast dynamic THG switches and pave the way for applications such as THG communications and computing.

Chapter 5 numerically studies an all-Sb₂S₃ MS to co-focus FH and TH signals of tunable foci with a high dynamic range, which can inspire the field of imaging and information processing with reconfigurable NL metalenses.

Chapter 6 numerically designs and experimentally demonstrates a bidirectional symmetry-breaking a-Si MS for efficient THG by featuring a novel and robust quasi-BIC scheme. The presented design outperforms most state-of-the-art demonstrations in terms of nearfield enhancement with high tolerance to fabrication errors. There is observable reconfigurability of the THG resonance at different pump intensity levels. This paves the way for all-optical modulation of THG and its application in NL computing.

Chapter 7 presents a novel strategy for the prediction of resonant THG wavelength and intensity for a type of free-form Si MSs using an image-classification-targeted CNN. This method compensates for the time consumption and relatively large numerical errors in electromagnetic simulations of frequency conversions. It can facilitate faster selection processes for effective NL applications at certain wavelength ranges.

Chapter 8 briefly summarizes the achievements of this dissertation work and discusses outlook for fabrication process optimization of the studies, potential expansion of the hybrid platform for wideband reconfigurable NL MMs to more optical processes, and applications of reconfigurable NL metaphotonics. Dynamic THG/SHG imaging and THG holographic applications are envisioned.

CHAPTER 2. BROADBAND-TUNABLE THG WITH AN ASYMMETRIC F-P GST CAVITY

This chapter summarizes the numerical and experimental demonstrations of a broadband-tunable subwavelength THG device with an asymmetric F-P cavity based on the PCM GST, leveraging intermediate crystallinity states of GST. The experimental demonstration shows the first truly wideband-tunable THG device, having potential for applications such as NL optical microscopic and communication. The content of this chapter is assembled from Refs. [136] and [137] published by the author.

2.1 Introduction to Dynamically Controlled THG with Chalcogenide Nanodevices

Third-order NL optical processes [92], such as THG [64] and four-wave mixing (FWM) [138] have been widely researched due to their potential for highly efficient frequency conversion with easily-obtained centrosymmetric media [92]. Notably, THG can generate light of shorter wavelengths than those of SHG; it can even extend the wavelength range of converted light to deep ultraviolet [139]. Ultra-compact NL optical sources demand photonic nanostructures to manipulate light at the subwavelength scale. A highly desired feature is spectral tunability (or reconfigurability) of the NL response. Very limited research has been focused on reconfiguration of the frequency band of NL generation due to the need for significant modulation of the NL refractive index. Well-known NL optical effects, such as Pockels and Kerr effects, are greatly limited by the available electro-optic coefficients and NL indices of refraction, respectively [92], of the conventional NL optical materials. Cao *et al.* [87] elicited the insight of giant THG modulation at a fixed frequency

band with a simple asymmetric quarter-wave-resonant layer [140] of GST on an Au reflector. They obtained a THG efficiency of 5.46×10^{-11} with a maximum unsaturable pump power of 13.37 mW at the fundamental wavelength (λ_f) of 1450 nm. More recently, Liu *et al.* utilized the gap plasmon resonance to greatly enhance THG nearfield in GST aiming at fixed-band dynamic control of THG [141].

Chalcogenide glasses are a class of amorphous semiconductors widely used in phase-change memories [51], especially in rewriteable optical data storage and electronic flash memories. The well-known phase-change alloy germanium antimony telluride, $\text{Ge}_2\text{Sb}_2\text{Te}_5$ (in short, GST), has been of great interest lately for nanophotonic [42, 59, 142-144] and terahertz metaphotonic [145] applications due to its very large change in the index of refraction through conversion between amorphous and crystalline states, especially in the NIR wavelength range. In addition, the refractive index of GST can be selectively controlled within the intermediate states between the terminal amorphous and fully crystalline states. Correspondingly, with the increase of electric conductivity during crystallization, the extinction coefficient of GST grows. Due to the large changes in the optical and electronic properties, the subwavelength scalability (down to 10's nanometers), reasonably fast switching speed (10's-100's nanoseconds) [146], high switching robustness (up to 10^{15} cycles) [55], nonvolatility (and thus, power efficiency), high thermal stability, and compatibility with the CMOS fabrication technology, GST is highly desirable for large-scale reconfigurable integrated networks [52]. There is reported research utilizing the increased loss at the crystalline GST (c-GST) state to exhibit THG off-state hybridizing with a Fano-resonant a-Si MS, while the THG response at the less lossy amorphous GST (a-GST) state represents the on-state [147].

Additional to large refractive indices of a-GST and c-GST, the third-order NL optical susceptibilities ($\chi^{(3)}$ s) of GST at the NIR wavelengths [148] are comparable to that of the widely used a-Si ($\sim 2.79 \times 10^{-18} \text{ m}^2/\text{V}^2$) [101, 149]. Thus, nanoscale devices with GST as the $\chi^{(3)}$ media can potentially enable reconfigurable NL devices with reasonably high THG conversion efficiencies and increased nonlinearity. We demonstrate such an important capability by integrating GST into a resonance-enhanced asymmetric quarter-wave F-P cavity.

2.2 Design and Fabrication of the F-P GST Cavity

The schematic of the asymmetric F-P device under study is illustrated in Figure 2(a). The device is comprised of four layers. A layer of Au as the back reflector is first deposited on a Si substrate. The Au layer is followed by a sandwiched structure of silicon dioxide (SiO_2)-GST- SiO_2 . The simulated thickness of the GST layer (t_{GST}) is set to 10 nm, 15 nm, or 20 nm as a design parameter to control the tuning range. The bottom SiO_2 layer is optically thick enough to guarantee the coherent interference of the incident and reflected linear signals at the GST layer. The thickness of the bottom SiO_2 layer (t_{bo}) is set to 10 nm, 25 nm, and 50 nm for different simulations. The top SiO_2 layer serves as a capping layer to protect the GST layer from oxidation and provide additional THG tunability. The thickness of the top SiO_2 layer (t_{to}) is considerably smaller than the TH wavelengths (λ_{TH}) of interest (370 nm to 530 nm). In different simulations, t_{to} is selected to be 10 nm, 50 nm, or 100 nm. For the sake of simplicity, we numerically study plane-wave excitation with only normal incidence from the air as shown in Figure 2(a). The reflected THG response is simulated using the finite element method (FEM) through the full-wave electromagnetic

modeling software COMSOL Multiphysics, which is also used in all other numerical simulations in this thesis.

There are 3 different crystallinity states of GST (i.e., amorphous, crystalline, and a semi-crystalline state) considered in the simulations. These GST states and the real and imaginary parts of their refractive index are shown in Figure 2(b). These indices are used in all other simulations with the 3 crystallinity states of GST in this thesis. Material settings in the simulations are as follows. Refractive indices of amorphous and fully crystalline states of GST in the wavelength range of 370–1700 nm are calculated from ellipsometry data of experimentally deposited GST samples at the Institute of Electronics and Nanotechnology (IEN) at Georgia Tech. The effective medium theory represented by the

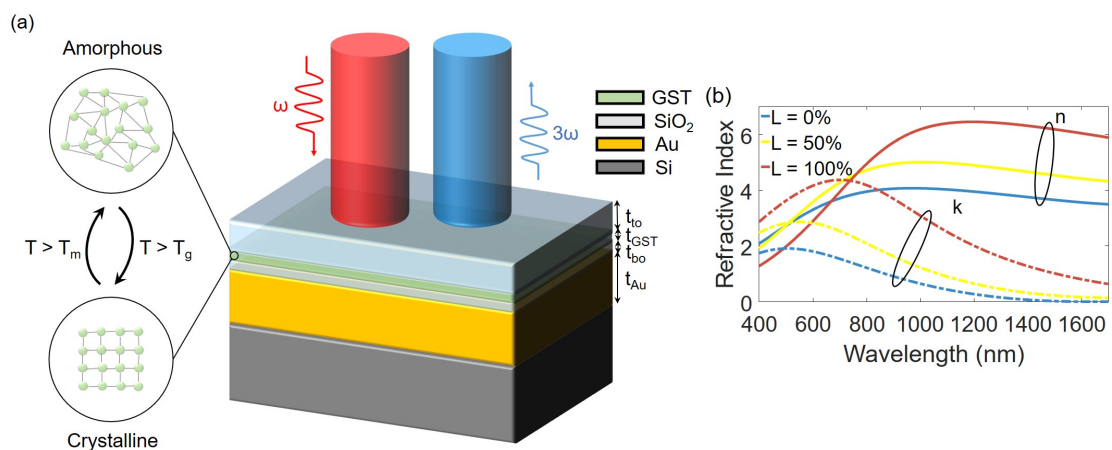


Figure 2 – (a) Schematic of the planar F-P-based NL device with operation under the normal-reflection mode. The thicknesses of the layers in this multilayer structure from bottom to top for all simulations in this subsection are 500 nm (Si), 100 nm (Au), 10, 20, or 50 nm (SiO₂), 15-35 nm (GST), and 10, 50, or 100 nm (SiO₂). The inset shows the schematic of GST in crystalline and amorphous states. T_g and T_m are the glass and melting temperatures of the PCM in schematic pictures throughout this thesis. (b) Real (n, solid curves) and imaginary (k, color-correspondent dashed) parts of refractive index of the 3 different crystallinity states of GST with different percent crystallization shown by L. The data for the amorphous and fully crystalline states is measured by ellipsometry of deposited GST samples. The property of the intermediate state is calculated using the Lorentz-Lorenz formula.

Lorentz-Lorenz formula [150] was exploited to calculate the refractive index of GST in the intermediate crystallinity states. It has been experimentally shown that by precisely controlling the annealing time of GST using an external stimulus, several intermediate states can be readily achieved [142]. The complex refractive index of Au is adopted from Johnson and Christy's experimental data [151] and used in all modeling of Au in this thesis. The refractive index of SiO₂ is also taken from measurement data [152]. The $\chi^{(3)}$ of GST is assumed to be isotropic and homogeneous for all states. An experimental study shows that $\chi^{(3)}$ of c-GST ($\chi^{(3)}_{\text{c-GST}}$) is about 12 times that of a-GST ($\chi^{(3)}_{\text{a-GST}}$) [87]. These settings of GST $\chi^{(3)}$ s are used throughout THG simulations of GST in this thesis. According to that $\chi^{(1)} \sim n^2 - 1$ for non-magnetic media in limited electric fields, and the empirical Miller's rule that $\chi^{(3)} \propto (\chi^{(1)})^4$, where $\chi^{(1)}$ is the first-order optical susceptibility of the material [90], we estimate in-plane $\chi^{(3)}$ of L = 50% GST $\sim 3.5 \chi^{(3)}_{\text{a-GST}}$. The $\chi^{(3)}$ of Au is not taken into account due to negligible field magnitude compared to that in the GST layer. The $\chi^{(3)}$ of SiO₂ with a refractive index of less than half of that of GST is also negligible. The THG simulation is composed of two steps. The linear optical electric field vector ($\mathbf{E}(\omega)$) under plane-wave excitation at radian frequency ω is first calculated. Then, the THG polarization at each mesh point of the GST domain is calculated as $\mathbf{P}(3\omega) = \epsilon_0 \chi^{(3)} \mathbf{E}(\omega) \cdot \mathbf{E}(\omega) \cdot \mathbf{E}(\omega)$, where ϵ_0 is the vacuum permittivity. The THG polarization of GST serves as a source for the electromagnetic field simulation at the third-harmonic (TH) frequency. Since the optical field of the TH signal is very small compared to the linear optical field at the pump frequency, pump depletion is not considered. This THG simulation method is also used in all other THG simulations in this thesis. In this study, the 2D mesh element sizes are set to be no larger than 1/18 of the λ_f in each medium to ensure an accurate calculation.

We fabricated the as-grown samples by consequent electron-beam (e-beam) evaporations of the Au reflector and the bottom SiO₂ layer ($t_{Au} = 100$ nm and $t_{bo} = 10$ nm, 25 nm, or 50 nm), radio-frequency (RF) magnetron sputtering of ~ 15 , 20, and 25 nm-thick GST (~ 5 nm-thick low-index GST oxide upon immediate exposure to air [153] is considered), and the e-beam evaporation of the top SiO₂ layer ($t_{to} = 10$ nm, 50 nm or 100 nm) on a prime Si substrate. All e-beam evaporation processes in this thesis were conducted with a Denton Explorer system and all GST sputtering processes in this thesis were conducted with a Chalcogenide Materials Sputterer at the IEN. A flowchart of the fabrication process for the as-grown samples is shown in Figure 3.

The non-a-GST samples were obtained with controllable annealing to semi-c-GST and c-GST states on a hotplate at $\sim 145^\circ\text{C}$ and $\sim 250^\circ\text{C}$ for 10 minutes, respectively. The annealing condition for $L = 50\%$ was obtained through calibration studies using different annealing temperatures and times. In each step, the crystallinity percentage (L) is identified through ellipsometry measurements and comparison with the GST refractive index approximated by Lorentz-Lorenz formula with the measured ellipsometry results of $L = 0\%$ and $L = 100\%$ cases. The annealing conditions for GST crystallization are used throughout the thesis.

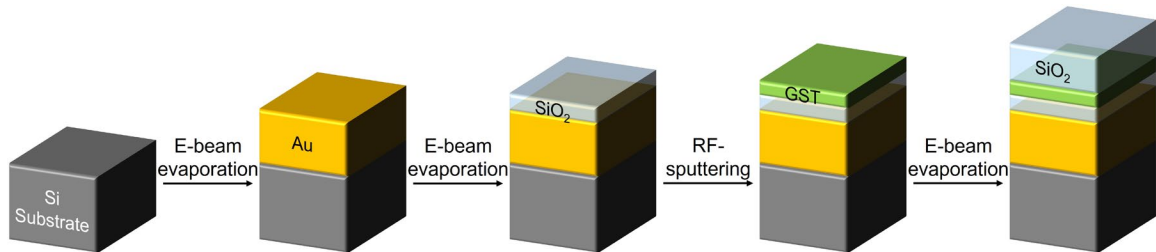


Figure 3 – Fabrication process for the as-grown asymmetric F-P cavity structure, in which e-beam evaporations and RF-sputtering were conducted.

2.3 Results and Discussion on the Device

Simulated linear reflectance spectra and THG spectral responses of the structure in Figure 2(a) with $t_{\text{GST}} = 20$ nm for the three investigated GST states are shown in Figure 4(a) and Figure 4(b), respectively. The resonance bands at different values of L in Figure 4(b) clearly demonstrate the broadband THG modulation possibility. Less overshadowing of resonance bands happens at longer wavelengths that correspond to GST states with larger L and higher values of $\chi^{(3)}$ and refractive index (and thus, higher field confinements). Note that the increased loss at larger L is overcome by the increase in $\chi^{(3)}$. The measured linear and THG spectra of the corresponding fabricated samples with $t_{\text{GST}} \sim 25$ nm (considering the 5 nm oxidation layer) are shown in Figure 4(c) and Figure 4(d), respectively. The measured data are comparable to the simulation results, although the measured THG resonance bands are narrower than the simulated ones. We believe the discrepancy between simulation and experimental results (see Figure 4(a) and Figure 4(c), Figure 4(b) and Figure 4(d)) is primarily due to the fabrication imperfections including the relatively rough GST surface resulted from ion bombardment during sputtering. Annealing for GST phase change can add to the surface roughness resulting in increased discrepancy at larger values of L . The discrepancy at $L = 100\%$ becomes particularly remarkable as the blue-half of the reflection spectrum is almost flat, which complicates identifying the resonance. Nevertheless, a shallow dip between wavelengths of ~ 1000 nm and ~ 1200 nm can be identified through a closer look at the reflection spectrum (see Figure 4(c)). Our a-GST sample has a resonant THG efficiency of 4.52×10^{-11} at a peak pump intensity of ~ 0.8 GW/cm². This efficiency is comparable to the peak THG efficiency reported on a planar a-GST nano-cavity (5.46×10^{-11}) [87] at a similar resonance band and a larger estimated

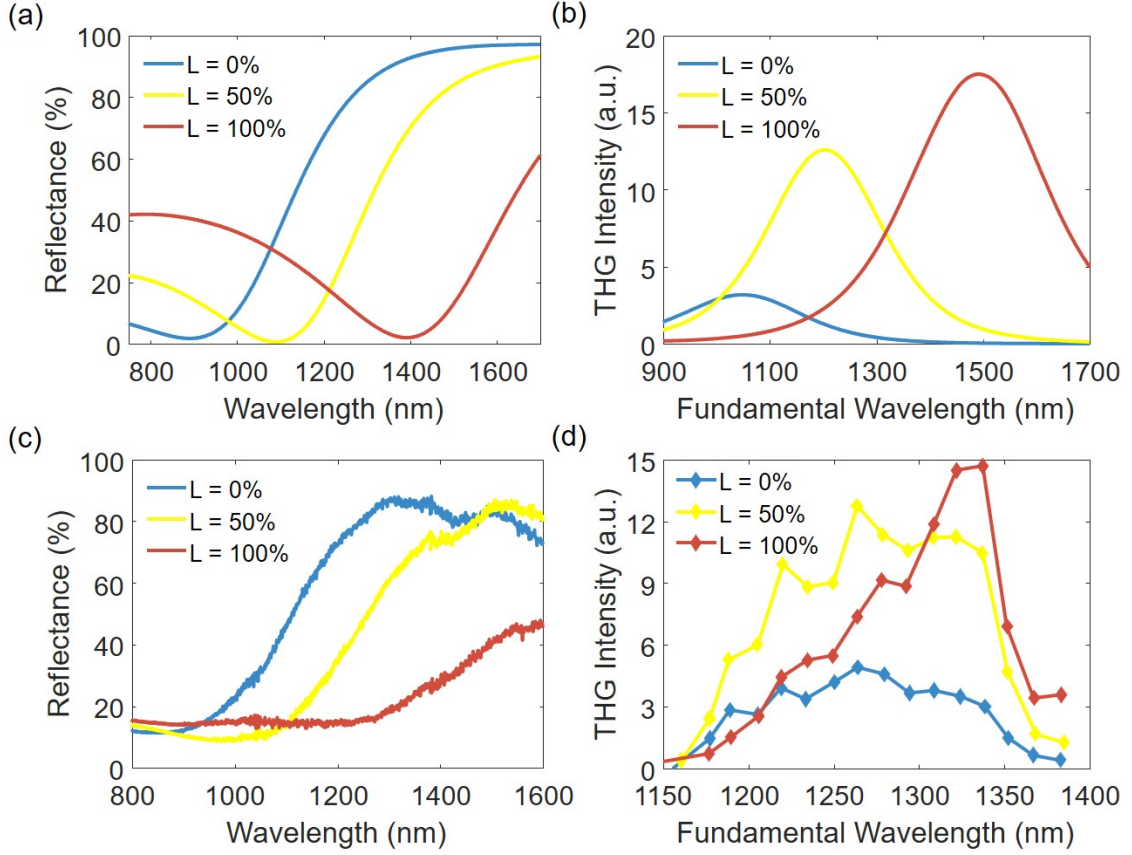


Figure 4 – Simulated (a) reflectance spectra, and (b) THG spectral responses of the asymmetric F-P structure in Figure 2(a) for different GST crystallinities (L) with $t_{\text{bo}} = 25$ nm, $t_{\text{GST}} = 20$ nm, and $t_{\text{to}} = 50$ nm. Measured (c) reflectance spectra and (d) THG spectral responses of the corresponding fabricated sample with $t_{\text{GST}} = 25$ nm, considering the GST oxidation effect.

peak pump intensity (~ 3 GW/cm²).

To study the possibility of broadband THG modulation using devices with compressed GST thicknesses, we compare the measured linear reflected and THG spectra with simulated responses for $t_{\text{GST}} = 10$ nm and for $t_{\text{GST}} = 15$ nm while keeping $t_{\text{bo}} = 25$ nm and $t_{\text{to}} = 50$ nm (see Figure 5 and Figure 6). The resonance bands for both cases (Figure 5(a) and Figure 6(a)) are substantially blue-shifted compared to those in Figure 4(a) due to the smaller t_{GST} . Since THG resonances for larger-L (higher $\chi^{(3)}$) GST with $t_{\text{GST}} = 10$ nm

(see Figure 5(b)) shift to the center of the fundamental wavelengths of interest (1100–1700 nm), substantial overshadowing of THG resonance bands happens at the fundamental wavelengths of interest. The measured linear and THG spectra of the corresponding fabricated samples with deposited GST thickness of ~ 15 nm (considering the GST oxidation effect) are shown in Figure 5(c) and Figure 5(d), respectively. The agreement between the measured and the simulated results is worse than that for the $t_{\text{GST}} = 20$ nm design. This is due to the reduced controllability of the roughness and uniformity at the extremely low sputtering deposition thickness of ~ 15 nm. There is also a possibility of a

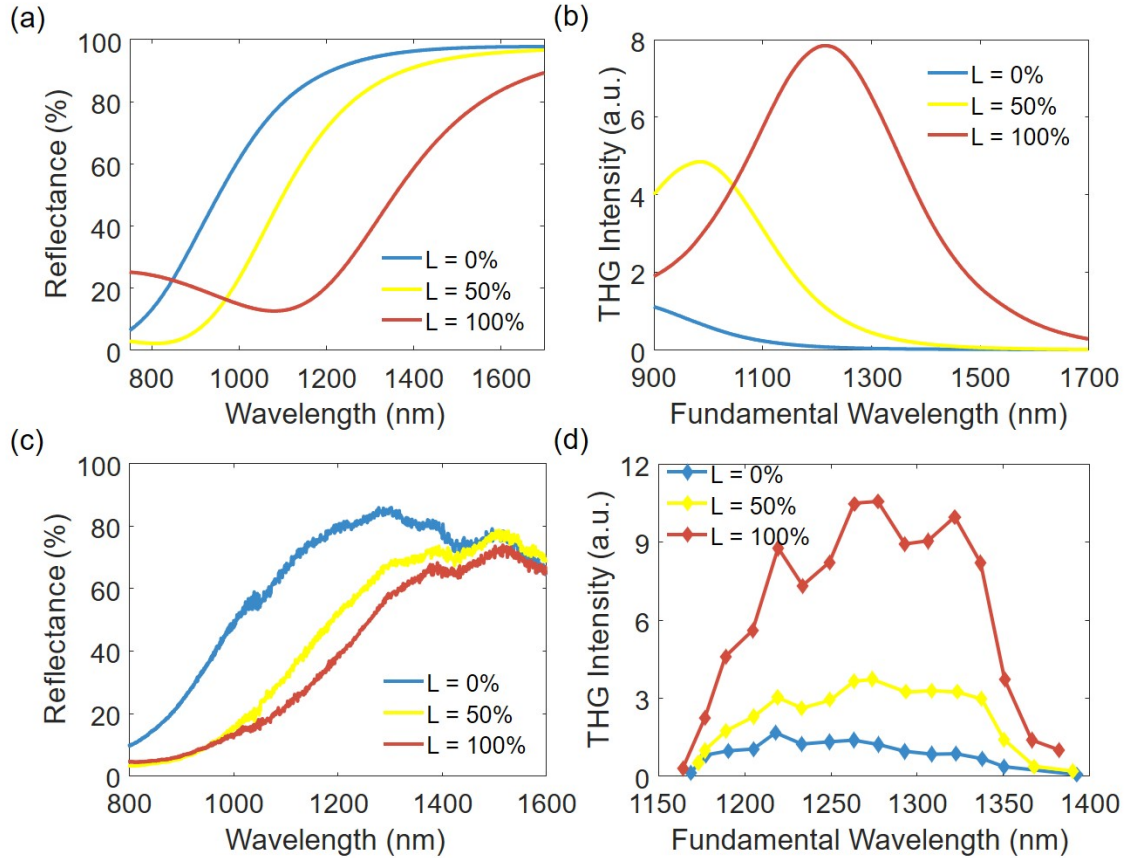


Figure 5 – Simulated (a) reflectance spectra, and b) THG spectral responses of the asymmetric F-P structure in Figure 2(a) with different L , $t_{\text{bo}} = 25$ nm, $t_{\text{GST}} = 10$ nm, and $t_{\text{to}} = 50$ nm. Measured (c) reflectance spectra, and (d) THG spectral responses of the corresponding fabricated samples with $t_{\text{GST}} \sim 15$ nm, considering the GST oxidation effect.

larger contribution of interfacial THG hotspots with increased GST/SiO₂ roughness at annealed GST states with larger values of L, which results in almost complete overshadowing of the THG responses compared to those at GST states with smaller values of L over the wavelength range of interest.

In comparison, the simulated linear reflectance spectra and THG spectral responses of the structure in Figure 2(a) with $t_{\text{GST}} = 15$ nm for the three GST states are shown in Figure 6(a) and Figure 6(b), respectively. The corresponding measurement results for the

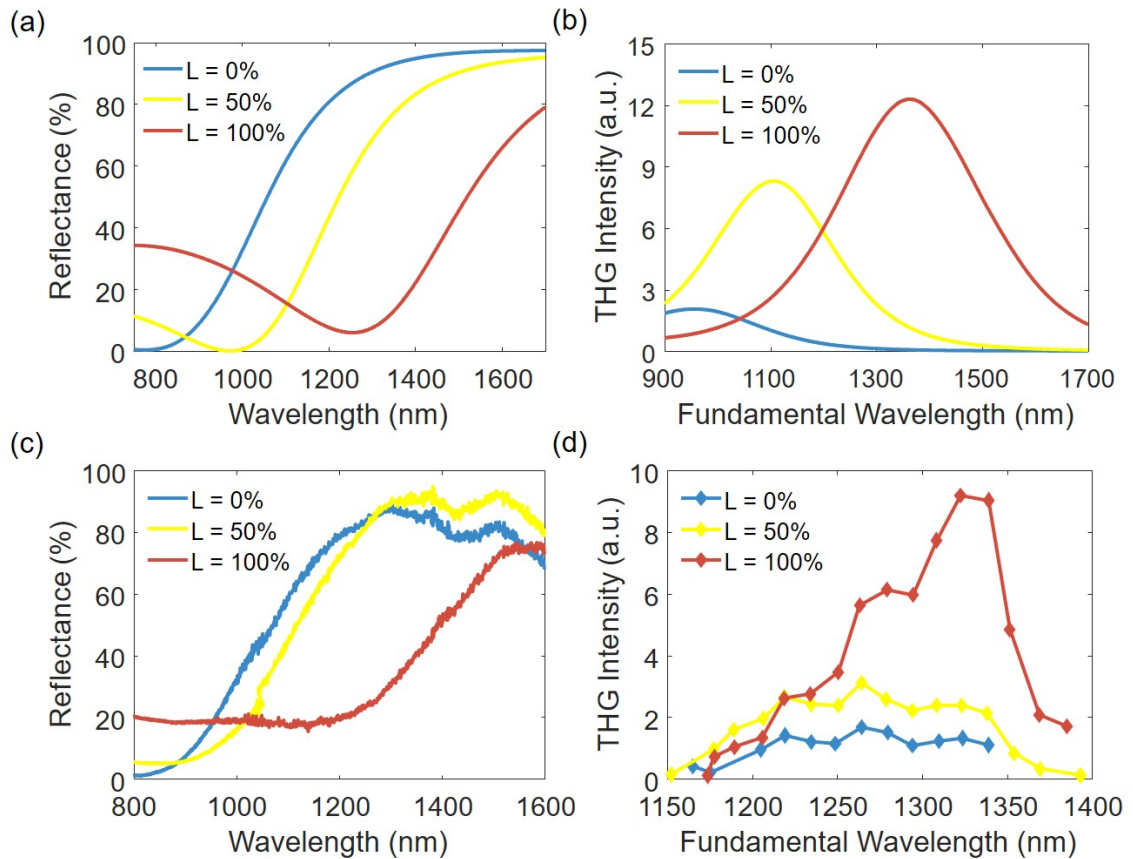


Figure 6 – Simulated (a) reflectance spectra, and (b) THG spectral responses of the structure in Figure 2(a) of different L, $t_{\text{bo}} = 25$ nm, $t_{\text{GST}} = 15$ nm, and $t_{\text{to}} = 50$ nm. Measured (c) reflectance spectra, and (d) THG spectral responses of the corresponding fabricated samples with $t_{\text{GST}} \sim 20$ nm, considering the GST oxidation effect.

deposited GST thickness of ~ 20 nm (considering the GST oxidation effect) and the investigated GST states are shown in Figure 6(c) and Figure 6(d), respectively. The linear and THG resonance band positions and the comparability of measurement results with simulations are between those of the structures with $t_{\text{GST}} = 10$ nm and $t_{\text{GST}} = 20$ nm as expected.

To further study the role of the thicknesses of different layers of the F-P structure in Figure 2, we numerically study the effect of the variation of the structural parameters on the THG response. The first step is to find the fundamental wavelength at the THG resonance and the resonant THG intensity. The second step is to calculate the THG Qs for the simulated THG responses for different values of L s at different t_{GST} mentioned above. The THG Q is defined as the ratio of the resonance (or peak) frequency to the full-width-at-half-maximum (FWHM) of the THG spectrum. Figure 7(a) shows the simulated resonant THG intensity and THG Q at different fundamental wavelengths at THG resonance for the asymmetric F-P structure with different thicknesses of the GST layer. This plot suggests that using thinner GST layers (e.g., $t_{\text{GST}} = 10$ nm) results in a larger variation of the resonant THG intensity with L while exhibiting an overall lower THG intensity. On the other hand, using relatively thicker GST layers can result in larger THG intensities with a smaller range of variation with L . Thus, a relatively thicker GST layer is a plausibly better choice for achieving more efficient broadband tunable THG. Figure 7(a) also shows the powerful design flexibility that our structure provides by only changing the GST thickness. In addition, the THG Qs for phase-variant resonances of each thickness in Figure 7(a) exhibit a smaller rate of increase with increasing L from $\lambda_f = 1200$ nm to $\lambda_f =$

1400 nm compared to the rest of the observed spectrum, due to the considerably larger GST losses at the corresponding range of λ_{TH} .

The variation of t_{bo} and t_{to} can also modify the resonance bands significantly as shown by Figure 7(b) and Figure 7(c), respectively. It is observed that a larger t_{bo} induces a redshift on the resonance (see Figure 7(b)) due to the larger optical length of the cavity. Moreover, a fixed-thickness GST layer that is only a few 10s of nanometers away from the Au reflector can potentially make use of more constructive interference to greatly increase the resonance amplitude, compared to the case that the GST layer is placed closer to the Au reflector (or directly on top of it). Thus, the resonance intensities for $t_{bo} = 50$ nm in Figure 7(b) can be considerably larger than those for $t_{bo} = 10$ nm. The selection of t_{to} can also impact the modulated THG bands, although not as strongly as t_{bo} can (see Figure 7(c)). With a smaller refractive index compared to GST, the top SiO₂ layer works as a transparent window for the optical input and output to the F-P cavity. Thus, the variation of t_{to} does not significantly induce the resonant-band shifts as that of t_{bo} . As it can be noticed from Figure 7(c), the resonance-band shifts for the fundamental wavelengths are only about 50 nm for t_{to} varying from 10 nm to 100 nm. This small shift is caused by the change in the amplitude of the field inside the GST layer through changing t_{to} . The thickness of the top SiO₂ layer thus has a lower impact on the total THG spectral response. Comparing Figure 7(b) and Figure 7(c) clearly suggests that the thickness of the bottom oxide layer (t_{bo}) is a stronger design parameter than that of the top oxide layer for controlling the THG response.

Investigation of THG resonant nearfield profiles of the F-P structure can consolidate understandings on the reason for comparable THG bands in resonant amplitude at different GST crystallinities for the selected design parameters. Simulated THG resonant

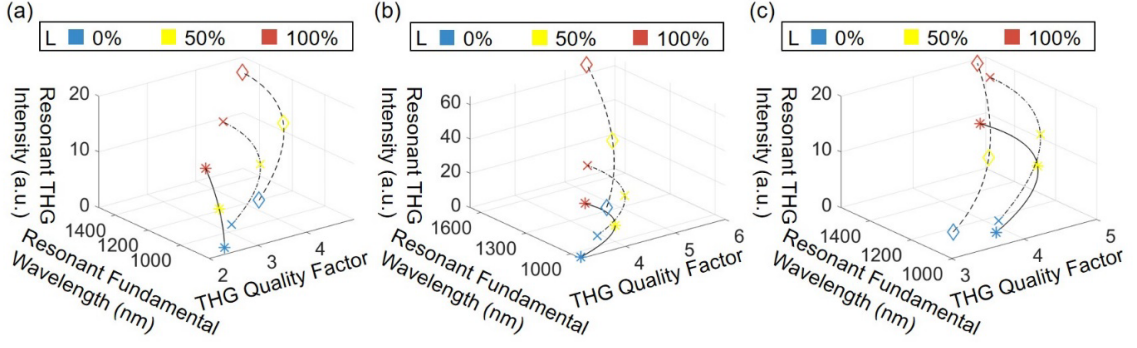


Figure 7 – Plots of simulated resonant THG intensity and THG Q at different resonant fundamental wavelengths for the asymmetric F-P structure in Figure 2(a) with different values of L, with (a) $t_{GST} = 10$ nm (asterisk), $t_{GST} = 15$ nm (cross), $t_{GST} = 20$ nm (diamond), and with $t_{bo} = 25$ nm and $t_{to} = 50$ nm for all cases; (b) $t_{bo} = 10$ nm (asterisk) and $t_{bo} = 25$ nm (cross), $t_{bo} = 50$ nm (diamond), and with $t_{GST} = 20$ nm and $t_{to} = 50$ nm for all cases; and (c) $t_{to} = 10$ nm (asterisk), $t_{to} = 50$ nm (cross), $t_{to} = 100$ nm (diamond), and with $t_{bo} = 25$ nm and $t_{GST} = 20$ nm for all cases. The arbitrary units (a.u.) in (a), (b), and (c) represent the same normalization for the conversion efficiency.

nearfield profiles of the structure in Figure 2(a) with $t_{bo} = 25$ nm, $t_{GST} = 20$ nm, and $t_{to} = 50$ nm for the a-GST and c-GST states are plotted in Figure 8(a) and Figure 8(b), respectively. Both the linear electric field amplitude (normalized to the incident field) and the THG electric field amplitude in arbitrary units (a.u.) are plotted in each sub-figure, where the a.u. in Figure 8(a) represents an identical field amplitude to that in Figure 8(b). It is clear that the linear field strength in the GST layer for the a-GST structure is considerably larger than that for the c-GST structure. This is possibly due to the larger loss of c-GST compared to a-GST at the fundamental wavelengths. Also, the a-GST structure exhibits a more coherent THG output (see the air region on top of the structure in Figure 8) than the c-GST structure as the field amplitude of THG output in air is ~ 1.5 (1.25) times that in the a-GST (c-GST) layer at resonance, as seen from the right of Figure 8(a) (Figure 8(b)). These effects partially compensate for the effect of $\chi^{(3)}_{c-GST}$ being much larger than $\chi^{(3)}_{a-GST}$, resulting in comparable resonant THG outputs of the device at the extreme states ($L = 0\%$

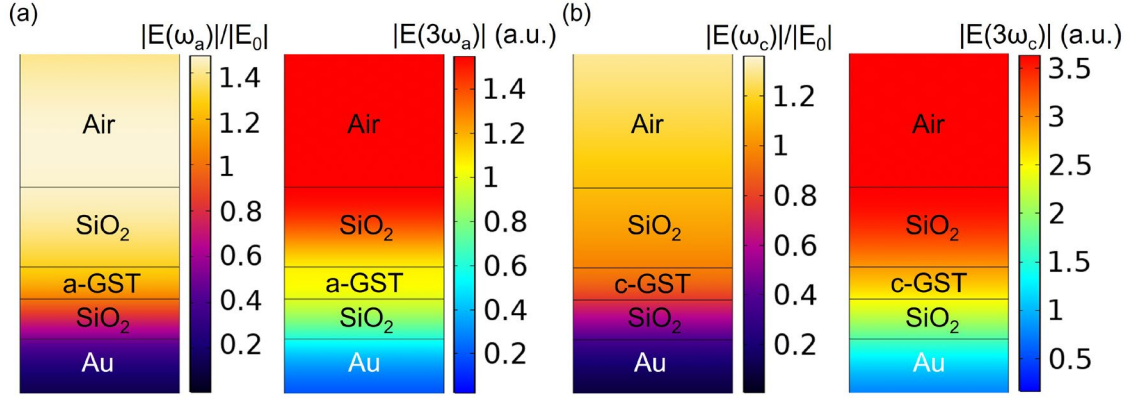


Figure 8 – Plots of simulated linear nearfield normalized to the incidence (left) and THG nearfield in an a.u. (right) for the asymmetric F-P structure in Figure 2(a) for the (a) a-GST state and (b) c-GST state with $t_{\text{bo}} = 25$ nm, $t_{\text{GST}} = 20$ nm, and $t_{\text{to}} = 50$ nm. The extent of all materials is marked by solid lines. ω_a and ω_c are angular frequencies for the fundamental wavelengths of 1050 nm and 1500 nm at THG resonances for the a-GST and c-GST states, respectively.

and $L = 100\%$). This is also observed in Figure 8, which shows that the resonant THG output field for the c-GST structure is only ~ 2.3 times larger than that of the a-GST structure.

2.4 The Characterization Setups and THG-Excitation Power Dependence

The characterizations are done with a modified version of the setups in Ref. [154]. All linear characterizations in this thesis were done with an incandescent white light source, a $10\times$ objective lens ($\text{NA} = 0.25$), and an InGaAs linear array detector coupled with a spectrometer. Reflectance spectra were normalized by the reflected power of sample control areas of simply 100 nm-thick Au on the substrate. The THG characterizations were conducted with an optical parametric oscillator (OPO) of 1100–1600 nm tuning range and a Si charge-coupled device. The OPO is pumped by a Ti:Sapphire laser (150 fs pulse duration and 80 MHz repetition rate, Coherent Chameleon), and used in all NL characterizations in this thesis. The $10\times$ objective lens and a pin hole of a ~ 0.8 -mm

diameter in front of the objective lens was used to make an approximate normal incidence. Figure 9 and Figure 10 show detailed setup schematics including the optical paths of the linear and THG characterizations, respectively.

Figure 11 presents excitation power (i.e., pump power) dependence of the measured

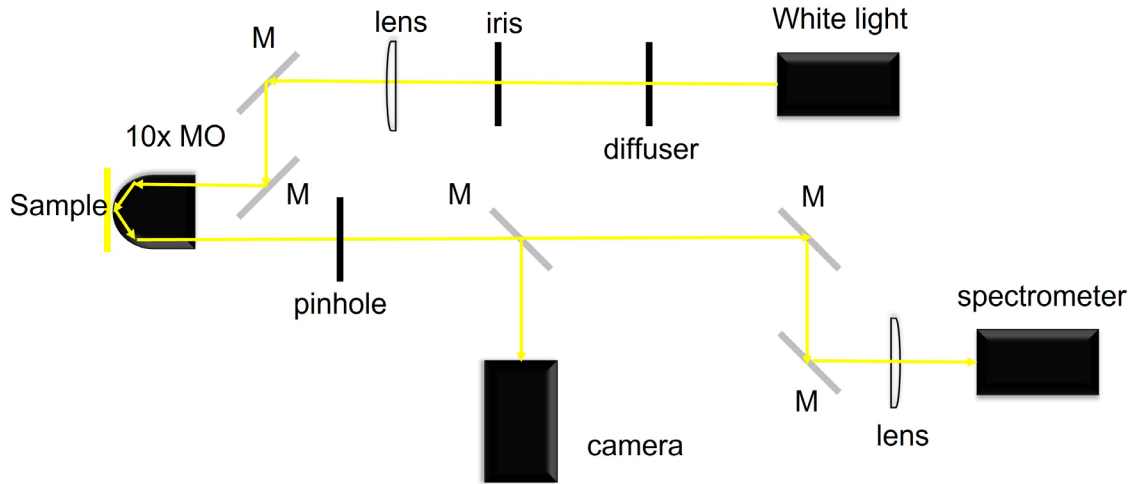


Figure 9 – The setup schematic for the reflectance measurement of the GST F-P cavity devices, where ‘M’ and ‘10× MO’ represent a mirror and the 10× microscopic objective lens, respectively.

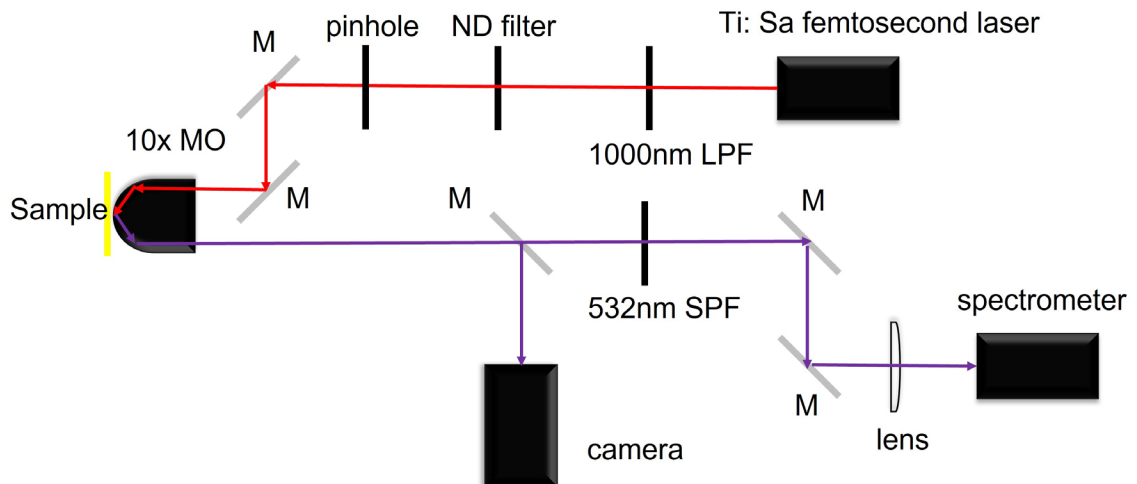


Figure 10 – The setup schematic for the THG measurement of the GST F-P cavity devices, where ND, LPF, and SPF represent neutral density, long-pass filter, and short-pass filter, respectively.

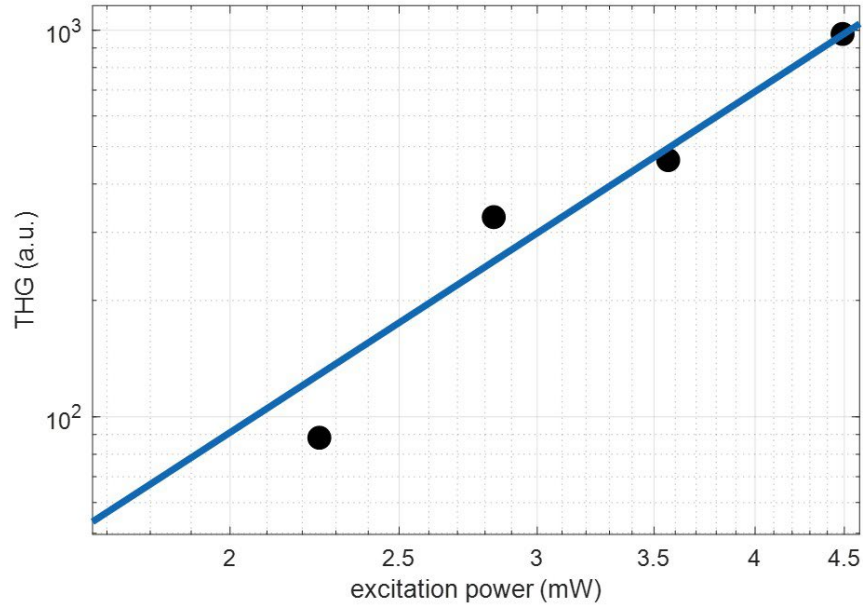


Figure 11 – Excitation power (i.e., pump power) dependence of the measured THG intensity from the a-GST sample of the structure in Figure 2(a) with deposited GST thickness ~ 20 nm at the excitation $\lambda_f = 1215$ nm. A power-law fit is applied to the measured data. The slope of the fit is 2.93 ± 0.15 at a confidence level of 95%, in agreement with the expected slope of 3 for THG. The excitation power was measured immediately after the ‘10 \times MO’ in Figure 10 without the sample. All fittings in this thesis are estimated at the 95% confidence.

THG intensity from the a-GST sample of deposited GST thickness ~ 20 nm at the excitation $\lambda_f = 1215$ nm. A power-law fit is applied to the measured data. The slope of the fit is 2.93 ± 0.15 , in agreement with the expected slope of 3 for THG. The excitation power was measured immediately after the ‘10 \times MO’ in Figure 10 without the sample. The demonstration of this structure uses the excitation power of ~ 3 mW (the peak pump intensity of ~ 0.8 GW/cm²), which fits in the linear regime shown in Figure 11, and should be safe from NL saturation [155] and GST phase conversion (change of n_0 and $\chi^{(3)}$) upon laser annealing.

2.5 Conclusion and Outlook

In this study, a new device based on an asymmetric subwavelength-scale F-P cavity structure is demonstrated for broadband-tunable THG of λ_f from 1100 nm to 1600 nm numerically as in Ref. [156], and from 1150 nm to 1400 nm experimentally by finely controlling the refractive index of the extreme states and semi-crystalline state of the conveniently controllable PCM GST. The carefully designed resonance-enhanced asymmetric quarter-wave F-P cavity configuration significantly promotes the tunability and THG effects. The demonstrated structure provides the first truly wideband-tunable NL generation devices and inspires the design of NL photonics MMs and MSs with enhanced efficiency and functionality for various applications, e.g., combined band-and-phase modulations for NL imaging, microscopy, and holography. These structures can be combined with ultrafast and compact heating processes using ITO Joule heaters as demonstrated in Refs. [157-159] to form a new platform for electrically tunable chip-scale NL optical devices. The structure here can also be a reliable platform for wideband tuning of THG with higher conversion efficiencies: 1) at the longer infrared wavelengths where the GST optical loss is minimal or 2) by using alloys of GST, e.g., GSST [88, 89], which provide less optical loss at the 1100–1600 nm wavelength range.

CHAPTER 3. DYNAMICALLY TUNABLE HARMONIC GENERATION USING HYBRID PLASMONIC METASURFACES WITH GST

This chapter summarizes a numerical demonstration of wideband tunable THG of resonant fundamental wavelengths from ~ 1100 nm to 1700 nm (Section 3.1) and an experimental demonstration of efficient fixed-band switchable SHG of a modulation depth as high as ~ 20 dB (Section 3.2), by gap-surface plasmon hybridized GST MSs. These pave the way for designs of strong resonances to realize more efficient NL conversion, which might be applicable to NL microscopy, communication, and computing. Section 3.1 is revised from Ref. [160] and Section 3.2 is assembled from Ref. [161], both published by the author.

3.1 Numerical Study of Wideband-Tunable THG Using Hybrid MSs with GST

Due to limited field enhancement in planar high-index F-P cavities, the extension of the broadband-tunable F-P GST device to patterned nanostructures, which exhibit higher surface-to-volume ratios than planar structures, is demanded. The patterned nanostructures are expected to interact with optical harmonics more intensively for dynamic manipulation of NL generations in the subwavelength scale. Liu *et al.* numerically demonstrated THG nearfield intensity enhancement of $\sim 10^5$ in GST with a hybrid metal-insulator-metal (MIM) structure supporting gap-SPRs [141]. Improving the linear nearfield and THG scattering of the GST-based device and resorting to GST states of intermediate crystallinity can lead to a more efficient reconfigurable, ultra-compact, and wide-range THG

nanophotonic source. In this study, the reconfiguration of a GST-based hybrid gap-surface plasmonic MM for wideband-tunable THG is numerically demonstrated with enhanced efficiency compared to the structure in Section 2.2 Figure 2(a). Different plasmonic materials and geometric configurations are studied and selected from, which is to substantially increase resonant THG scattering for enhanced output efficiency.

3.1.1 *Design and Simulations of the MIM MM*

Ag is selected as the plasmonic material for its lower loss than Au at intended operational wavelengths and THG SPR at the a-GST state, compensating for much smaller $\chi^{(3)}_{\text{a-GST}}$ than $\chi^{(3)}_{\text{c-GST}}$. The reconfigurable GST device is composed of an array of Ag/GST nano-disks on an Ag reflector, which can function as a micro-heater, as can be imagined from Figure 12(a). The device is designed for λ_f between 1000 nm and 1800 nm. The Ag reflector is set to be 100-nm thick to prevent light transmission. The Ag/GST nano-disk comprises a 30-nm-thick GST layer and a 90-nm-thick (or a 50-nm-thick for comparison) Ag layer. The diameter of the nano-disk is selected as 100 nm, and square lattice period is selected as 250 nm that is even smaller than TH wavelengths, which will result in normal THG reflection. The surface sulfurization [162] / oxidation of Ag/GST is not considered in this numerical study for the sake of simplicity. The thickness of the Ag nano-disk is set to 90 nm, which is comparable to the diameter to afford stronger THG scattering at shorter wavelengths. The reflected THG flow is calculated through the simulation under normal excitation of a plane wave polarized in one periodic direction of the MS. Au-(a-GST)-Au structure is also simulated for comparison.

There are 6 different crystallinity states of GST (i.e., amorphous, crystalline, and 4 intermediate crystallinity states) considered in the simulations. More intermediate states than that in Section 2.2 Figure 2(b) are studied due to increased complexity of the structure in Figure 12(a). THG spectra might exhibit various characteristics under complicated scattering at fundamental and TH wavelength ranges. These GST states and the real and imaginary parts of their refractive index are shown in Figure 12(b). These indices are used in all other simulations with the 6 crystallinity states of GST in this thesis. $\chi^{(3)}$ s of GST are only taken into consideration for THG simulations in this study, while $\chi^{(3)}$ of Ag/Au is not considered as the optical field at the surface of Ag/Au is negligible compared to that in the GST. The $\chi^{(3)}$ s of the intermediate states in Figure 12(b) are assumed to form an equal-ratio series according to the Lorentz-Lorenz formula [150] and the empirical Miller's rule [90]. The complex refractive index of Ag is adopted from Johnson and Christy's experimental

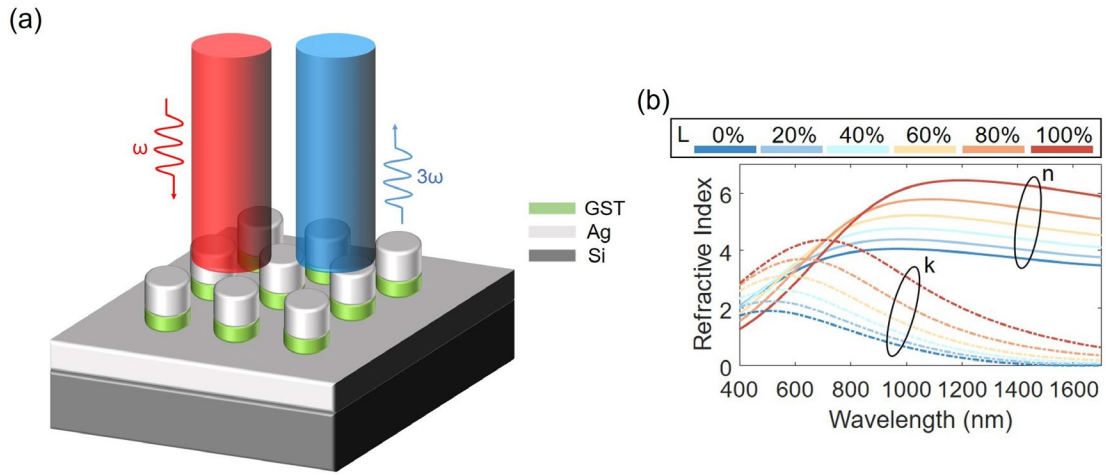


Figure 12 – (a) Schematic of the Ag-GST-Ag device on a Si substrate. The square lattice period and the diameter of the nano-disk are 250 nm and 100 nm, respectively, for all simulations in this numerical study. (b) Real (n , solid curves) and imaginary (k , color-correspondent dashed) parts of refractive index of the 6 different crystallinity states of GST with different percent crystallization shown by L. The data for the extreme and intermediate states are the same and calculated in the same way as Figure 2(b).

data [151]. The incident optical field amplitude in this study is set to only ~ 0.43 times that for the structure in Section 2.2 Figure 2(a) considering generally lower thermal thresholds of plasmonic nanostructures under laser annealing. The mesh element sizes in the device simulations of this study are set to be no larger than $1/10$ of the λ_f in media to ensure an accurate calculation, which are also applied to all other 3D THG simulations in this thesis. This setting is coarser than 2D THG simulations to reduce time consumption.

3.1.2 Results and Discussion

Figure 13 shows the resonant linear and THG nearfields along the plane of incidence for a series of designs with different plasmonic materials (Ag or Au), GST crystallinity, and plasmonic nano-disk thicknesses (T_M where M is the metal) of interest. The linear resonance in a-GST is stronger than that in c-GST due to a much smaller loss in a-GST, as mildly suggested by Figure 13(a) and Figure 13(b). A more vivid observation is the considerably stronger THG hot spots on the edges of the Ag nano-disk in the a-GST

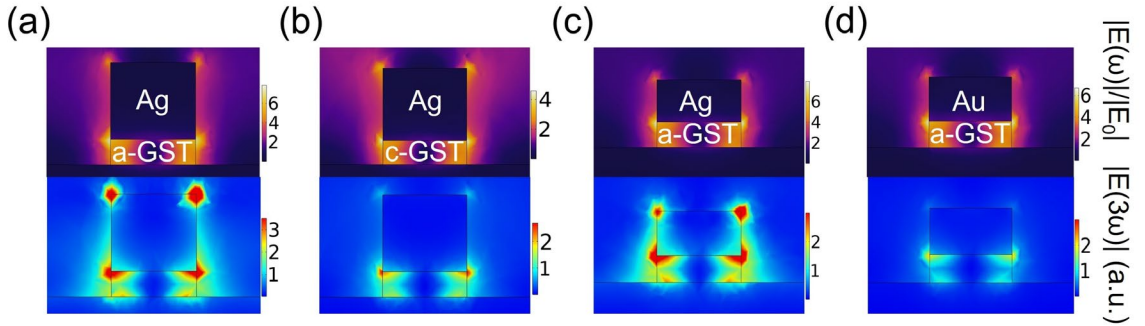


Figure 13 – Simulated side-view normalized nearfields to incidence at resonances (top: linear; bottom: THG $\times 10^4$) for $T_{Ag} = 90$ nm and (a) a-GST state and (b) c-GST state. Nearfields are calculated in the same ways for the a-GST state with (c) Ag plasmonic material with $T_{Ag} = 50$ nm and (d) Au plasmonic material with $T_{Au} = 50$ nm. λ_f values for different nearfield plots are (a) 1120 nm, (b) 1645 nm, (c) 1115 nm, and (d) 1115 nm. All material components of the nano-disks are marked in the plots. The nano-disks are placed on the same metal as the plasmonic nano-disk and surrounded by air for all plots.

case (see Figure 13(a) and Figure 13(b)) despite stronger $\chi^{(3)}_{c-GST}$, as a result of designed SPR. Figure 13(a) and Figure 13(c) suggest that a larger thickness of the Ag nano-disk (90 nm in Figure 13(a) and 50 nm in Figure 13(c)) results in stronger THG hot spots, especially at the edge of the top surface of the plasmonic nano-disk. Comparing Figure 13(c) and Figure 13(d) also reveals that the Ag-based MM has a slightly larger linear field response, however, a considerably enhanced THG response compared to the Au-based structure due to the enhanced scattering at short visible by Ag. The THG of the Ag-(a-GST)-Ag structure turns out to be ~ 10 times that of the Au-(a-GST)-Au structure.

Linear reflection spectra of the structure in Figure 12(a) at the 6 different GST states are shown in Figure 14(a). The gradually broadened reflection ‘dip’ with the red shift of resonance is observed with increasing L as expected, which is like the ‘dip’ broadening in Section 2.3 Figure 4(a). The ‘dip’ is also gradually shallowed with increasing L , due to possibly more decrease in absorption by Au under resonance weakening than increase in

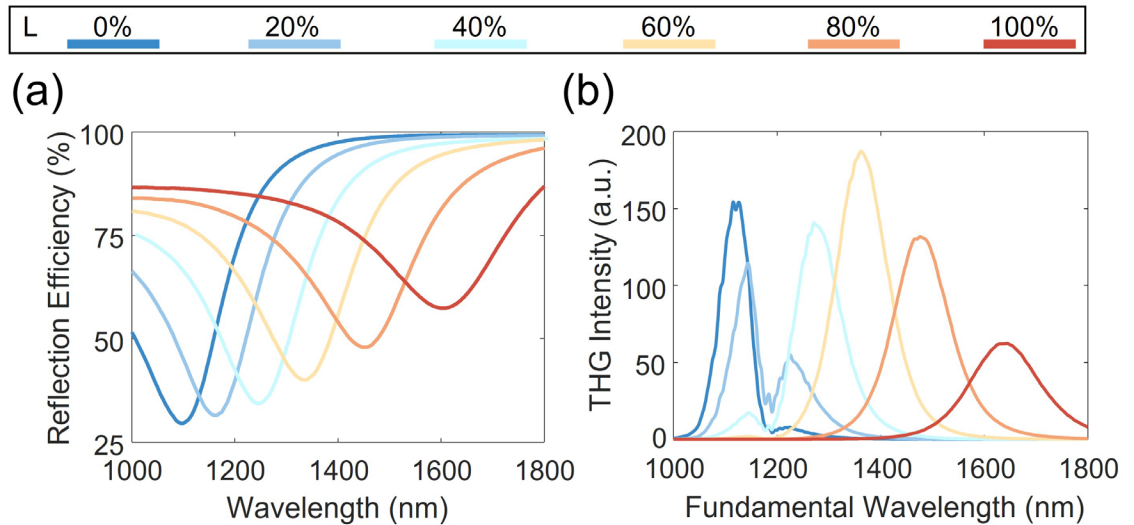


Figure 14 – Simulated (a) reflectance and (b) THG spectra of the structure in Figure 12(a) for the 6 different GST crystallinities (L).

absorption by more-c-GST. Corresponding reflected THG intensity spectra are plotted in Figure 14(b). The a.u. in Figure 14(b) is normalized to that in Section 2.3 Figure 4(b) considering the same incident field amplitude. The unique feature of this structure is its wide effective tuning of the THG resonances from corresponding λ_f of ~ 1100 nm to 1700 nm as seen in Figure 14(b) that match or are very close to the linear resonances in Figure 14(a). This is due to the strong tunability of GST combined with the unique plasmonic structure supporting the strong linear resonance dominating over possible resonances at TH wavelengths in the design. To the best of our knowledge, this is the largest wavelength tunability range for THG reported. In addition, there is substantially less over-shadowing of the resonance bands compared to Section 2.3 Figure 4(b) owing to the designed strong resonance, although more GST states are shown in Figure 14(b). The resonance THG intensities for different GST states are more comparable than those in Figure 4(b) as explained through Figure 13. And the THG output at the a-GST state is significantly larger than that at the c-GST state, suggesting the joint effect of the strong linear resonance and THG scattering at the a-GST states substantially surpasses the impact of the larger $\chi^{(3)}_{\text{c-GST}}$ than $\chi^{(3)}_{\text{a-GST}}$. Existence of resonances of much lower intensity in the vicinity of the primary resonance for more-a-GST states as shown in Figure 14(b) is another indicator for increased THG scattering with the nano-disks of Ag / more-a-GST.

3.1.3 Conclusion and Outlook

A subwavelength-scale wideband-tunable THG device by incorporating the well-known phase-change chalcogenide GST into an Ag-based structure featuring gap-SPR is numerically demonstrated in this work. Tunable THG response of fundamental wavelengths from 1100 nm to 1700 nm is presented with intermediate crystallinity states

of GST, which corresponds to a wide-range THG source from violet to yellow light. The amplitudes of the THG responses are more comparable to those demonstrated with the subwavelength-thick asymmetric F-P cavities in Section 2.3.

This hybrid GST-plasmonic structure advocates more sophisticated designs for applications such as THG microscopy and communication with further enhanced conversion efficiency by design. The structure can also be combined with ITO micro-strip resistors featuring ultrafast heating processes as envisioned for the F-P GST nanocavity device in Section 2.5. ITO is more thermal-resistant than Ag/Au as Joule heaters for chip-scale electro-optical NL devices.

3.2 Switchable SHG Using Hybrid Plasmonic MSs with GST

Considering the large-area sulfurization tarnishing issue of Ag, the difficulty of the lift-off process of plasmonic nano-disks with high aspect ratios of height to width such as in Figure 12(a), and even the structure in Figure 13(d) can be challenging to lift-off, we fabricated only Au-GST-Au samples of ever lower nano-disk thicknesses. THG signals of the samples were not detected due to not only the multiple factors of deficiency discussed above but also GST oxidation. In addition, GST oxidation substantially blue-shifts the resonances to λ_f of ~ 1050 nm to 1100 nm that corresponds to TH wavelengths in the ultraviolet, which is hard to detect.

Orderly structured GST has a high potential for tunable SHG with a non-centrosymmetric crystal structure at the crystalline state, while the amorphous state of GST does not exhibit bulk second-order nonlinearity. SHG signals of the samples were detected,

and the signals are highly switchable with GST crystallinity states as expected and being studied in this section.

3.2.1 Introduction to Dynamically Controlled SHG and THG with Nanodevices

SHG is widely employed in conversion of an optical signal to shorter wavelengths [63, 163] using non-centrosymmetric media [63, 92] and second-order surface nonlinearity [92, 164], originated from the symmetry breaking of the inherent crystal structure of a material [92] and large refractive index differences of materials on the two sides of an interface [165], respectively. This poses special requirements for materials or material interface selections to realize efficient SHG. Nevertheless, SHG is more frequently used than THG for generating light with shorter wavelengths, because SHG is generally a stronger effect, and thus, more efficient than THG [166]. Ultracompact SHG sources demand nanophotonic structures to manipulate light at subwavelength scales with extraordinary optical properties [167] beyond those achieved in bulk materials in addition to strong second-order nonlinearities. Tunable nanophotonic SHGs are typically realized by 1) all-optical modulation induced by Kerr-type coupled resonance shifting [168] and transient symmetry breaking [169] of passive nanostructures, or 2) using an external stimulus to tune the second-harmonic (SH) signal from the nanostructures in real time [77, 170]. However, the reconfigurability of these structures is limited by the relatively small tunability of the second-order optical nonlinearity in passively or actively tunable material configurations.

With fast and large refractive index tunability, PCMs [42, 59, 171, 172] have recently been widely studied for optical reconfigurability in the linear regime and

subwavelength scale. GST, as one of the most widely used PCMs, has garnered widespread interest in nanophotonics [52, 173-175]. The real and imaginary parts of the refractive index of GST can experience changes by over 50% and 10 times, respectively, when switching between a-GST and c-GST states through precisely controlled heating. The relatively high optical loss of GST during crystallization, especially at the visible and NIR wavelengths, is a major obstacle for the performance of GST-based NL optical devices. Yue *et al.* demonstrated MIR-excited THG with a very high efficiency by patterning arrays of subwavelength cylinders made of the lower-loss phase-change chalcogenide GSST and supporting a magnetic dipolar resonance [88]. However, using GSST has the shortcoming of a relatively slow response of the phase change mechanism.

In terms of NL reconfiguration, THG modulation is mostly reported for MMs incorporating GST, where both a-GST and c-GST exhibit third-order nonlinearity. The refractive index, loss, and third-order NL optical susceptibility ($\chi^{(3)}$) of a-GST are substantially smaller than those of c-GST [87] as discussed in Section 2.3. Experimental studies of THG amplitude [87] and band [136] modulations with asymmetric subwavelength F-P cavities have been showcased by incorporating GST as the dominant $\chi^{(3)}$ medium. The details for Ref. [136] are elaborated in Section 2.3. Patterned nanostructures incorporating GST for THG modulations mostly appear in reported theoretical studies due to challenges with associated fabrications. The gap-SPR structure exhibiting an enhanced THG nearfield intensity modulation incorporating GST as the $\chi^{(3)}$ medium [141], and our giant switching design of THG from an all-dielectric Fano-resonant MS modulated by an asymmetric F-P cavity incorporating GST [176] that will be elaborated in Section 4.1, have been reported. More recently, the increased loss at the c-

GST state is utilized [147] to exhibit THG off-state hybridizing with a Fano-resonant a-Si MS, while the THG response at the less lossy a-GST state represents the on-state. In contrast, fewer SHG modulation demonstrations have been reported with GST. The potential for SHG modulation with GST phase change was indicated by a study of tunable grain orientation of GST thin films by exhibiting substantially contrasted SHG responses before and after annealing [177]. A theoretical study leverages GST phase change for manipulating SHG response by adjusting the nearfield in LiNbO₃ nano-resonators in a GST/LiNbO₃ hybrid device [178]. The manipulation principle is based on distinct losses of GST states of different crystallinity as revealed in Ref. [147].

In this study, we seek to leverage metal-GST-metal gap-surface-plasmon resonance (compared with an asymmetric F-P GST nanoscale cavity) and multiple crystallinity states of GST (a-GST, semi-c-GST, and c-GST) to demonstrate efficient three-level SHG switching using the potential high contrast of second-order NL optical susceptibility $\chi^{(2)}$ between a-GST and c-GST states. The design and fabrication of the gap-SPR structure are covered in Section 3.2.2. The design and fabrication of the control structure have been described in Section 2.2 since the F-P cavity structure is the same as that for Figure 6(c). Results are presented and discussed in Section 3.2.3. The settings of experimental characterization and an accepted range of the SHG excitation power are described in Section 3.2.4. Final conclusions and envisions are made in Section 3.2.5.

3.2.2 Design and Fabrication of the MIM MM

The hybrid GST device featuring gap-SPR is composed of an array of Au/GST nano-disks on an Au reflector, as shown in Figure 15(a). The Au reflector is set to be 100-

nm thick as in the structure for Figure 13(d). The Au/GST nano-disk comprises a 25 nm-thick GST layer and a 35 nm-thick Au layer. The diameter of the nano-disk is selected as 120 nm, and the considered periods p of the MS are 220 nm, 250 nm, and 280 nm. The schematic of the asymmetric F-P device is illustrated in Figure 15(b) with the only difference from Figure 2(a) that the structure is studied for SHG instead of THG in this work. The bottom SiO₂, GST, and top SiO₂ layers are fabricated to be ~ 25 nm, 20 nm, and 50 nm, respectively. The bottom SiO₂ / GST layers form the quarter-wave cavity on Au for a λ_f of interest ~ 1150 nm, which can exhibit substantial field interference in the dielectric layers featuring absorption resonance [140], despite the high loss of GST at λ_f of ~ 1150 nm. In addition to serving as a capping layer to protect the GST from oxidation, the top SiO₂ layer also provides a transmission window for SHG emission, as that for THG. As mentioned, GST surface is oxidized upon immediate exposure to air, a GST oxide layer of 10 nm is considered at the top interface (i.e., between GST and Au) of the Au-GST-Au nanostructure as well as on the sidewalls, which is thicker than the 5 nm-thick GST oxide at the GST / top oxide interface considered for the asymmetric F-P cavity structure. No GST oxide is added to the bottom interface for this nanostructure (i.e., between the bottom Au reflector and GST) since the deposition of GST on Au does not expose the GST at that interface to air. These GST oxide thicknesses are selected based on previous experience in working with GST-based MMs and comparing theory and experiments. We believe that with the smaller surface-to-volume ratio of the F-P structure, the oxidation effect is reduced compared to that in the Au-GST-Au nanostructure. For the sake of simplicity, the GST oxide layers are modeled as a non-dispersive lossless material with an assumed refractive index of 2.5 in this study. For the sake of simplicity, only plane-wave excitations to the

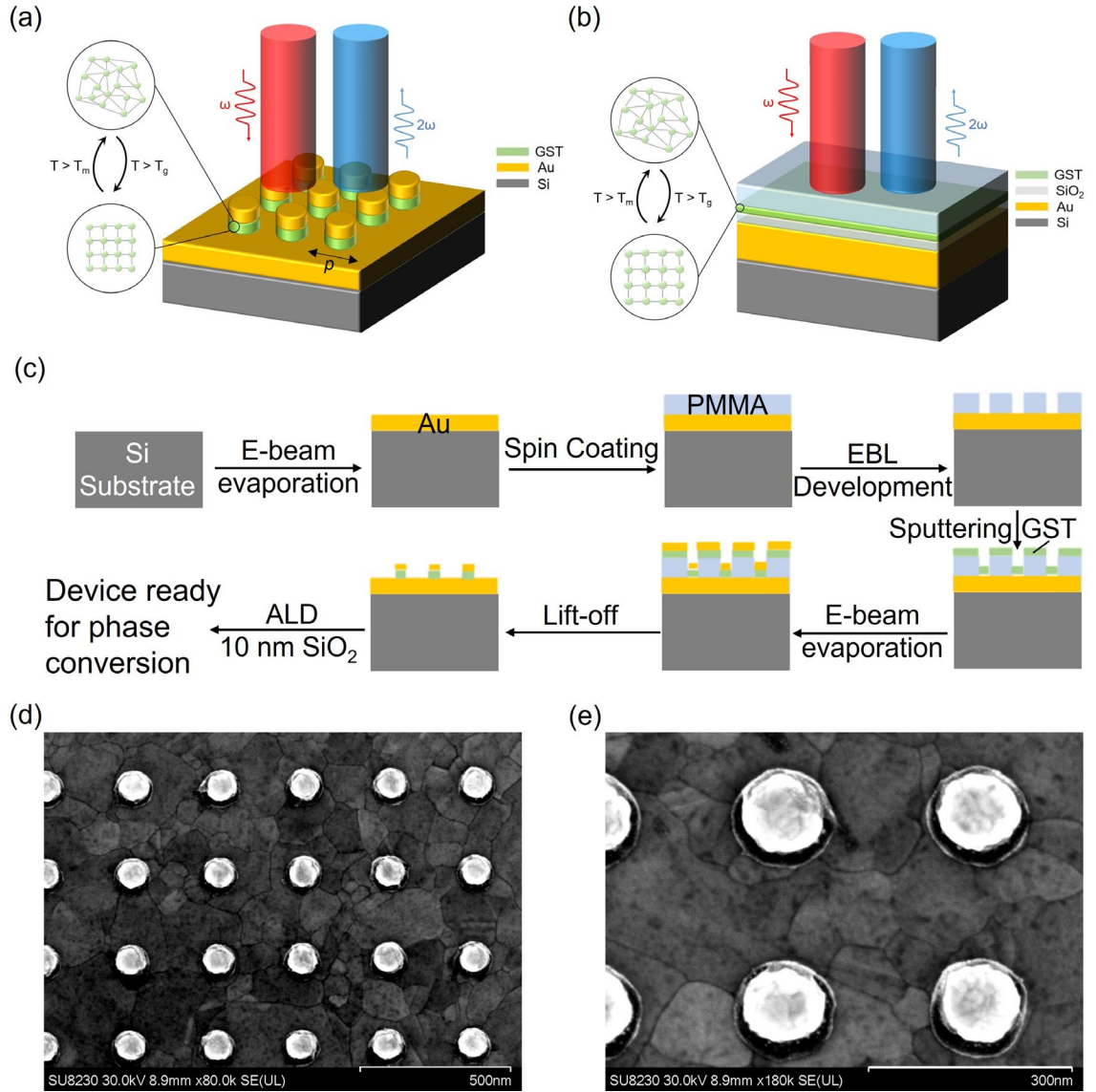


Figure 15 – (a) Schematic of the Au-GST-Au device composed of an array of Au (35-nm-thick) / GST (25-nm-thick) nano-disks on an Au reflector (100-nm-thick) and a Si substrate. The diameter of the nano-disk is selected as 120 nm, and the period of the MS is marked as p . (b) Schematic of the asymmetric F-P structure to be measured SHG and compared with the Au-GST-Au device. The Au reflector is also 100-nm thick, the bottom SiO₂ is 25-nm thick, the GST is 20-nm thick, and the top SiO₂ is 50-nm thick. (c) Fabrication process for the as-grown Au-GST-Au structure, in which e-beam evaporations of Au, spin coating of the e-beam resist, EBL, development of the resist, RF-sputtering of GST, lift-off, and ALD of an ultrathin SiO₂ protective layer were conducted. (d) A top-view SEM image of micron-scale area of an Au-GST-Au sample. (e) A top-view SEM image of submicron-scale area of another Au-GST-Au sample. All SEM images in this thesis are with a scaling measure marked.

structures with normal incidence from the air are studied as shown in Figure 15(a) and Figure 15(b).

We fabricated the as-grown Au-GST-Au structures by 1) e-beam evaporation of the Au reflector; 2) patterning of the e-beam lithography (EBL) resist poly (methyl methacrylate), in short PMMA; 3) RF magnetron sputtering of GST; 4) the e-beam evaporation of the top Au layer on a prime Si substrate, and lift-off. The samples were encapsulated by a ~ 10 nm-thick layer of SiO₂ deposited using atomic layer deposition (ALD) at ~ 100 °C (a safe temperature for SiO₂ deposition while preventing GST crystallization, which begins at T_g of $\sim 135^\circ\text{C}$ [42]) immediately after the lift-off process to protect GST from oxidation. The EBL process was conducted with an Elionix ELS-G100 system at IEN. The ALD process was conducted with the Cambridge NanoTech Plasma ALD at IEN. Figure 15(c) shows a flowchart of the fabrication process for the as-grown samples. Figure 15(d) and Figure 15(e) show top-view scanning electron microscopy (SEM) images of micron-scale and submicron-scale areas of an Au-GST-Au sample, respectively, with scaling marked. All SEM images in this thesis were taken with the Hitachi SU-8230 at IEN. The GST nano-disks exhibit radii slightly larger than the Au nano-disks due to the slight shadowing effect by the patterned PMMA during e-beam evaporation of the top Au layer. Only the extreme crystallinity GST states are considered for SHG from the asymmetric F-P cavity sample as the control structure for the Au-GST-Au samples.

3.2.3 Results and Discussion on the Structure

Simulated and measured linear reflectance spectra of the structure in Figure 15(a) with periods $p = 220$ nm, 250 nm, and 280 nm for the a-GST state are shown in Figure 16(a) and Figure 16(b), respectively. There is a general blue-shift of the measured resonances at different values of p compared to the simulation results, and the measured resonances cover a wider wavelength range compared to the simulated resonances. This is possibly due to fabrication imperfections including the error caused by shadowing effect indicated in Figure 15(e). The resonance blue-shifts with increasing p since the effective index of the structure (considering equivalent uniform layers) decreases, with no change in the Au/GST nano-disk dimensions. The absorption of the structure at resonance decreases with increasing p since the ratio of lossy Au/GST nano-disk area to the total MS area decreases. The structure at non-a-GST states is expected to exhibit a red-shifted resonance compared to the a-GST state since the refractive index of GST increases with crystallinity. Considering the range of resonances for different values of p , we selected Au-GST-Au

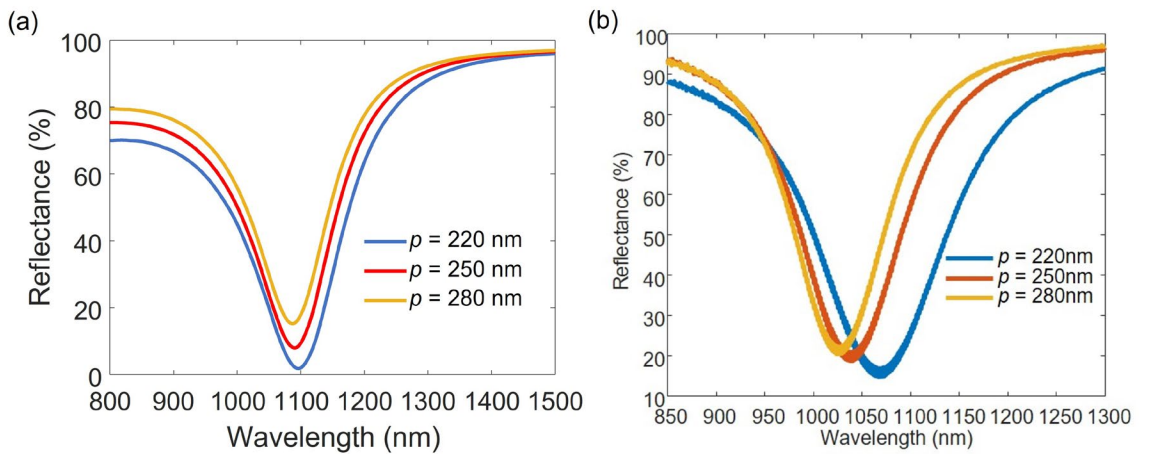


Figure 16 – (a) Simulated and (b) measured reflectance spectra for the structure in Figure 15(a) with cases of $p = 220$ nm, $p = 250$ nm, and $p = 280$ nm at the a-GST state.

MMs with $p = 220$ nm for SHG in the rest of our designs and experimental investigations. This is primarily due to the limitation in the characterization system that the OPO exhibits limited stability at excitation wavelengths < 1050 nm.

Simulated and measured linear reflectance spectra of the structure in Figure 15(a) with period $p = 220$ nm for all investigated GST states are shown in Figure 17(a) and Figure 17(b), respectively. There is a general blue-shift of the resonances at the investigated GST states compared to those of the simulations, and the measured resonances are closer to each other compared to the simulated resonances possibly due to fabrication imperfections. The gradually broadened reflection ‘dip’ is observed with increasing L due to the higher GST loss at higher values of L . Figure 17(c) shows the simulated linear reflectance spectra of the structure with parameters for Figure 17(a) at the visible wavelengths. There is a resonance ‘dip’ with significantly increased depth with GST crystallinity, starting from a depth of ~ 0 at the a-GST state, which indicates increased strength of the resonance. In addition, the resonance exhibits a much smaller redshift with increased GST crystallinity, compared to the designed resonance at the NIR. And the resonance wavelength is slightly longer than the SH at the NIR resonance, considering both simulated results in Figure 17(a) and measured results in Figure 17(b). Figure 17(d) presents measured reflected SHG intensity spectra of the device for the investigated GST states. One a.u. in Figure 17(d) is estimated to correspond to a SHG efficiency of $\sim 7 \times 10^{-12}$ at a pump power density of ~ 0.1 GW/cm². This a.u. applies to all SHG efficiencies in this section. As shown in the inset of Figure 17(d), the SHG peak intensity for the device at $L = 0\%$ (i.e., a-GST) is observed at the SHG emission wavelength of ~ 535 nm, which approximately matches the linear reflection ‘dip’ of λ_f (~ 1070 nm from Figure 17(b)). There is a SHG peak of smaller

intensity at ~ 575 nm possibly due to the resonant mode at the SH wavelength indicated in Figure 17(c) that can overcome the reduced signal at the λ_f . The SHG peak intensities of the device for $L = 50\%$ and $L = 100\%$ are ~ 50 and ~ 100 times higher than that for $L = 0\%$, respectively, although the Q of linear resonance is reduced with GST crystallization. This clearly indicates that the second-order nonlinearity of c-GST is much stronger than the surface second-order nonlinearity of Au in this device. Note that the SHG peaks at ~ 575 nm for the non-a-GST states (see the yellow and red curves in Figure 17(d)) are higher

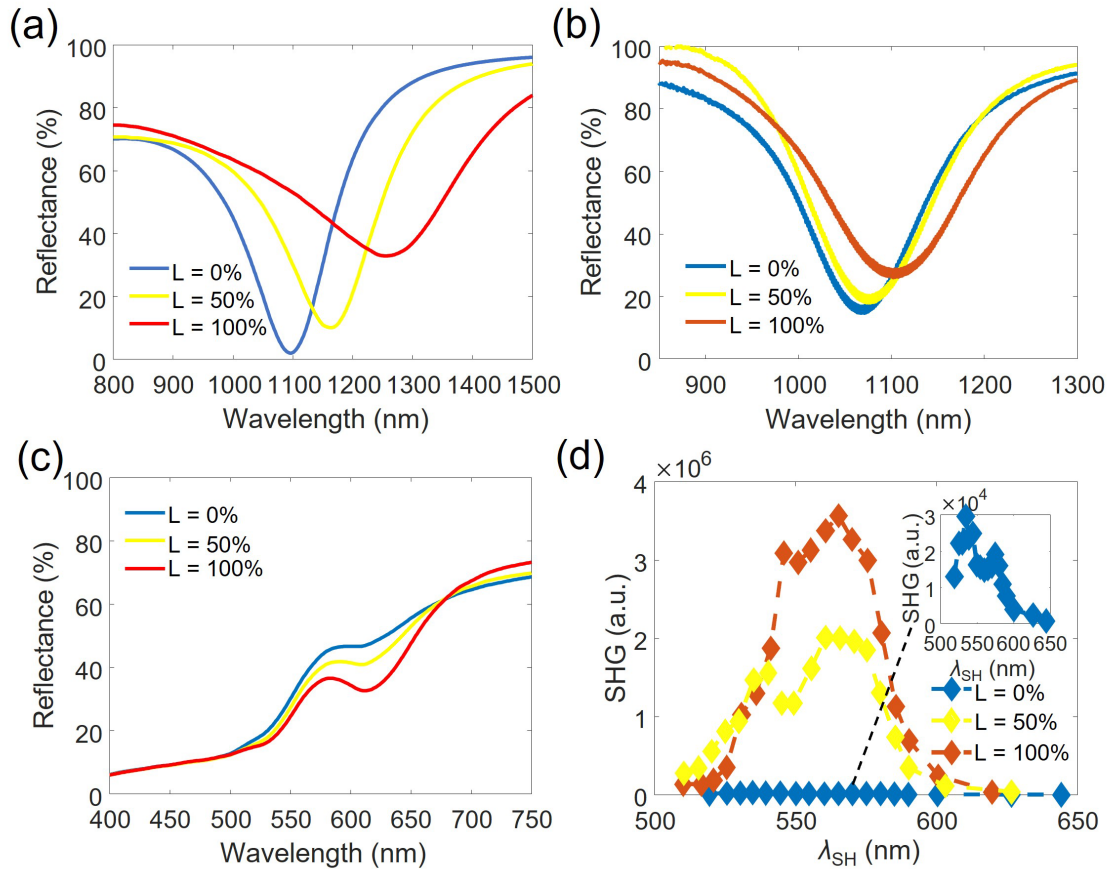


Figure 17 – (a) Simulated and (b) measured reflectance spectra for the structure in Figure 15(a) with $p = 220$ nm at investigated GST states. (c) Simulated reflectance spectra of the structure with parameters for Figure 17(a) at the visible wavelengths. (d) Measured SHG response of the correspondent fabricated samples, where λ_{SH} represents the SH wavelength, and the inset shows a zoomed-in view of the weak SHG signal for the a-GST case.

than the peaks corresponding to the linear resonances, which indicates that the hybridization of the linear mode with the SH resonant mode becomes stronger than the peak of the non-hybridized linear mode with GST crystallization. The observation is in accordance with the strengthened resonance around SH wavelengths, which is indicated in Figure 17(c). This device, to the best of our knowledge, exhibits the largest extinction ratio of SHG switching for a NL MM reported to date. In addition, by using different values of L (different levels of GST crystallinity), both the amplitude and the wavelength of the maximum SH signal can be modified. We attribute this to the strong tunability of the GST nonlinearity with its change of crystallinity (L). This makes the device an unmatched solution for other applications of MMs for second-order optical nonlinearity.

Using the observations for the SHG in the structure in Figure 15(a), we found the asymmetric F-P GST device of certain dimensions in Figure 15(b) experimentally matching the SHG resonance wavelength from the F-P device to that from the Au-GST-Au MM at the c-GST state (to achieve substantial second-order nonlinearity). The measured linear reflectance spectrum of the F-P structure in Figure 15(b) for the c-GST state is shown in Figure 18(a). The reflectance band is much broader than that of the Au-c-GST-Au patterned structure. This is due to the fact that the absorption resonance of a loss mechanism [140] is much weaker than the gap-surface-plasmon resonance with high field confinement. Figure 18(b) shows a comparison plot of measured SHG spectra at the c-GST state of the selected structure in Figure 15(a) with $p = 220$ nm and the structure in Figure 15(b). As shown in the inset of Figure 18(b), the SHG peak intensity for the F-P device with the c-GST state is observed at the SH emission wavelength of ~ 575 nm, which approximately matches the shallow reflection ‘dip’ (~ 1150 nm) at the λ_f in Figure 18(a).

The SHG resonance wavelength of the Au-c-GST-Au patterned structure is approximately the same as that of the F-P c-GST structure. However, it is clear from Figure 18(b) that the SHG output intensity of the Au-c-GST-Au patterned structure is ~ 100 times that of the F-P c-GST structure given that their GST thicknesses are similar. This is additional evidence for the strength of the gap-surface-plasmon resonance, which can mitigate the relatively high loss of GST, especially for its most lossy (i.e., crystalline) state. Figure 18(c) shows measured reflected NL emission intensity spectra, at the visible wavelengths, of the asymmetric F-P structure in Figure 15(b) for the a-GST and c-GST states at the pump wavelength of 1150 nm. The output SHG peak intensity of the F-P structure for the c-GST state is measured to be ~ 50 that of the a-GST case, showing the possibility of ON/OFF switching of the SH signal. This modulation depth is lower than that of the Au-GST-Au structure (~ 100), which might be due to greater susceptibility of the relatively weak SHG signal to the background noise for the F-P structure. As shown in the inset of Figure 18(c), a heavy tail of the SHG emission spectrum at the a-GST state (extending to longer spectral

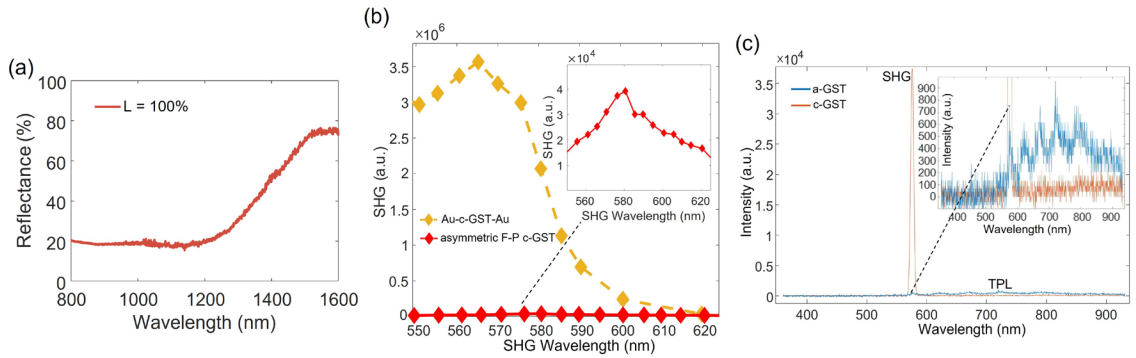


Figure 18 – Measured (a) linear reflectance spectrum for the structure in Figure 15(b) at the c-GST state ($L = 100\%$); (b) c-GST state SHG spectra of the structure in Figure 15(a) with $p = 220$ nm, and the structure in Figure 15(b); (c) reflected NL emission intensity spectra, at the visible wavelengths, of the asymmetric F-P structure for the a-GST and c-GST states at a pump wavelength of 1150 nm. TPL: two-photon luminescence.

wavelengths than the SHG emission) represents the two-photon luminescence (TPL) following the TPA process, which is a NL optical process related to the imaginary part of the $\chi^{(3)}$ s of NL materials [83]. It is evident that the TPL at the c-GST phase of the F-P structure is generally weaker than that observed at the a-GST phase, though the imaginary part of $\chi^{(3)}_{\text{c-GST}}$ is generally larger than that of $\chi^{(3)}_{\text{a-GST}}$ at the NIR wavelengths according to the empirical Miller's rule, i.e., $\chi^{(3)} \propto (\chi^{(1)})^4$ [90]. The weaker TPL of the c-GST structure can be due to a smaller linear nearfield and larger absorption of the intrinsic TPL signal in the more lossy c-GST state.

To better illustrate the sharp difference between SHG from the Au-c-GST-Au gap-surface-plasmon resonance and asymmetric F-P c-GST absorption resonance, we show in Figure 19(a) and Figure 19(b) the middle cross-sectional plots of simulated normalized nearfields in a plane parallel to the polarization direction in Figure 15(a) and Figure 15(b), respectively, at the c-GST state at $\lambda_f = 1260$ nm. This corresponds to the simulated gap-surface-plasmon resonance of the structure in Figure 15(a) and approximates the simulated absorption resonance of the structure in Figure 15(b). From Figure 19, we can observe that although the largest nearfield enhancement in the Au-c-GST-Au structure lies in the GST oxide between the lossy GST and the top Au layer (i.e., top GST-oxide layer, see Figure 19(a)), the nearfield enhancement in c-GST in Figure 19(a) is still substantially larger than that in Figure 19(b). Note that due to the large resonance nearfield on the Au/dielectric interfaces (as clearly seen from Figure 19(a)), the surface $\chi^{(2)}$ of Au cannot be ignored as a component in the SHG sources of the Au-c-GST-Au structure. Thus, both surface $\chi^{(2)}$ of Au and bulk $\chi^{(2)}$ of c-GST coupling to the strong linear field interference contribute significantly to the largely enhanced SHG from the patterned Au-c-GST-Au structure

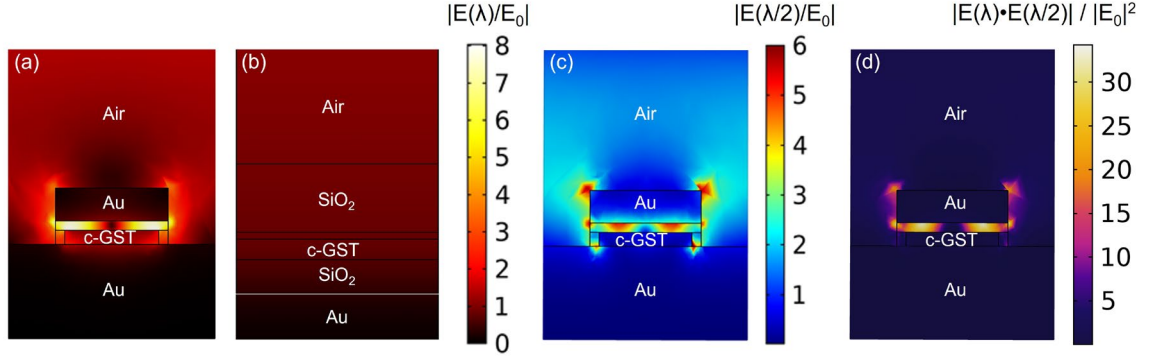


Figure 19 – Middle cross-sectional plots of simulated normalized nearfields in a plane parallel to the polarization direction (i.e., the incident polarization is in the plane of this figure) in (a) Figure 15(a) and (b) Figure 15(b) for the c-GST state at $\lambda = 1260$ nm. The fields are normalized to the incident field. Figure 19(a) and Figure 19(b) are in the same scale, and the maximum value of the scale bar is set to the maximum normalized nearfield in the Au-c-GST-Au structure at $\lambda = 1260$ nm. Figure 19(c) shows the normalized nearfield plot for the incidence wavelength of $\lambda/2$ (i.e., SH wavelength) under the same way of excitation. The mode overlap between nearfields in Figure 19(a) and Figure 19(c) is plotted in Figure 19(d) in terms of normalized inner-product of the nearfields to the square of incident field. Solid lines show the extent of all materials. All material components of the structures are marked in the plot except for the GST oxide, which is represented by unmarked areas (on top of the c-GST layer) in the plots.

compared to the asymmetric F-P c-GST cavity structure. In addition, we studied the simulated nearfield at incidence of the correspondent SH wavelength (i.e., 630 nm), and the mode overlap of the nearfields at the fundamental and SH wavelength incidences. Figure 19(c) shows the normalized nearfield plot for the SH wavelength incidence. The mode overlap between nearfields in Figure 19(a) and Figure 19(c) is plotted in Figure 19(d) in terms of normalized inner-product of the nearfields to the square of incident field. It is clear in Figure 19(c) that the largest nearfield enhancement in the Au-c-GST-Au structure also lies in the top GST oxide layer, except for some hotspots on interfacial corners on the Au/c-GST nano-disk. Figure 19(d) shows a large mode overlap in the top GST oxide layer as well. Therefore, surface $\chi^{(2)}$ of c-GST, which can couple efficiently with the mode overlap, might also be much larger than that of a-GST. The contributions of bulk $\chi^{(2)}$ of c-

GST, and surface $\chi^{(2)}$ s of Au and GST of different crystallinities to the SHG outputs in this structure are worth further studying.

3.2.4 *The Characterization Setups and SHG-Excitation Power Dependence*

The linear reflectance spectra were normalized with the reflected power of control areas of 100-nm-thick Au on the substrates for the samples. The SHG characterizations were conducted with the same Si charge-coupled device ($\sim 400\text{--}700$ nm in detection range) used in Section 2.4. A $100\times$ objective lens ($\text{NA} = 0.95$) was used for effective collection of SHG signals under the formation of out-of-plane resonant electric dipole components [179]. These characterization settings were applied to all the samples for Figure 15(a) and Figure 15(b). Figure 20 shows detailed setup schematics including the optical paths of the SHG characterization. A 750-nm SPF and a 700-nm SPF are used sequentially before SHG detection due to that their individual attenuations at the NIR wavelengths are smaller than that of the 532-nm SPF in Figure 10.

Figure 21 presents excitation power dependence of the measured SHG intensity from the a-GST from the sample of the structure in Figure 15(a) with $p = 220$ nm and the excitation $\lambda_f = 1080$ nm. The excitation power dependence for the samples of the structure in Figure 15(b) is not tested. This is because of a higher laser damage threshold expected for the F-P cavity than the MIM structure that contains plasmonic nanoparticles. The fact is supported by that the excitation power level in Figure 11 ($\sim 10^0$ mW) is higher than that in Figure 21 ($\sim 10^{-1}$ mW). The demonstrations of these structures use the excitation power of ~ 0.1 mW (the peak pump intensity of ~ 0.1 GW/cm²), which fits in the quasi-linear regime shown in Figure 21 and should be free from GST phase conversion (change of n_0

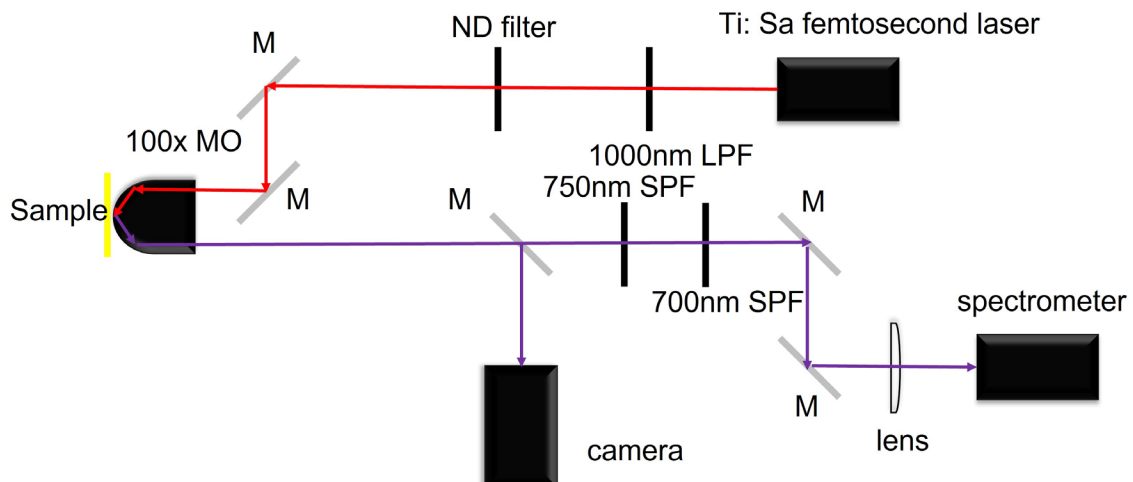


Figure 20 – The setup schematic for the SHG measurement of the Au-GST-Au and F-P GST devices, where ND, ‘M’, ‘100× MO’, LPF, and SPF represent neutral density, a mirror, the 10× microscopic objective lens, a long-pass filter, and a short-pass filter, respectively.

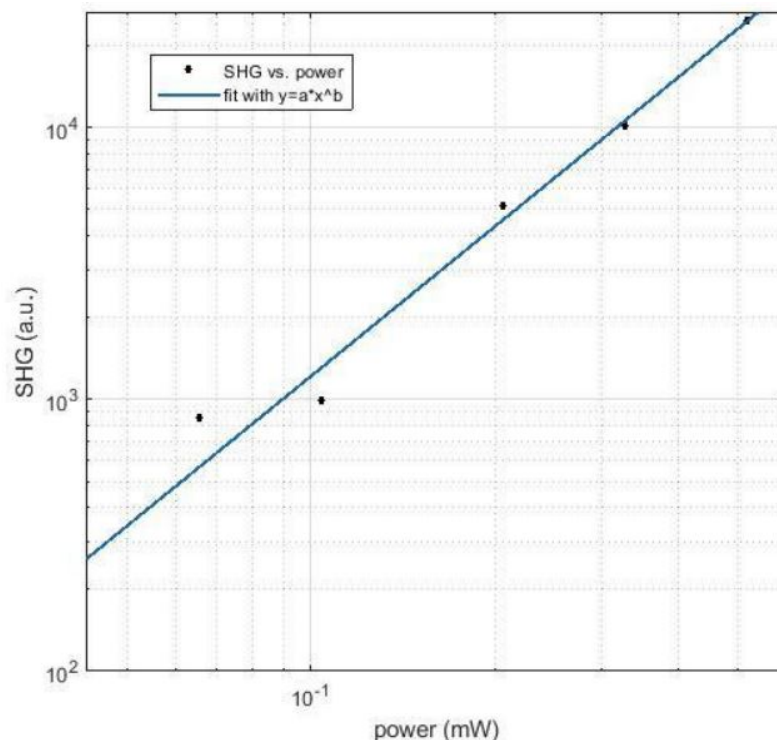


Figure 21 – Excitation power (i.e., pump power) dependence of the measured SHG intensity from the sample of the structure in Figure 15(a) with $p = 220$ nm and the excitation $\lambda_f = 1080$ nm. A power-law fit is applied to the measured data. The slope of the fit (b) is 1.83 ± 0.24 , in acceptable agreement with the expected slope of 2 for SHG. The excitation power was measured immediately after the ‘100× MO’ in Figure 20 without the sample.

and $\chi^{(2)}$) upon laser annealing. The slope is most likely only slightly below the expected slope of 2 for SHG (1.83 ± 0.24), which indicates that the SHG is possibly accompanied by substantial NL absorption [180].

3.2.5 *Conclusion and Outlook*

We experimentally demonstrated a new device based on a MIM structure for efficient tunable SHG by integrating conveniently reconfigurable PCM GST with a plasmonic MS. The performance of the structure is compared to SHG from one of the samples of the counterpart asymmetric F-P GST cavity structure that has been studied for THG in Section 2.3. Both structures are in subwavelength scale and exhibit SHG switching with ON/OFF ratios of $\sim 10^2$. The Au-GST-Au structure exhibits a much higher average SHG efficiency than the F-P GST structure among investigated GST crystallinity states. This is caused by the fact that the MIM structure exhibits a gap-surface plasmon resonance with a stronger photonic interaction than the absorption resonance in the F-P structure. This study expands the linear optical intensity switching nanodevices to the SH paradigm and paves the way for more sophisticated designs for improved efficiency and functionality, which might be applicable to SHG microscopy, communication, and computing. These structures can be combined with ultrafast and compact heating processes using ITO Joule micro-heaters as suggested in Section 2.5 which is for the device in Figure 2(a) of Section 2.2. Robust metals (e.g., tungsten (W), demonstrated in Ref. [158]) can also be incorporated as micro-heaters to expand the device with new features for ultrafast and compact tunable microelectronic chip-scale SHG devices. The Au-GST-Au structure can also be a reliable platform for SHG switching with higher conversion efficiencies by 1) shifting the operation frequency to a regime of very low GST optical loss as elicited in

Section 2.5, or 2) by using phase-change chalcogenides of more significant inversion asymmetry in ordered crystalline structures, such as KPSe_6 [181] and $\text{K}_4\text{GeP}_4\text{Se}_{12}$ [182].

CHAPTER 4. DYNAMICALLY TUNABLE THG WITH A GST-MODULATED A-SI MS

This chapter summarizes a numerical demonstration of 1) switchable THG of a giant modulation depth as high as ~ 70 dB at the optical communication conventional band (C-band, 1530–1565 nm) for fundamental wavelengths (Section 4.2), and 2) an experimental demonstration of efficient switchable THG of a modulation depth as high as ~ 20 dB at the fundamental wavelength of 1600 nm (Section 4.3). The demonstrations are based on a dielectric MS supporting a Fano-type resonance, electromagnetically-induced transparency (EIT), that is actively controlled by a quarter-wave asymmetric F-P cavity incorporating multiple crystallinity percentage states of GST. This shows the high potential of GST-based fast dynamic THG switches for real-world applications ranging from communications to computing. Section 4.2 is assembled from Ref. [176] and Section 4.3 is revised from the presentation of Ref. [183], both published by the author.

4.1 Introduction to All-Si THG MSs

Si, with a high refractive index reaching 3.7 amorphous and polycrystalline states [101], a small optical loss ($E_g \sim 1.12$ eV at the room temperature), a large $\chi^{(3)}$, and compatibility with CMOS fabrication processes, is widely researched for THG in MSs. Yang *et al.* experimentally demonstrated a high-Q polycrystalline Si (poly-Si) MS (linear $Q \sim 300$) with a simulated maximum linear nearfield enhancement of ~ 50 to obtain high THG efficiency of 1.2×10^{-6} using an OPO with a repetition rate of 80 MHz, a pulse duration of ~ 250 fs, and a peak intensity of ~ 3.2 GW/cm², which fairly surpasses other

demonstrations [101]. They also demonstrated a resonant THG intensity $\sim 10^5$ times that off-resonance, which is levels higher than that obtained using the GSST THG MS in Ref. [88]. They utilized an EIT-type Fano resonance for dielectric bright-dark mode conceived from plasmonic EIT structures. Recently, Koshelev *et al.* investigated BIC to further enhance the linear Q for boosting THG efficiency [184]. Details on BIC MSs will be discussed in Section 6.1. Liu *et al.* designed a high-Q symmetry-broken 500-nm-thick Si MS governed by quasi-BIC to achieve an ultra-high Q of $\sim 2 \times 10^4$ and a record-breaking THG conversion efficiency of $1.4 \times 10^{-8} [\text{W}^{-2}]$ with a pulsed laser with a repetition rate of 80 MHz, a pulse duration of ~ 5 ps, and a peak power of ~ 3 mW [26]. Yang *et al.* observed up to 5×10^7 increase in THG from an a-Si MS of nanopillars coupled to a gold reflector, compared to the unpatterned film, and a record high THG efficiency of 1.8×10^{-6} at a relatively low peak pump intensity of 0.4 GW/cm^2 for fs-scale excitation [185]. Nevertheless, the maximum reported THG efficiency in a-Si MSs is still limited to the order of 10^{-6} , which is possibly due to fabrication imperfections as a partial reason.

In this chapter, we leverage an a-Si MS structure consisting of coupled bright-mode nano-bars and dark-mode nano-disks hybridized with a reflective quarter-wave F-P GST cavity to realize a THG switch. The large refractive index change between the a-GST and c-GST induces a significant phase difference in the linear beam reflected from the MS. This enables the realization of constructive/destructive interference between the normal incident beam and the reflected beam at the two extreme states of GST. Reflected THG intensity can exhibit a large modulation depth according to $\mathbf{P}(3\omega) = \epsilon_0 \chi^{(3)} \mathbf{E}(\omega) \cdot \mathbf{E}(\omega) \cdot \mathbf{E}(\omega)$. This cubic relationship between $\mathbf{P}(3\omega)$ and $\mathbf{E}(\omega)$ results in a much larger THG

nearfield amplitude difference between constructive and destructive interferences than that for the linear nearfield.

4.2 Numerical Study of Tunable THG with a GST-Modulated a-Si MS

4.2.1 Design and Simulations of the GST-Modulated NL MS

The device is comprised of 5 layers aiming to work at the λ_f of 1550 nm wavelength. A 100-nm-thick Au layer is first deposited on a Si substrate as a back-reflector. Then, a three-layer sandwich structure of SiO₂-GST-SiO₂ is formed on top of it. Lastly, the a-Si MS could be fabricated through EBL and dry etching. The thickness of the GST layer is 50 nm. The thickness of the bottom SiO₂ layer is 10 nm to avoid the diffusion of Au into GST during annealing. The thickness of the top SiO₂ layer is 450 nm to generate constructive interference at its top surface for a-GST. This layer can be also deemed sufficiently thick to avoid lowering the Q by the GST loss. The thickness of the a-Si layer (T_{a-Si}) is 150 nm. The planar dimensions of the meta-atoms are shown in Figure 22, which illustrates the device schematic without showing the heating structure. The MS structure is selected based on previous reports to ensure the formation of an EIT mode [101]. To simplify the simulations, the MS is excited from the top (air) with a plane wave polarized along the long axis of the a-Si nano-bars (i.e., the y-axis in Figure 22). Incident angles from -10° to 10° with 1° increments are considered for both in-plane and out-of-plane directions. The absorption losses of all materials at the corresponding wavelengths have been carefully considered in all simulations.

Similar to Section 3.1.1, crystallinity percentages $L = 0\%$, 20% , 40% , 60% , 80% , and 100% of GST are simulated in this study. The extinction coefficients of a-GST and c-



Figure 22 – Schematic of the reconfigurable NL MS; the device structure includes (on top of a Si handle layer) successive layers of 100-nm-thick Au, 10-nm-thick bottom buffer SiO₂, 50-nm-thick GST, 450-nm-thick top SiO₂, and a-Si with thickness $T_{a-Si} = 150$ nm. The dimensions of the a-Si MS are $p_1 = p_2 = 910$ nm, $a = 240$ nm, $b = 850$ nm, $g_1 = 75$ nm, and $g_2 = 85$ nm. T_g and T_m are the glass and melting temperatures of GST.

GST at the fundamental wavelength of interest (i.e., 1550 nm) are small (~ 0.005 and ~ 0.89 , respectively), comparable to those in Ref. [186]. In addition, the Au layer and the Si substrate work as efficient heatsinks to prevent the crystallization of a-GST and melting of c-GST during optical measurements. We numerically simulated the opto-thermal response of the structure with a-GST and c-GST states under 250-fs-long laser pulses with a repetition rate of 80 MHz and a peak intensity of 3.2 GW/cm^2 as used in Ref. [101]. The local temperature has been found not being able to exceed 38°C even for the more absorptive c-GST structure during the annealing by the pulse. Such a temperature is far lower than that needed for changing the crystallinity state of GST. $\chi^{(3)}$ of a-Si is assumed to be $1.4 \times 10^{-18} \text{ m}^2/\text{V}^2$ in account of empirical Miller's rule that $\chi^{(3)} \propto (\chi^{(1)})^4$ for lossless materials, and the refractive index of our sample of uniform sub-micron-thick a-Si film is

measured to be ~ 3.42 at the wavelength of 1550 nm. Here we use the experimentally calculated value of $\chi^{(1)}$ for our deposited a-Si. $\chi^{(3)}$ of GST is also considered in the simulations as its effect can be comparable to that of a-Si, and the optical field is not limited to the interface.

The a-Si MS dimensions are designed by simulating the EIT MS on only a thick-enough layer of SiO₂ under normal incidence with $\lambda_f \sim 1550$ nm (the exact resonance wavelength for the MS is 1552.5 nm) as shown in the linear transmission spectrum in Figure 23(a). Figure 23(b) shows the linear nearfield enhancement plot for the MS on SiO₂ at the middle-z-plane of the MS ($T_{\text{a-Si}}/2$ distance above the interface between the SiO₂ layer and the MS in air) under normal incidence with $\lambda_f = 1552.5$ nm. A large maximum linear nearfield enhancement similar to that in the MS of Ref. [101] is exhibited at the dark-mode nano-disk, as the electric dipoles of the bright-mode nano-bar feed electromagnetic energy to the magnetic dipoles of the dark-mode nano-disk at resonance [23]. Figure 23(c) shows

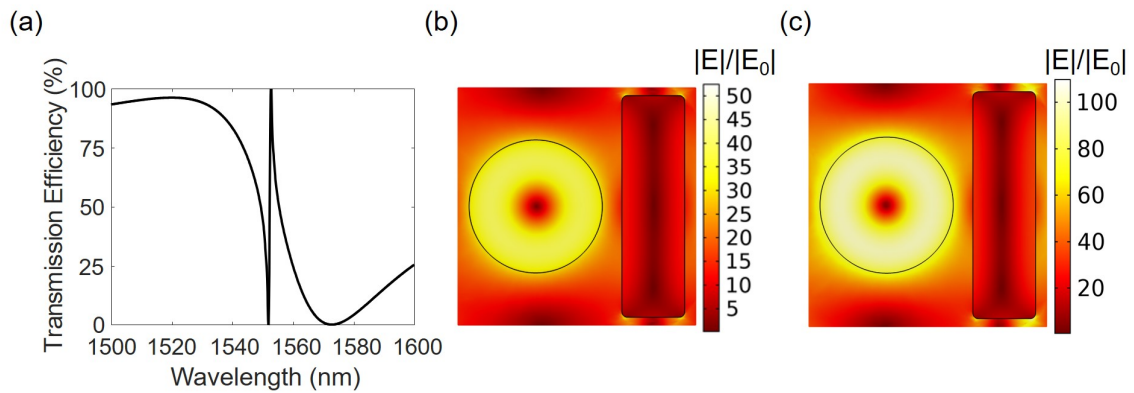


Figure 23 – (a) The linear transmission efficiency plot, and (b) simulated middle-z-plane nearfield plot at $\lambda_f = 1552.5$ nm of the a-Si MS on infinitely thick SiO₂ at plane-wave normal incidence from air exhibiting EIT. The nearfields are normalized to the incident field (E_0), geometric dimensions of the MS are the same as those in the captions of Figure 22. (c) Simulated normalized middle-z-plane nearfield plots for the same MS on top of a 570-nm-thick SiO₂ on the same Au reflector as in Figure 22 at $\lambda_f = 1550$ nm.

the linear nearfield enhancement plot at the middle-z-plane of the same a-Si MS on an optimized SiO₂ layer of 570-nm-thick on the same Au reflector as in Figure 22(a) that resulted in \sim doubling the maximum linear nearfield compared to that in Figure 23(b). This indicates almost perfect constructive interference between incident and reflected light at the MS in this control structure.

The thickness of the GST layer in Figure 22 is selected to ensure $\sim 180^\circ$ phase difference for the reflected beam out of the structure between the two cases of a-GST and c-GST. The thickness of the top SiO₂ layer in Figure 22 is selected to result in constructive interference at the pump wavelength between the incident and the reflected beams around the middle-z-plane of the a-Si MS for the structure at the a-GST state. Combining these two design criteria also ensures destructive interference between the incident and reflected beams at the pump wavelength around the middle-z-plane of the a-Si MS for the c-GST case. This is clearly seen in Figure 24(a) and Figure 24(b), which show the linear nearfield enhancement plots at the middle-z-plane of the MS under normal incidence with $\lambda_f = 1550$ nm for the structure in Figure 22 with a-GST and c-GST states, respectively. The maximum linear nearfield enhancement of ~ 70 in Figure 24(a) is substantially larger than that in Figure 24(b) (~ 50) but smaller than that in Figure 23(c) (~ 100). These results indicate imperfect constructive interference of the incident and reflected beams in the MS for the structure in Figure 22 with the a-GST state, due to the loss of a-GST. Figure 24(c) and Figure 24(d) show the linear nearfield plots of the designed F-P cavity without the MS for a-GST and c-GST, respectively. It is clear that the interference patterns at the two states are approximately out of phase. These results clearly show that the use of the F-P structure mitigates to some degree the loss of the GST layer and provides a reasonably large nearfield

enhancement while enabling the large tuning range. The large difference between the maximum nearfields in Figure 24(a) and Figure 24(b) stems from the large refractive index contrast of a-GST and c-GST, which considerably modifies the resonance of the overall structures (including the F-P cavity and the meta-atoms). The results in Figure 24(b) also show that our design mitigates the problem of high loss in the c-GST state by assigning the off state of switching to this state.

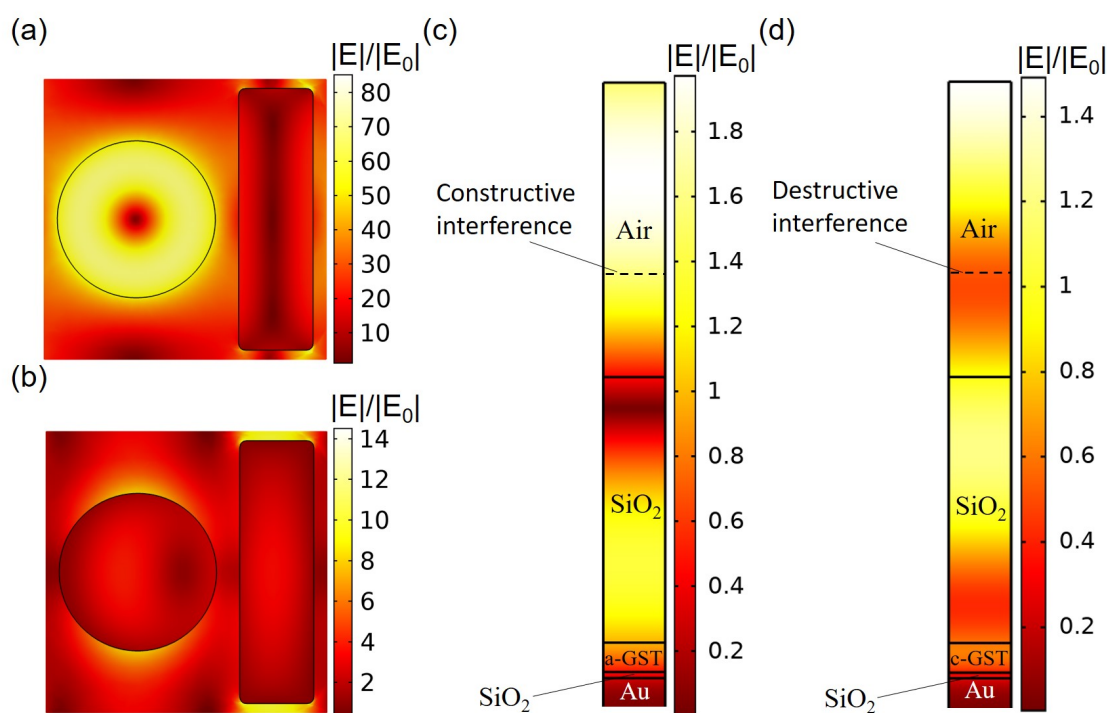


Figure 24 – Simulated normalized nearfield at the middle-z-plane of the MS for the structure in Figure 22 with (a) a-GST and (b) c-GST states. Simulated normalized nearfield plots of asymmetric (c) a-GST and (d) c-GST F-P cavity of $T_{\text{GST}} = 50$ nm sandwiched between two SiO₂ layers with thicknesses $T_{\text{to}} = 450$ nm and $T_{\text{bo}} = 10$ nm without the a-Si MS. Solid lines show the extent of all materials. The example planes of interference observations are marked with dashed lines. All plots are for plane-wave normal incidence at $\lambda_f = 1550$ nm. The large difference between the field enhancements in (a) and (b) is due to the constructive and destructive interference between the incident and reflected beams at ~ 200 nm above the top SiO₂ layer as seen in (c) and (d) for the a-GST and c-GST case, respectively.

4.2.2 Results and Discussion on the Numerical Design

Figure 25(a) further demonstrates the role of GST crystallinity level (L) by showing the linear reflection responses of the structure in Figure 22 for different values of L . It is clear that the changes in the index of refraction and the loss due to varying L have a profound effect on the reflectance amplitude and its rate of variation with wavelength. The resonances near 1550 nm are gradually red-shifted with increased L due to the refractive index increase before vanishing (and becoming off-resonance) at $L = 80\%$. In addition, the increase in the optical loss of GST by increasing L affects the sharpness of the reflection dips. Note that the overall linear reflection response is the result of the interference pattern at the a-Si layer and the resonance lineshape in Figure 23(a). Thus, the overall linear reflection response is not just a simple function of the refractive index and the optical loss of GST. This explains why the reflectance of the structure with $L = 100\%$ in Fig. 4(a) is larger than that for the structure with $L = 80\%$. Figure 25(b) shows the THG efficiency of the structure in Figure 22 at different values of L in terms of the vertical component of the reflected THG power flow at 3.2 GW/cm^2 pump intensity calculated by the formalism in Ref. [101]. Figure 22(b) shows multi-level switching with an ultra-large modulation depth of $\sim 70 \text{ dB}$ around $\lambda_f = 1550 \text{ nm}$, which is a solid result of the large tunability of the refractive index of GST over multiple states. It can be observed from Figure 22(b) that the structures with larger L provide the red-shifting of the TH signal while exhibiting some smoothening of the THG peak due to the added optical loss. This functionality vanishes at larger values of L (e.g., $L > 80\%$) as such structures become off-resonance with a considerable optical loss.

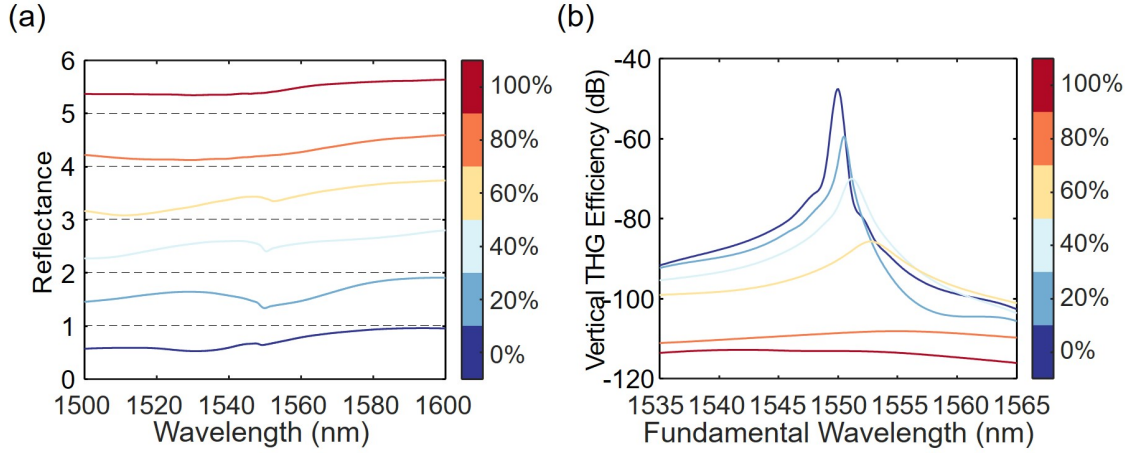


Figure 25 – Simulated (a) linear reflectance spectra and (b) vertical-component THG efficiency plots for fundamental C-band for the 6 GST crystallinity percentages (L). THG efficiencies of this device are calculated in comparison to the simulation result in Ref. [101].

The key advantages of the structure in Figure 22 are: 1) a potentially tunable THG source with a reasonably large tuning bandwidth (e.g., 5 nm for the pump wavelength, see Figure 25(b)); 2) a potentially large switching extinction ratio (e.g., 70 dB, see Figure 25(b)); 3) a highly miniaturized integrated structure (see Figure 22) with full CMOS fabrication compatibility. The loss of GST can be addressed by using alternative PCMs. The structure in Figure 22 with GST can contribute to more efficient THG responses than that of the a-Si MS in the longer infrared wavelengths where its optical loss is minimal. However, less lossy PCMs such as GSST have the potential for all-PCM MSs to realize giant THG switching with the low-loss amorphous state forming the high-Q resonance.

4.3 Experimental Study of Tunable THG with a GST-Modulated a-Si MS

4.3.1 Fabrication and Characterizations of the Device

The as-grown samples on crystalline Si (c-Si) substrates for structure in Figure 22 were fabricated by consequent e-beam evaporation of Au, low-temperature ($\sim 100^\circ\text{C}$)

plasma-enhanced chemical vapor deposition (PECVD) of SiO₂, sputtering of GST, ALD (~ 100°C) of 20-nm-thick SiO₂ adhesive layer, PECVD (~ 100°C) of top SiO₂ and a-Si, and EBL patterning of the a-Si MS. The low-temperature depositions are for low-stress and adhesive films as well as the prevention of GST phase transition. The a-Si deposition is done by the Unaxis PECVD tool at the IEN. A flowchart of the fabrication process, including hydrogen silsesquioxane (HSQ) e-beam resist development and inductively coupled plasma (ICP) etching, for the as-grown samples is shown in Figure 26. The 20-nm-thick ALD SiO₂ layer also covers the edge of the GST layer to protect GST from being eroded by resist development solution. The details of resist development and etching for a-Si MSs are in Section 6.2.2. The left-over HSQ on the a-Si meta-atoms is not removed at the end for both simplicity and impedance matching of the top HSQ/a-Si and bottom a-Si/SiO₂ interfaces at the MS. This is according to the fact that the chemical compositions of them are very similar, therefore low-index and lossless characteristics of HSQ is very similar to SiO₂. The coupling among the meta-atoms is mostly in the plane of the MS, therefore, is not affected by the left-over HSQ. A top-view SEM image of a sample showing a few unit cells of the MS is displayed in Figure 27. HSQ residuals are observable

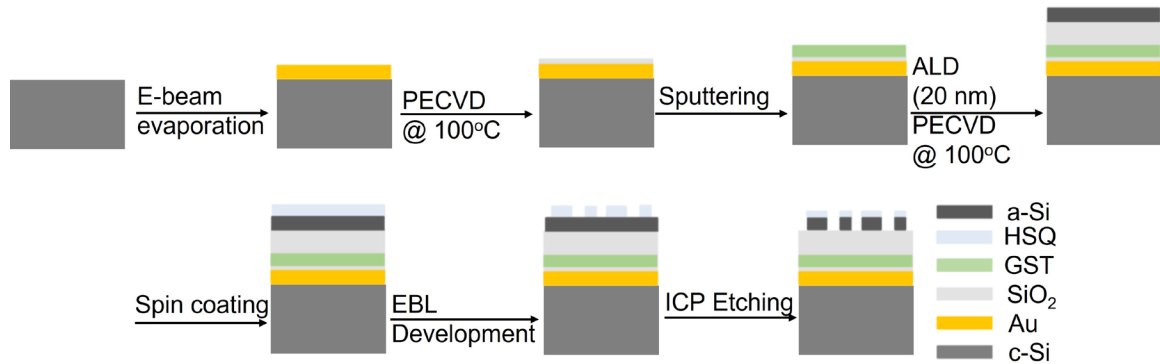


Figure 26 – Fabrication process for the as-grown structure in Figure 22, in which e-beam evaporations, PECVDs, RF-sputtering, ALD, spin coating of the e-beam resist, EBL and resist development, and ICP etching were conducted.

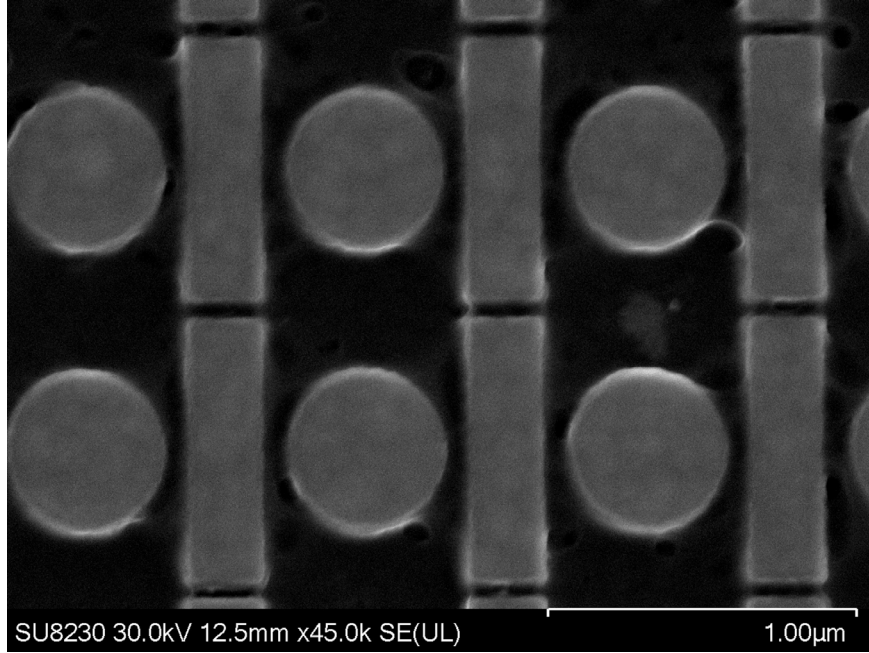


Figure 27 – A top-view SEM image of a few unit cells of an a-Si MS in a sample for the structure in Figure 22.

at the edges of the a-Si nanoparticles in Figure 27. For the nano-bars, the residuals tend to be more obvious near the vertices. This can be due to the deformation of HSQ residuals, which can worsen fabrication imperfection.

Linear reflectance spectra were measured to identify the resonance wavelengths of the samples that are susceptible to fabrication imperfections and select the one with the highest quality for THG characterization. The reflectance spectra were normalized with the reflected power of a thick Au sample, due to that control areas of simply 100 nm-thick Au on the substrate for the sample in Figure 27 are difficult to justify. The THG characterization setup is the same as that in Figure 10 of Section 2.4. THG-excitation power dependence was not measured due to that the structure in Figure 22 has a higher expected damage threshold than that in Figure 15(a) of Section 3.2.2. The expectation is based on

that dielectric and plasmonic MSs are incorporated in the structures in Figure 22 and Figure 15(a), respectively.

4.3.2 Results and Discussion

Resonance of the sample in Figure 27 exhibits substantial red-shift probably due to fabrication imperfections. Thus, we measured the NL emission spectra of the sample of different GST crystallinities at visible wavelengths for the THG signal under an excitation $\lambda_f = 1600$ nm that is at the long wavelength end of the effective range of the OPO. Figure 28 shows the measured NL emission intensity spectra of the sample for the a-GST, semi-c-GST, and c-GST states at a pump power comparable to that for Figure 4(d) in Section

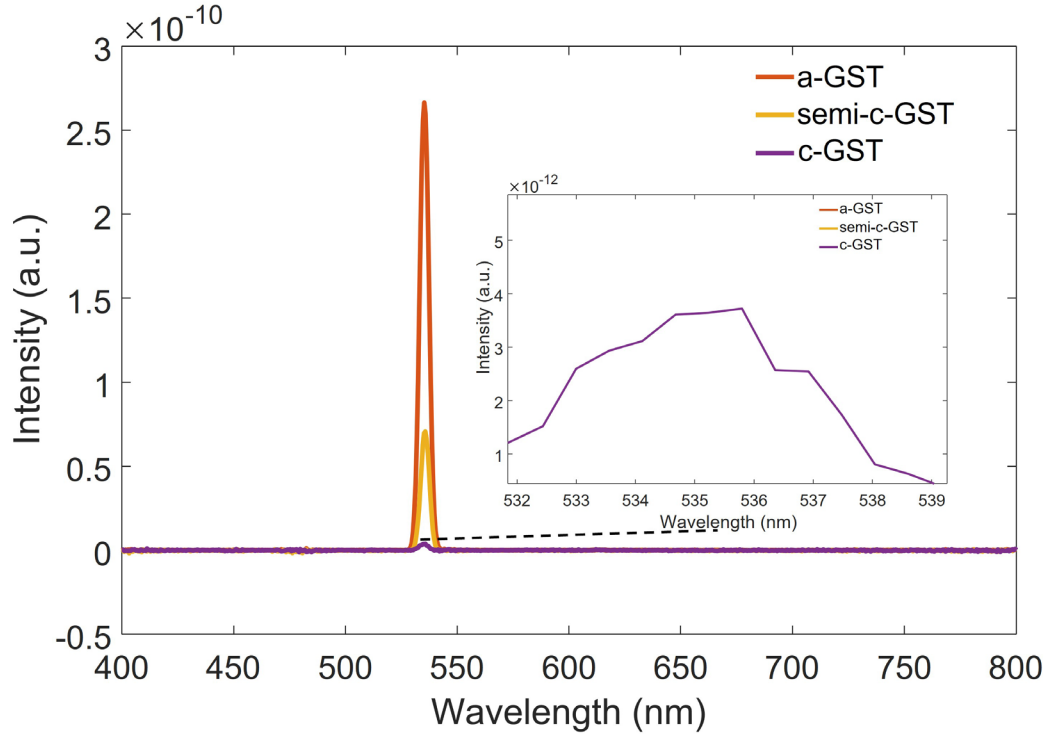


Figure 28 – Measured reflected NL emission intensity spectra, at the visible wavelengths, of the structure in Figure 22 for the a-GST, semi-c-GST, and c-GST states at a pump wavelength of 1600 nm.

2.3. The NL emission intensity in Figure 28 divided by the a.u. approximately represents corresponding emission efficiency. The NL emission peaks are located at or close to the λ_{TH} as expected. It can also be seen from Figure 28 that the a-GST state device exhibits the highest THG efficiency among the three considered crystallinity states. THG efficiency at the a-GST state is higher than that of Figure 4(d) (4.52×10^{-11}). The three-level switching presents a large modulation depth of ~ 20 dB at the λ_{TH} . This modulation depth is much smaller than that of ~ 70 dB by simulations possibly due to both fabrication imperfections and limited collimation of the incident beam in the measurement. According to Figure 28, the THG efficiency of the sample at the a-GST state is only a few times larger than that of the semi-c-GST state, whereas the THG efficiency of the sample at the semi-c-GST state is about a few tens of times larger than that of the c-GST state. This observation agrees with the blue-half of the simulated spectra in Figure 25(b) that the THG efficiencies exhibit smaller differences at more-a-GST states than at more-c-GST states for a certain λ_f shorter than the resonance wavelength of the a-GST state device.

4.4 Conclusion and Outlook

We presented a miniaturized, integrated, CMOS-compatible, tunable THG switch with extinction ratios of ~ 70 dB at the resonant band in theory and ~ 20 dB near the red-shifted resonance by experiments. By taking advantage of the large multi-level variation of the refractive index of GST, we demonstrated multilevel THG intensity modulation for long NIR fundamental wavelengths. The design mitigates the effect of GST loss on the THG MS with a hybrid structure that integrates a high-Q MS (formed using a-Si) and a subwavelength GST layer at a sufficiently large distance without increasing the device size considerably. Similar to Section 3.2.5, this structure can be combined with compact

microheaters using transparent conductive oxides (e.g., ITO) or robust metals (e.g., W) to form a novel μ s-scale switching platform for electrically tunable chip-scale NL optical devices.

This study also shows the high potential of PCM-based devices for realization of NL photonic switches and paves the way for more sophisticated designs for higher modulation depths. For example, the dielectric EIT MS requires precise coupling between the bright-mode and dark-mode resonators, which makes the design highly sensitive to material index variations and geometry errors. This is equivalent to low fabrication tolerance and advocates incorporating dielectric MSs of higher fabrication tolerance. Moreover, low-optical-loss PCMs (e.g., Sb_2S_3 and Sb_2Se_3) can be potentially hybridized with high-Q NL dielectric MSs at a smaller distance without substantial effect on the resonant nearfield enhancement in the MSs at the ON state of the switching. These PCMs are also promising for NL all-PCM MSs at the NIR fundamental wavelengths where there is no optical loss, which can simplify the design of ON/OFF switching of NL harmonic generation as the structure in Ref. [88] using GSST at the MIR fundamental wavelengths.

CHAPTER 5. NUMERICAL STUDY OF RECONFIGURABLE LINEAR AND NL FOCUSING Sb_2S_3 METASURFACES

This chapter presents a numerical demonstration of an all- Sb_2S_3 linear and THG MS, that exchanges foci of the MS at amorphous Sb_2S_3 (a- Sb_2S_3) and crystalline Sb_2S_3 (c- Sb_2S_3) states for FH and TH. The demonstration is practical towards NL imaging and microscopic applications. The content of this chapter is assembled from Ref. [187] published by the author.

5.1 Brief Introduction to NL All-Dielectric Metalenses

All-dielectric metalenses have been widely investigated as a promising candidate to replace ubiquitous bulky curved lenses. So far, most demonstrations of metalenses have relied on linear materials since NL materials significantly restrict the overall performance of metalenses [188]. However, to our interest, NL metalenses provide a future platform for applications in NL information processing, all-optical higher-order Fourier transformations, short laser pulse diagnostics, *etc.* [16]. More importantly, metalenses conveying information at both linear and NL frequencies could potentially reveal more information about the imaging object. Due to significant material dispersion of constituent high-index material (such as semiconductors), NL signal generation confocal with the linear signal is challenging.

Low-loss phase-change chalcogenide Sb_2S_3 has shown high-contrast optical constants in the switchable a- Sb_2S_3 and c- Sb_2S_3 states and intrinsic large third-order nonlinearities [41, 42], potentially enabling material platforms for efficient tunable-foci

metalenses that enable co-focusing of FH and TH signals. The following section describes the design idea to approach this objective.

5.2 Design of the NL All-Sb₂S₃ Metalens

For the sake of simplicity, a reconfigurable all-dielectric NL MS with wavefront shaping in one of the dimensions and single-element periodicity in the other dimension is designed. MS wavefront is shaped by arrays of eleven Sb₂S₃ nano-ellipsoids as depicted in Figure 29(a). The nano-ellipsoids are sitting on a SiO₂ substrate with square lattice period and height of 400 nm, with both semi-axial lengths in the range of 100 nm to 160 nm, which are set to exhibit resonance behaviors at 950-nm incidence for both crystallinity states of Sb₂S₃. Optical constants of a-Sb₂S₃/c-Sb₂S₃ are adopted from Ref. [41] with quasi-linear extrapolations at short wavelengths following the dispersion characteristics towards shorter wavelengths from real-part refractive index peaks of the two states, respectively.

The aim is to utilize unique dispersion relationship between a-Sb₂S₃ and c-Sb₂S₃ as shown in Figure 29(b) for the device works at the λ_f of 950 nm, where the refractive

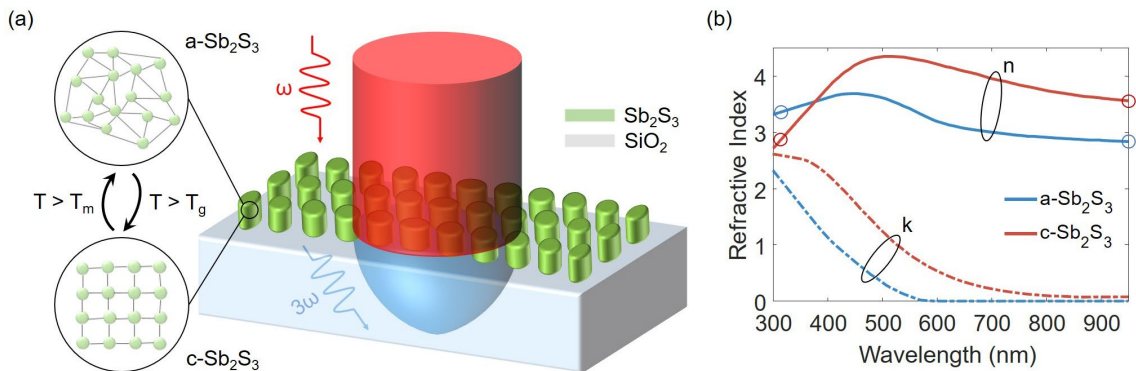


Figure 29 – (a) Schematic of the designed linear and NL tunable-foci MS. (b) Real (solid curves) and imaginary (dashed curves) parts of the refractive indices of a-Sb₂S₃ and c-Sb₂S₃ extrapolated from data in Ref. [41].

index of a-Sb₂S₃ ($n_{a-Sb_2S_3}$) at λ_f is close to that of c-Sb₂S₃ ($n_{c-Sb_2S_3}$) at λ_{TH} whereas $n_{c-Sb_2S_3}$ at λ_f is close to $n_{a-Sb_2S_3}$ at λ_{TH} . Circles with Sb₂S₃ state-correspondent color enclose the respective real-part index values in Figure 29(b). The principle of phase delay should bring foci of THG signal from the MS of one crystallinity state and the transmitted fundamental signal of the other crystallinity state closer.

5.3 Simulation Results and Discussion

A plane wave polarized in wavefront-shaping orientation is normal-incident on the MS in the simulations. The third-order NL optical coefficient of c-Sb₂S₃ is evaluated to be approximately 7 times that of a-Sb₂S₃ at 950 nm, with values comparable to the a-Si used in Ref. [101], according to the empirical Miller's rule [90].

Figure 30 shows the middle-incident-plane plots of the focusing nearfield of FH and TH induced by MS the a-Sb₂S₃ and c-Sb₂S₃ states, with scaling of length in the orientation normal to the MS. Figure 30(a) and Figure 30(b) are plotted for the FH in normalized nearfields and the TH in an a.u. at the a-Sb₂S₃ state, respectively. Figure 30(c) and Figure 30(d) are corresponding plots at the c-Sb₂S₃ state. Dashed ellipses mark the regions that exhibit focusing behaviors of the four conditions. Zeroth order THG signals are evidently identified to focus in the marked, although immersed in high-order diffraction signals. Figure 30(a) and Figure 30(d) show close transmission focusing regions of $\sim 8 \mu\text{m}$ from the air/SiO₂ interface for the FH at the a-Sb₂S₃ state and the zeroth order THG signal at the c-Sb₂S₃ state, respectively, whereas Figure 30(b) and Figure 30(c) show close transmission focusing regions of $\sim 5 \mu\text{m}$ from the air/SiO₂ interface for the FH at the c-Sb₂S₃ state and the zeroth order TH at the a-Sb₂S₃ state, respectively.

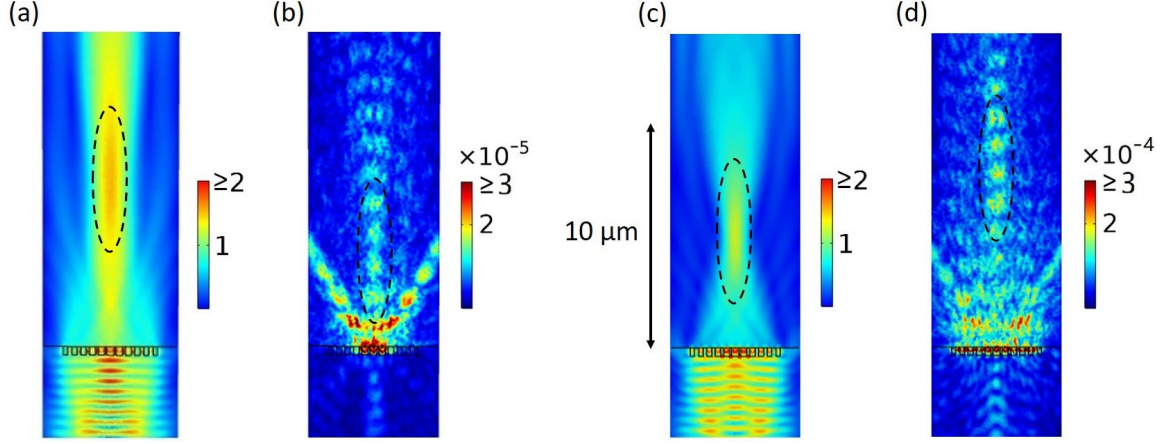


Figure 30 – Simulated middle-incident-plane nearfields for the MS of (a) a-Sb₂S₃ state @ $\lambda_f = 950$ nm and (b) a-Sb₂S₃ state @ $\lambda_{TH} = 317$ nm, in normalized fields and a.u., respectively; (c) c-Sb₂S₃ state @ $\lambda_f = 950$ nm and (d) c-Sb₂S₃ state @ $\lambda_{TH} = 317$ nm, in normalized fields and a.u., respectively, with length scale in the orientation normal to the MS and dashed ellipses enclosing regions of focus marked.

Above all, the double-frequency foci-reconfiguration is realized with the strong and unique refractive index reconfigurability between amorphous and crystalline states of low-loss PCM Sb₂S₃ in this study. The results can inspire the field of frequency-based microscopic image processing with reconfigurable NL metalenses.

CHAPTER 6. QUASI-BIC FOR BIDIRECTIONAL BREAKING-SYMMETRY NL METASURFACES

This chapter summarizes the numerical design and experimental demonstration of ultra-high Q factors and reconfigurable efficient THG with bidirectional symmetry-broken a-Si MSs, respectively. The symmetry-breaking tactic is based on the formation of quasibound states in the continuum. The theoretical linear Qs are up to the order of 10^5 , considering fabrication feasibility. The experimental demonstration shows the optical Kerr effect in THG, having potential for applications such as all-optical modulation and computing at NL harmonics. The content of this chapter is extended from Ref. [189] published by the author.

6.1 Introduction to BIC-based NL MSs

Highly efficient TH frequency conversion processes are typically realized by phase-matching techniques featuring precise material dispersion engineering in conventional bulk structures [190, 191]. It is known that subwavelength-scale structures can exhibit extraordinary optical properties that macroscopic material structures do not possess. Among ordered subwavelength-scale artificial structures, MSs have advantages over their 3D counterpart (MMs): lower optical losses and easier fabrication. Lower optical losses could improve spectral modulation depth and the reduced dimension of MSs can lead to faster optical switching [184, 192]. Moreover, resonant MSs have experimentally demonstrated sensible THG conversion efficiencies [26, 101, 193] without the need for phase matching.

Non-radiating sources of energy have been conventionally studied in quantum mechanics and astrophysics but recently explored in nanophotonics for localizing high-intensity electromagnetic fields within small volumes of matter [20], expected to provide stronger field localization than most radiating sources that dissipate a substantial portion of energy to the surrounding. Traditionally, non-radiating sources did not attract much attention from the photonics community because it was believed that such states forbid energy from propagating away from the source [20]. Recently, research interest in non-radiating electromagnetic states at optical wavelengths has been boosted by many studies on light propagation and interactions with all-dielectric resonant nanoparticle systems supporting multipolar Mie-type resonances [20, 194], including high-refractive-index dielectric MMs [195-197]. These structures can exhibit subwavelength confinement properties similar to plasmonic MSs [20], but with electromagnetic field enhancement deep within the resonators, instead of only exhibiting equivalently large field enhancement at the surface as lossy metal. This makes high-index dielectric MSs supporting non-radiating states favorable for high-order harmonic generation. High-odd-order NL optical susceptibilities of centrosymmetric high-index materials can be estimated by the relation $\chi^{(n)}(\omega) \propto \chi^{(1)}(n\omega) \cdot (\chi^{(1)}(\omega))^n$, where ω is the fundamental angular frequency, and $\chi^{(n)}$ is the n th-order optical susceptibility of the material [198]. Besides these characteristics, relatively high thermal damage thresholds and low optical loss of dielectric materials, with weak absorption of the pump power, also facilitate the studies of high-index dielectric MSs for high-order harmonic generation.

Non-radiating photonic BIC states have been widely discussed in the last decade. Optical BIC modes are currently classified as the symmetry-protected BIC [199],

accidental BIC [200, 201] (also called Friedrich-Wintgen BIC), and Fabry-Perot BIC [202, 203]). The symmetry-protected BIC is defined as BIC in which no outgoing wave exists for modes of a particular symmetry. Accidental BIC is defined as the outcome of radiation suppression for all incident angles and polarizations. Fabry-Perot BIC simultaneously exhibits Fano and Fabry-Perot resonances [204]. Real BIC modes are dark modes [204, 205] with infinite Q factors [26], therefore, the far field spectral characteristic of high-Q resonances can be potentially excited in terms of quasi-BIC and nearly BIC modes [204]. High-Q resonances can arise from quasi-BIC modes by distorting symmetry-protected BIC [21] to realize minimized but perceptible interaction with the continuum [26]. The demonstrations of symmetric distortions on meta-atoms to form quasi-BIC [26, 206], to the best of our knowledge, have lower geometric sensitivity and tolerance, compared to asymmetrically distorted meta-molecules [21]. Symmetry-breaking dielectric MSs with quasi-BIC modes generally exhibit magnetic-dipole Fano resonances under normal excitations [21, 207, 208]. Lower degree of symmetry breaking generally corresponds to higher Q factors that are typically restricted by the geometric resolution and error of EBL.

Si is the most promising material for efficient THG and generation of higher-order odd harmonics [102] using BIC MSs fabricated with mature techniques. There are demonstrations of symmetric c-Si quasi-BIC MSs. Liu *et al.* designed MSs of symmetric cut-corner meta-atoms 500 nm in height to achieve an ultra-high Q factor of $\sim 2 \times 10^4$ and an unprecedented THG conversion efficiency of $1.4 \times 10^{-8} [\text{W}^{-2}]$, as mentioned in Section 4.1 [26]. Fang *et al.* studied MSs of symmetric cut-edge meta-atoms (measuring 230 nm in height) with a high Q factor of ~ 3500 and THG efficiency was calculated to be enhanced 368 times compared to the flat Si film [206]. A-Si quasi-BIC NL MSs are more commonly

discussed than c-Si ones. Yang *et al.* observed an increase of up to 5×10^7 in THG from an a-Si BIC MS of nanopillars coupled to a gold reflector, compared to the unpatterned film, and a record high THG efficiency of 1.8×10^{-6} at a relatively low peak pump intensity of 0.4 GW/cm^2 , as mentioned in Section 4.1 [185]. Their quasi-BIC mode is formed by critical coupling between the MS and the reflector [185]. Bar-David *et al.* experimented with a 280-nm thick MS of asymmetric a-Si meta-atoms to manipulate SH light and control its diffraction patterns [97]. Gandolfi *et al.* numerically demonstrated near-unity third-harmonic circular dichroism with 575-nm thick MSs composed of parallel block pair arrays that have the broken pair symmetry in terms of block length [209]. Sinev *et al.* observed ultrafast TH resonance blue-shift and broadening due to laser-driven generation of free carriers and multiphoton absorption which change the material refractive index on time scales less than the pulse duration in MSs featuring quasi-BIC [208]. The structure is composed of 500-nm thick parallel block pair arrays that the pair symmetry was broken in block widths. These MS thicknesses were designed to fit the BIC resonance wavelengths to the NIR.

6.2 Theoretical Ultrahigh-Q a-Si MSs that Experimentally Reconfigure THG

6.2.1 Introduction to Optical Kerr Effect in NL MSs

The optical Kerr effect is caused by the multiplication of NL refractive indices (n_2) of materials and the local optical intensity. Yang *et al.* found a THG resonance red shift of 2.6 nm during a peak pump intensity (I_{PP}) increment from 0.8 GW/cm^2 to 1.6 GW/cm^2 , with the poly-Si MS exhibiting Fano resonance due to EIT [101]. The impressive Kerr effect on THG stems from the large simulated maximum nearfield enhancement of ~ 50 in

the dark-mode nano-resonator, joint with a high n_2 of Si $\sim 2.7 \times 10^{-18} \text{ m}^2/\text{W}$ [149] in the NIR wavelength range. However, as discussed in Section 4.4, the resonance strength is highly dependent on the coupling between the sensitive bright-mode and dark-mode nano-resonators, which is not robust to nano-resonator geometry and refractive indices of the surroundings to the MS.

It is in our interest to explore symmetry-breaking methods, which aim at larger nearfield enhancement at higher Q factors in fabricatable BIC-based Si MSs that are flexible to geometric errors and the surrounding environment, can be a potential approach to realize more efficient subwavelength-scale THG and robust optical-Kerr-based switching of THG. In this study, we demonstrate a-Si MSs featuring quasi-BIC with both co-polarized and cross-polarized symmetry breaking from parallel block pairs for efficient THG. Compared with the studies that only break symmetry in width [208] or length [209] of the nano-blocks, we expect much larger theoretical resonant nearfield enhancement / Q factors, given a same feature resolution considering fabrication reality. Although the experimental Qs of the bidirectional symmetry-broken MSs are limited by fabrication imperfections and characterization constraints, we observe a substantial optical Kerr effect through efficient THG responses at $I_{\text{PP}} \sim 1.33 \text{ GW}/\text{cm}^2$ and $I_{\text{PP}} \sim 3.34 \text{ GW}/\text{cm}^2$.

6.2.2 *Design and Fabrication of the a-Si MSs*

The a-Si MS is composed of unit cell arrays of two identical nano-blocks with two mirror-symmetric corners cut in each nano-block, which are placed on a SiO_2 substrate as shown in Figure 31(a). The square lattice period of unit cell p is 740 nm and the respective corners of adjacent parallel nano-blocks are $p/2$ distant as shown in Figure 31(a). The

height of the nano-blocks is set to 300 nm and the width of the nano-blocks W is set in the range of 220 nm to 230 nm in the simulation, to fit the linear resonance to 1200–1400 nm and compare with experimental results. The length of the nano-blocks is $2W$ as shown in Figure 31(a). The cut-corners break the spatial symmetry of the two nano-blocks. A unitless asymmetric factor $\alpha = 2\Delta L / L$, where L and $L - 2\Delta L$ are the widths of the two nano-blocks, was introduced in a theoretical modeling [25] to denote the degree of symmetry breaking in one-dimensional (1D) widths of the two nano-blocks. The breaking of symmetry is applied in the study by shortening each end of one of the nano-blocks in the unit cell by ΔL in width. It was concluded in the study that the radiative Q of the 1D-symmetry-breaking MS is proportional to α^2 under normal excitation polarized along the non-symmetry-breaking long axes of the nano-blocks [25]. A higher Q factor in the quasi-BIC structure means a larger resonant nearfield enhancement in the meta-molecules. We devise the evolved structure that breaks the symmetry in both co-polarized and cross-polarized directions with the dimensions of the cut-corners. The MS is designed with a minimum geometric feature difference, defined as the minimum differences in corresponding dimensions between the two blocks, of 10 nm, considering fabrication feasibility. The cut corners on the left and right nano-block are squares and rectangles, respectively, but their perimeters are identically 360 nm. The width d of cut-corners in the right nano-block is set to 80 nm, 70 nm, or 60 nm in simulations, which makes the parallel cut-corner nano-blocks very similar in planar size with a minimum area difference of 200 nm². These cut corners are designed to not affect the field confinement, by making them much smaller than the nano-bar. Figure 31(b) shows a control structure unit cell that is evolved, similar to cut corners from the nano-blocks of $W = 220$ nm before corners being cut in Figure 31(a), but

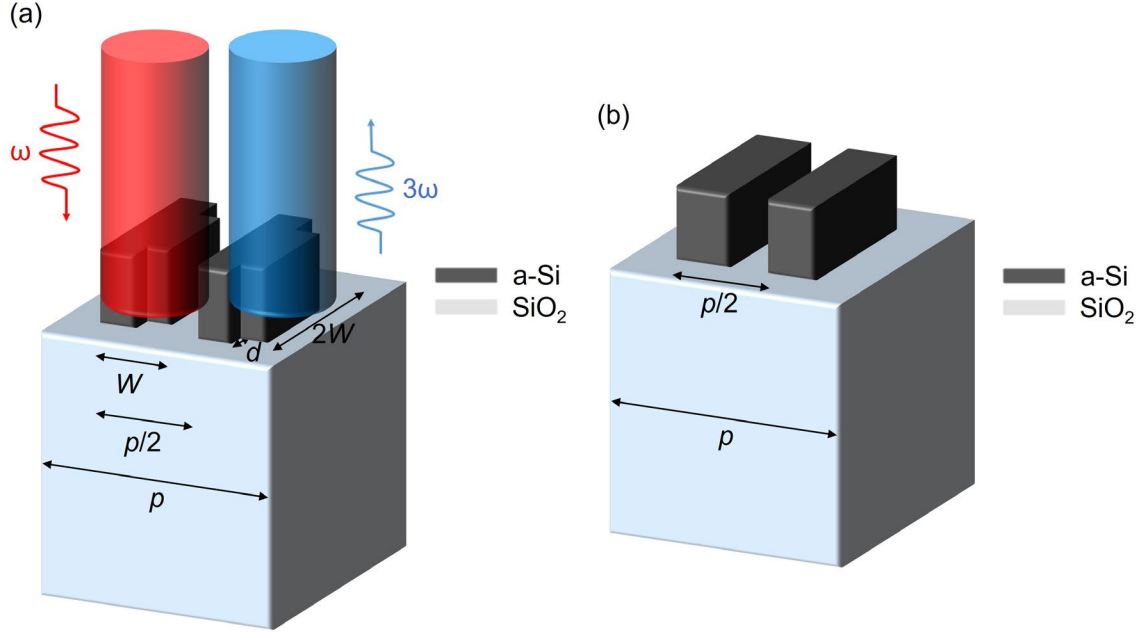


Figure 31 – (a) Unit cell schematic of the normal-reflection-mode MS that comprises two identical nano-blocks with two mirror-symmetric corners cut in each nano-block on a SiO_2 substrate. Critical dimensions are marked as denotations. The square lattice period of unit cell p is 740 nm and the respective corners of adjacent parallel nano-blocks are $p/2$ distant. The height of the nano-blocks is 300 nm, and the width of the nano-blocks W is in the range of 220 nm to 230 nm to fit the linear resonance to 1200–1400 nm. The length of the nano-blocks is $2W$. The perimeter of all cut corners is 360 nm and those from the left nano-block are squares. The width d of cut-corners in the right nano-block is 80 nm, 70 nm, or 60 nm, which makes the parallel cut-corner nano-blocks very similar in planar size with a minimum area difference of 200 nm^2 . (b) A control structure unit cell also evolved from the identical nano-blocks of $W = 220$ nm as in (a), but the width of its right nano-block is 210 nm, resulting in a planar area difference between the symmetry-breaking nano-blocks of 4400 nm^2 . The square lattice period of unit cell p is 740 nm and the respective corners of the parallel nano-blocks are $p/2$ distant, same as in (a).

the width of its right nano-block is 210 nm, which is similar to the structure in an aforementioned study [208]. These structures are used to determine the better symmetry-breaking tactic for optimizing THG output intensity by comparing their numerical linear response. If the planar area of the right meta-atom is A , then the planar area difference between the two meta-atoms ΔA in Figure 31(b) is 4400 nm^2 , which is much larger than that of 200 nm^2 given by Figure 31(a), given the minimum feature difference of 10 nm.

Therefore, the structure in Figure 31(a) is expected to exhibit a higher Q factor and nearfield enhancement than the structure in Figure 31(b) at the BIC resonance.

For the sake of simplicity, we simulate the resonant linear nearfield responses considering only normal excitation of the MS polarized along the long axes of the nano-blocks. The a-Si refractive indices used in the simulations are calculated from ellipsometry data of the samples we deposited in a study of linear MSs [59]. The mesh element sizes are set to be no larger than 1/10 of the wavelengths of incidence in media to ensure accuracy. All planar corners of the MS geometry are rounded with a fillet of 20 nm in radius, to reduce computational singularity in the simulations. Samples for the structure in Figure 31(a) with $w = 80$ nm, i.e., the smallest planar area difference of 200 nm^2 between the cut-corner nano-blocks, are fabricated. The fabrication starts with PECVD ($\sim 100^\circ\text{C}$) of a-Si for a 300-nm-thick low-stress film. The a-Si deposition is done by the Unaxis PECVD as in Section 4.3.1. The a-Si MS is fabricated by EBL patterning and ICP etching of the a-Si film. XR-1541-006 negative-tone e-beam resist, i.e., a solution of 6% HSQ, is used. The spin coated and e-beam exposed resist is developed with a solution of 25% tetramethylammonium hydroxide (TMAH) at $\sim 40^\circ\text{C}$. The etching process is conducted using chlorine (Cl_2) in the Plasma Therm ICP tool at IEN. The left-over HSQ on the a-Si cut-corner nano-blocks is not removed at the end for both simplicity and impedance matching of the top HSQ/a-Si and bottom a-Si/ SiO_2 interfaces at the MSs, as described in Section 4.3.1. Figure 32 shows a flowchart of the fabrication process. Figure 33 presents top-view scanning SEM images of a unit cell of the fabricated structure in Figure 31(a) with $W = 220$ nm (left, Sample 1) and $W = 230$ nm (right, Sample 2). The cut-corner sizes in the two images are expected to match as the variation of W is controlled by adjusting the

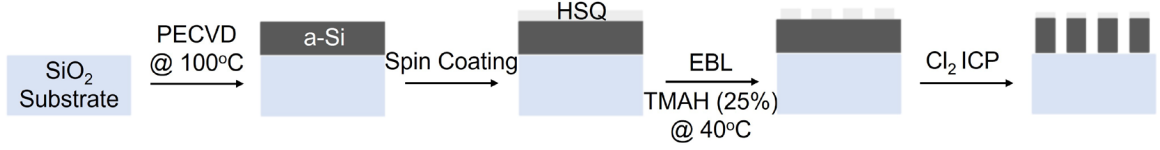


Figure 32 – Fabrication process for the a-Si MS samples with left-over HSQ, in which low-temperature PECVD of a-Si, EBL of spin coated HSQ, and ICP etching with Cl_2 were conducted.

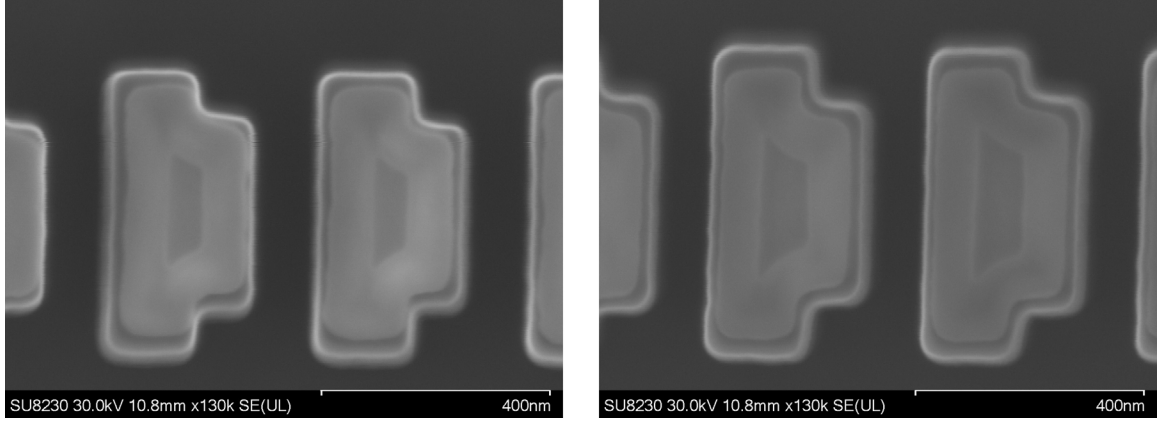


Figure 33 – Top-view SEM images of a unit cell of the fabricated structure in Figure 31(a) with $W = 220$ nm (left, Sample 1) and $W = 230$ nm (right, Sample 2), with the scaling measure marked. The left/right image shows the square-corner-cut nano-block on the right/left.

exposure dose to a fixed computer-aided design pattern of $W = 220$ nm during EBL. The left/right image shows the square-corner-cut nano-block on the right/left. Both SEM images have a scaling measure of 400 nm. There is an enclosed contour clearly in contrast to other parts for each cut-corner nano-block in the images, possibly due to the non-uniform thickness of the left-over HSQ after development and etching.

6.2.3 Results and Discussion

Figure 34(a) and Figure 34(b) show the simulated plots of the normalized nearfields at middle-plane intersections of all axes based on each pre-symmetry-breaking nano-block, due to incidence at the quasi-BIC resonances ~ 1217.24 nm and ~ 1248.8 nm for the base

structure in Figure 31(a) ($W = 220$ nm, $d = 80$ nm) and the structure in Figure 31(b), respectively. The nearfield enhancement in Figure 34(a) is much larger than Figure 34(b), as expected, indicating a larger resonant THG efficiency for the base structure in Figure 31(a) than the structure in Figure 31(b), in theory. The nearfield enhancement in Figure 34(a) is almost the largest in reported structures that have the potential to be achieved with adequate fabrication precision. The relation of a higher nearfield enhancement to a higher Q factor is as anticipated by comparing the nearfield enhancements in Figure 34(a) and Figure 34(b) to the linear Q factors marked in Figure 34(c) and Figure 34(d) showing the simulated reflectance spectra in the vicinity of Figure 34(a) and Figure 34(b), respectively. All reflectance Qs in this work are defined as the ratio of the resonance (or dip) frequency to the FWHM of the dip in the reflectance spectrum. The half-maximum level of a simulated reflectance dip is approximated by averaging the dip reflectance and the highest reflectance in the vicinity of the dip. The dip in Figure 34(c) is shallower than that in Figure 34(d), which is possibly attributed to more mode leakage in Figure 34(a) that can be contributed through the cut corners, compared to Figure 34(b). In addition, it can be observed that the resonance mode in Figure 34(a) has relatively higher field enhancement in a-Si than that of Figure 34(b), which further enhances potential for the Figure 31(a) structure in efficient THG, given the geometry scale. The Fano parameter [19] characterizes the degree and orientation that a Fano line shape deviates from Lorentzian. The obviously different modes in Figure 34(a) and Figure 34(b) can be the main origin for different signs of the Fano parameter clearly speculated from the nearly mirror-symmetric Fano line shapes in Figure 34(c) and Figure 34(d).

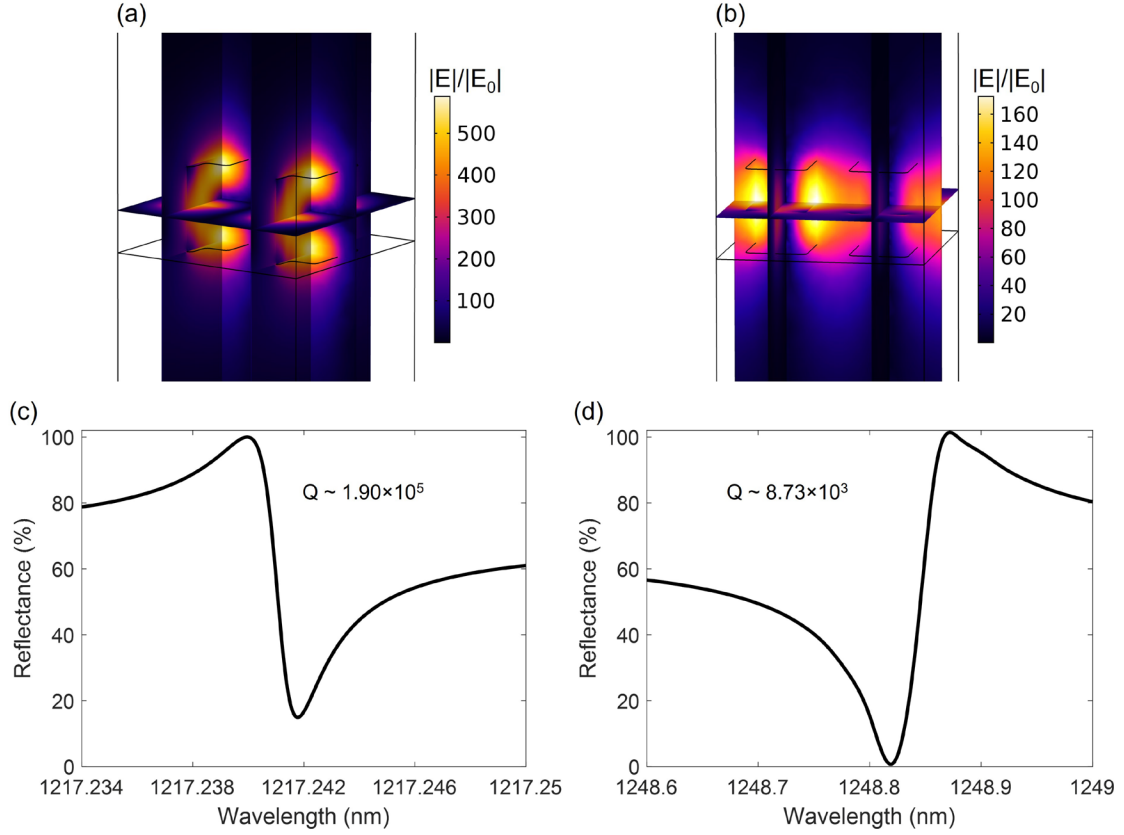


Figure 34 – Simulated plots of the normalized nearfields at middle-plane interceptions to all axes based on each pre-symmetry-breaking nano-block, due to incidence at the quasi-BIC resonances (a) ~ 1217.24 nm for the structure in Figure 31(a) with $W = 220$ nm and $d = 80$ nm; (b) ~ 1248.8 nm for the structure in Figure 31(b). Simulated reflectance spectra (c) and (d) marked with Q factors in the vicinity of (a) and (b). The reflectance Qs are defined as the ratio of the dip frequency to the FWHM of the dip in the reflectance spectrum. The half-maximum level of a reflectance dip is approximated by averaging the dip reflectance and the highest reflectance in the vicinity of the dip.

In order to compare the resonant nearfield profiles and Q factors under different ΔA s in the symmetry-breaking cut-corner nano-blocks, without changing A and the electromagnetic mode, we also simulate for the structure in Figure 31(a) with design parameter combinations of $W/d = 220$ nm / 70 nm and $W/d = 220$ nm / 60 nm. Figure 35(a), Figure 35(b), and Figure 35(c) show the simulated cross-planar plots of the normalized nearfields for incidence at the quasi-BIC resonances ~ 1217.24 nm, for the base structure

of $W/d = 220 \text{ nm} / 80 \text{ nm}$ (simplified from Figure 34(a)), $\sim 1217.9 \text{ nm}$ for the structure in Figure 31(a) with $W/d = 220 \text{ nm} / 70 \text{ nm}$, and $\sim 1219.4 \text{ nm}$ for the structure in Figure 31(a) with $W/d = 220 \text{ nm} / 60 \text{ nm}$, respectively. The slight redshift of the resonance wavelength is due to a very small size increase in the right cut-corner nano-block from Figure 35(a) to Figure 35(c). It is observable that the maximum nearfield enhancement in Figure 35(b) is only $\sim 1/4$ of that in Figure 35(a), and about twice that in Figure 35(c). The reflectance Q_s for Figure 35(b) and Figure 35(c) are $\sim 1.42 \times 10^4$ under $\Delta A = 800 \text{ nm}^2$, and $\sim 2.97 \times 10^3$ under $\Delta A = 1800 \text{ nm}^2$, respectively. Let the maximum nearfield enhancement be M and note the reflectance Q for Figure 35(a) is 1.90×10^5 under $\Delta A = 200 \text{ nm}^2$, the results approximately follow $Q \propto M^2 \propto \Delta A^{-2}$ given the same structure geometry before breaking symmetry. This strongly matches existing theory [25] and consolidates our design strategy.

In addition to comparison with experimental results, since Figure 34(c) and Figure 34(d) show possible effect of mode leakage by the cut-corners in nano-blocks, the structure in Figure 31(a) is simulated for design parameter combinations of $W/d = 225 \text{ nm} / 80 \text{ nm}$

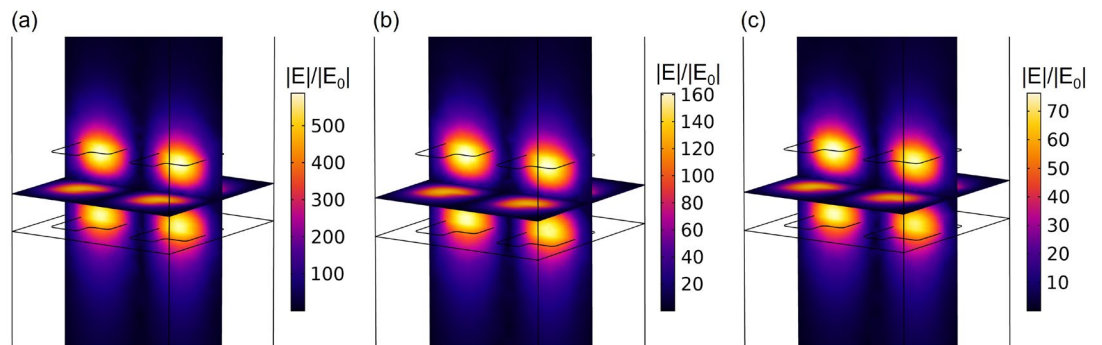


Figure 35 – Simulated cross-planar plots of the normalized nearfields for incidence at the quasi-BIC resonances (a) $\sim 1217.24 \text{ nm}$ (simplified from Figure 34(a) of $W/d = 220 \text{ nm} / 80 \text{ nm}$), (b) $\sim 1217.9 \text{ nm}$ for the structure in Figure 31(a) with $W/d = 220 \text{ nm} / 70 \text{ nm}$, and (c) $\sim 1219.4 \text{ nm}$ for the structure in Figure 31(a) with $W/d = 220 \text{ nm} / 60 \text{ nm}$.

and $W/d = 230 \text{ nm} / 80 \text{ nm}$, to compare with the base structure of $W/d = 220 \text{ nm} / 80 \text{ nm}$ by varying A without changing the sizes of the cut corners. Figure 36(a), Figure 36(b), and Figure 36(c) show the simulated reflectance spectra in the vicinity of the quasi-BIC resonance and inset middle intercept planar plots of the normalized nearfields for incidence at the resonances $\sim 1217.24 \text{ nm}$ for the base structure of $W/d = 220 \text{ nm} / 80 \text{ nm}$, $\sim 1230.16 \text{ nm}$ for the structure in Figure 31(a) with $W/d = 225 \text{ nm} / 80 \text{ nm}$, $\sim 1242.24 \text{ nm}$ for the structure in Figure 31(a) with $W/d = 230 \text{ nm} / 80 \text{ nm}$, respectively. The reflectance Qs are marked in the plots and planar contours of the cut-corner nano-blocks are marked by solid lines. The resonance wavelength in Figure 36(b) is approximately the average of those of Figure 36(a) and Figure 36(c), which is natural as the increment in A from Figure 36(a) to Figure 36(b) is approximately that from Figure 36(b) to Figure 36(c). It is clear that the cut corners occupy substantial amount of resonance mode localization. The reflectance dip that gradually deepens from Figure 36(a) to Figure 36(c) can be interpreted as decreased mode

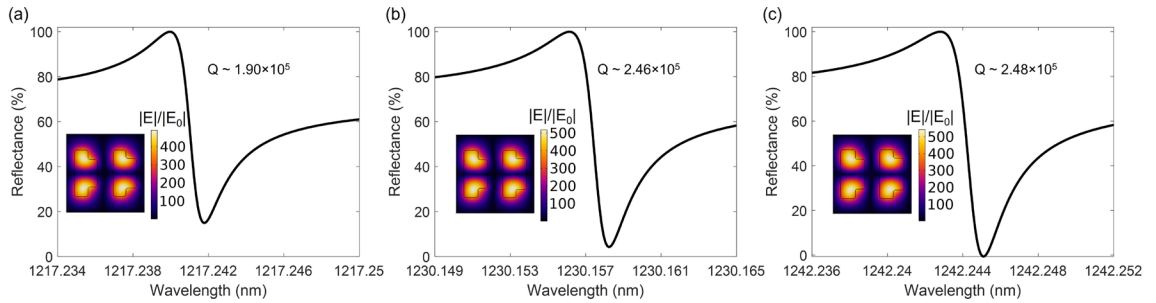


Figure 36 – Simulated reflectance spectra in the range of the quasi-BIC resonance and inset middle intercept planar plots of the normalized nearfields for incidence at the resonances (a) $\sim 1217.24 \text{ nm}$ for the base structure of $W/d = 220 \text{ nm} / 80 \text{ nm}$, (b) $\sim 1230.16 \text{ nm}$ for the structure in Figure 31(a) with $W/d = 225 \text{ nm} / 80 \text{ nm}$, (c) $\sim 1242.24 \text{ nm}$ for the structure in Figure 31(a) with $W/d = 230 \text{ nm} / 80 \text{ nm}$. The reflectance Qs are marked in the plots and planar contours of the cut-corner nano-blocks are marked by solid lines. The reflectance Qs are defined as the ratio of the dip frequency to the FWHM of the dip in the reflectance spectrum. The half-maximum level of a reflectance dip is approximated by averaging the dip reflectance and the highest reflectance in the vicinity of the dip.

leakage as d/W decreases. Meanwhile, the nearfield enhancement exhibits slight increments from Figure 36(a) to Figure 36(c), which can be due to slightly more localized mode at a very small decrease in d/W as well as the slight decrease in the degree of symmetry breaking $\Delta A/A$. The Q factor increases accordingly with the nearfield enhancement, however, the increment from Figure 36(a) to Figure 36(b) is tens of times larger than that from Figure 36(b) to Figure 36(c). This can be largely due to our FWHM-based Q-factor calculation method that involves the level of reflection dip, which decreases a lot more from Figure 36(a) to Figure 36(b) than that from Figure 36(b) to Figure 36(c).

Figure 37(a) / Figure 37(b) present measured linear reflectance spectrum (dashed) joint with THG efficiency spectra in an a.u. at I_{PPS} of $\sim 1.33 \text{ GW/cm}^2$ and $\sim 3.34 \text{ GW/cm}^2$, for Sample 1 / Sample 2. The linear spectra exhibit Q factors of ~ 300 , according to half-maximum levels of the measured linear reflectance dips approximated by averaging the dip reflectance and the highest reflectance in the blue region of the dip. The approximation is aligned with the line shape. The Q factors are very small compared to those in theory, and the reflectance dips are much shallower than those simulated. These are due to fabrication imperfections, limited collimation of the incidence, and resolution of the spectrometer in the measurement. The overall reflectance level of Sample 2 is slightly higher than Sample 1, because of slightly more area covered with a-Si in Sample 2 than Sample 1, which is clear in Figure 33. The maximum reflectance in Figure 37(b) is slightly greater than unity. This is due to the uncollimated incidence that some light that is not collected when measuring the reference might be scattered by the MS into the objective lens when measuring the sample. Sample 1 has THG efficiency levels in the order of 10^{-11} at the two pump intensities. Since the THG intensity $I(3\omega) \propto I(\omega)^3$ regardless of NL

absorption, the THG efficiency $I(3\omega)/I(\omega) \propto I(\omega)^2$ under the assumption. The ratios of resonant THG efficiencies between the lower peak pump intensity $I_{\text{PPL}} = 1.33 \text{ GW/cm}^2$ and the higher peak pump intensity $I_{\text{PPH}} = 3.34 \text{ GW/cm}^2$ are both ~ 5.5 in Figure 37(a) and Figure 37(b), which is slightly smaller than $(I_{\text{PPH}}/I_{\text{PPL}})^2$. This should be mainly due to increasing NL absorptivity at the higher pump intensity in the lower saturation regime. There are exhibited THG resonance redshifts in Figure 37(a) although the collected data points are limited. In Figure 37(a), the THG efficiency at 404.7 nm is lower than that at 403.7 nm for $I_{\text{PP}} = 1.33 \text{ GW/cm}^2$, whereas the THG efficiency at 404.7 nm is higher than that at 403.7 nm for $I_{\text{PP}} = 3.34 \text{ GW/cm}^2$. In Figure 37(b), the THG efficiency at 421 nm exhibits a substantially more relative increase from that at 420 nm for $I_{\text{PP}} = 3.34 \text{ GW/cm}^2$ compared to $I_{\text{PP}} = 1.33 \text{ GW/cm}^2$. This is the first demonstration of BIC MSs featuring the optical Kerr effect in THG to the best of our knowledge on reported structures. The characteristics are most likely due to the concentrated large nearfield enhancement in a-Si with high $\chi^{(3)}$ and n_2 at the linear resonance. The level of THG efficiency in Figure 37(b) is

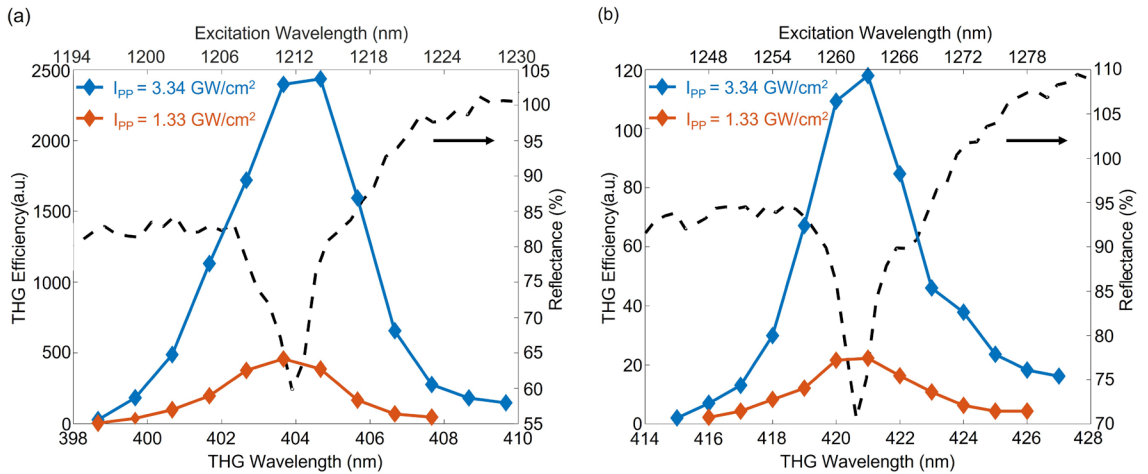


Figure 37 – Measured right-y-axis-calibrated linear reflectance spectrum (dashed) joint with THG efficiency spectra at peak pump intensities (I_{PPs}) of $\sim 1.33 \text{ GW/cm}^2$ and $\sim 3.34 \text{ GW/cm}^2$, for (a) Sample 1 and (b) Sample 2.

much lower than that of Figure 37(a), though the dimensions of Sample 2 should result in slightly higher resonant nearfield enhancement than that of Sample 1. This could be caused by increased visible light scattering loss at a rougher geometric resolution of Sample 2 patterned at a higher e-beam dose than Sample 1. The device performance can be improved for further studies by optimizing the fabrication process under the current precision and enhancing collimation of the optical paths in the characterization setups.

6.2.4 The Characterization Setups

Though the structure in Figure 31(a) exhibits some transmittance in the vicinity of resonance, most incident power is reflected which is indicated in Figure 37(a) and Figure 37(b). Due to the momentum conservation of photons in high-order harmonic generation [210], most THG power is also expected to be reflected. In addition, high collimation is needed for the high-Q MS. Thus, the linear and THG characterization setups presented in Figure 38 and Figure 39, respectively, are the same as those in Section 2.4. THG-excitation

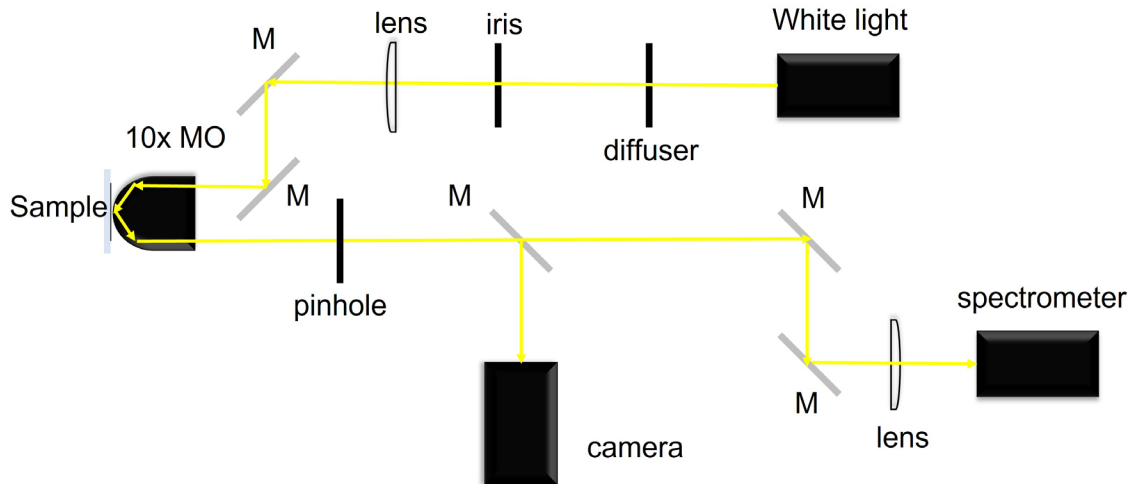


Figure 38 – The setup schematic for the linear reflectance measurement of the a-Si BIC MS samples, where ‘M’ and ‘10× MO’ represent a mirror and the 10× microscopic objective lens, respectively.

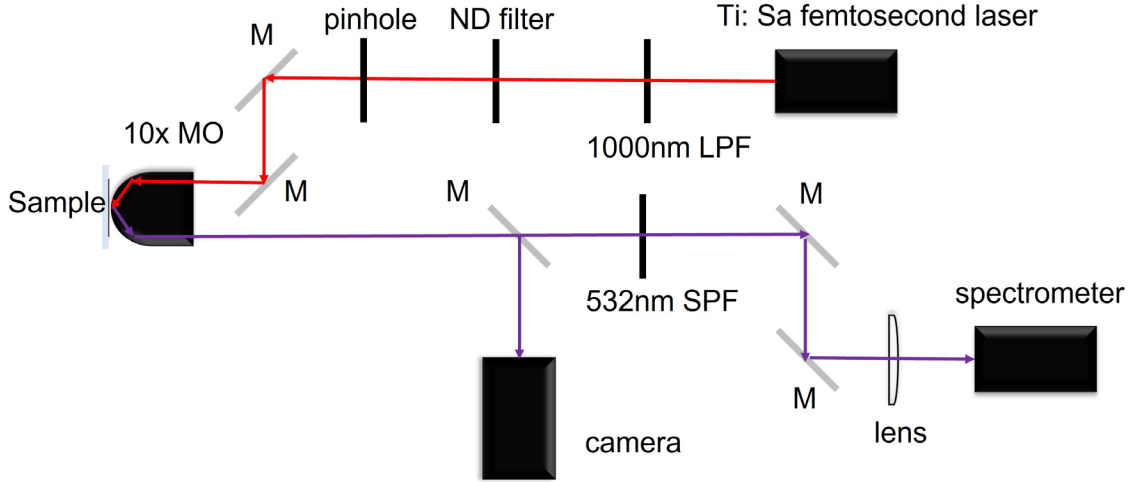


Figure 39 – The setup schematic for the THG measurement of the a-Si BIC MS samples, where ND, LPF, and SPF represent neutral density, long-pass filter, and short-pass filter, respectively.

power dependences of the samples were not measured for the same reason as that in Section 4.3.1.

6.2.5 Conclusion and Outlook

We demonstrate a bidirectional symmetry-breaking a-Si MS for efficient THG conversion based on a novel and robust quasi-BIC scheme. Our presented design outperforms most state-of-the-art demonstrations in terms of nearfield enhancement with a more practically feasible structure, which is promising for high-efficiency subwavelength-scale high-order harmonic generation. We observe the optical Kerr effect by comparing the THG resonance from the MS at two different peak pump intensity levels. This observation paves the way for structural modification of subwavelength-scale quasi-BIC designs for all-optical switching of NL harmonic generation. This includes SHG resorting to either the surface $\chi^{(2)}$ of centrosymmetric media [168, 169] or the bulk $\chi^{(2)}$ of non-centrosymmetric media [211]. The quasi-BIC design could potentially be extended for

other $\chi^{(3)}$ processes such as FWM [103, 212] and TPA [27, 66] due to highly intensified optical field in the $\chi^{(3)}$ medium, which provides a compact platform for possible mixtures of the $\chi^{(3)}$ processes to realize multiple functions.

CHAPTER 7. DL-BASED PREDICTION OF THG RESONANCE FOR SI METASURFACES

This chapter presents an image-classification-targeted CNN prediction method on binary-pixelated free-form Si MSs, with high accuracies of ~ 0.7 and ~ 0.8 for three classes of THG resonance wavelength range and three classes of resonant THG output intensity levels, respectively. This method expedites the design process of THG MSs by ultrafast filtration of patterns for certain ranges of NIR resonant excitation wavelengths and high-level THG output, which can be referenced in the design of NL MSs of other geometry, materials, and processes.

7.1 Brief Introduction

Symmetry-breaking MSs have attracted extensive research attention due to the potential of achieving high-Q resonances featuring quasi-BIC, especially for those based on high-index lossless dielectric materials (e.g., Si). However, efficient THG output from irregular-shape symmetry-breaking MSs has remained elusive, due to the near-infeasibility of theoretical analysis and computation complexity of forward design with electromagnetic simulation attempts.

The recent era has witnessed the application of AI and ML methods in metaphotonics. Most studies leverage DL networks to inversely design nanostructures [213] or discover underlying physics [125] that are in general associated with very-high dimensional data. Precise DL predictions of NL harmonic generation from irregular-shape MSs can be challenging. As described in the last paragraph of Section 1.3, this is due to

that training data generated by NL optical simulations are more complex and prone to larger errors than linear simulations. Labeling the training data of rough NL responses with discrete classes can convert the prediction study to a classification problem. Random binary-pixel-patterned Si MSs of fixed period and thickness are classified by two representative THG resonance characteristics in this work.

7.2 Simulations and the CNN

The random MSs are composed of binary-pixelated Si nano-resonators on a SiO₂ substrate, and work in a transmission mode at normal incidence of a plane wave from air, as shown in Figure 40(a). The nano-resonators are designed to be contractible in shape for the consideration of easy fabrication. The MSs have a thickness of 200 nm and are arranged in a square lattice with a period of 1000 nm. The unit cell of this periodic structure has one nano-resonator, and the binary-pixelated pattern is located within a 16-by-16 matrix with a resolution of 50 nm. The resolution is selected considering a trade-off between pattern complexity and fabrication feasibility. Our binary matrices tend to have comparable numbers of ‘0’ and ‘1’ digits according to the generation method, however, largely vary in sequences. The contractible patterns are generated by compressing ‘0’s to the center of the random binary matrices in the column and row directions (magnetic and electric field directions of an incident plane wave in Figure 40(a)) sequentially, where a ‘0’ indicates that there is 200-nm-thick Si in the corresponding square area of the side length of 50 nm. Linear simulations of 15000 random binary MSs are first conducted. Most of these MSs exhibit linear magnetic-dipole resonances in the wavelength range of 1450–1650 nm, so that the λ_f of THG resonance for each pattern is selected from this range. Since the intensity of the TH source at a node in the THG simulation $I(3\omega) \propto I(\omega)^3 \propto E(\omega)^6$, where $I(\omega)$ and

$E(\omega)$ are simulated local optical intensity and electric field amplitude at the FH, respectively. Regardless of THG scattering and mode overlap with the FH, the λ_f of THG resonance for each MS is determined by a simple indicator of the maximum volume integration of the sixth power of electric field amplitude over the nano-resonator. The Si refractive indices used in the simulations are the same as those for Section 6.2.2. The $\chi^{(3)}$ of Si is assumed to be uniform. The NL simulation result THG output intensity is represented by the transmitted THG power flow component in the direction perpendicular to the air/SiO₂ interface.

THG resonance wavelengths inferred from the linear simulations and output intensities calculated from the NL simulations are classified into three groups each by range and level, respectively. The ranges and levels are continuous segments to fit the groups with comparable number of samples for classifications of resonance and output intensity, respectively. With the given patterns and assigned classes, we train a CNN composed of 2

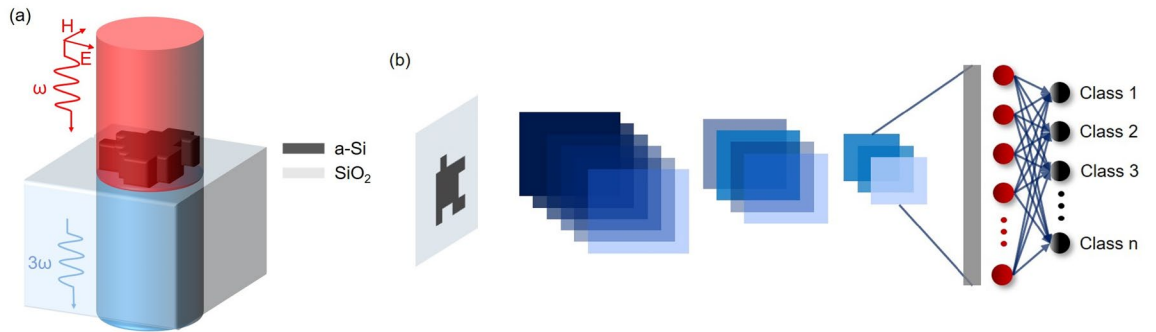


Figure 40 – (a) Example schematic of the unit cell of a square-lattice MS with a single random binary-pixelated contractible Si nano-resonator on a SiO₂ substrate, which works at plane-wave normal incidence from air and a transmission mode. (b) An illustration of the CNN structure for predicting the THG response of the MS with a unit cell as that in (a). The CNN is composed of 3 blocks of convolutional layers (each one includes 2 convolutional layers with ReLU activation function and a maximum pooling layer); a fully connected layer with 512 nodes; and fully connected layers with 256 nodes, 128 nodes, and 3 nodes (2 layers for each number of nodes in a layer).

blocks of convolutional layers (each one includes two convolutional layers with rectified linear unit (ReLU) activation functions and a maximum pooling layer), and 2 fully connected layers with 100 and 50 nodes, respectively. An illustration of the CNN structure for predicting the THG response of the MS with a unit cell as that in Figure 40(b). The categorical cross-entropy loss function is minimized over the training set using the Adam optimizer. From all the 15000 samples, we use 70% for training, 10% for validation, and 20% for testing the model, which can potentially predict THG resonance range and output intensity level for the Si MS structure of given patterns.

7.3 Results and Discussion

The inferred fundamental wavelengths of THG resonance are labeled into classes of 1450–1461.3, 1461.3–1471.1, and 1471.1–1650 in nanometers. The wavelength intervals gradually shrink along shorter wavelengths as the structures tend to exhibit THG resonances closer to the λ_f of 1450 nm. The simulated resonant THG output intensities are labeled into classes of $10^{-4.5}$ – $10^{-1.4}$, $10^{-1.4}$ – $10^{-0.9}$, and $10^{-0.9}$ – $10^{10.5}$ in an a.u. The medium level is narrower than the low and high levels in the exponential scaling range due to the regular Mie-type resonance that most likely happens in these structures, which is more common than resonance destruction and the formation of high-Q quasi-BIC. Though the high-level TH output intensities that are most likely generated with high-Q quasi-BIC occupy the broadest exponential range among the three levels, thus, are most sparsely distributed, the broad range of high-level THG intensities indicates high potential for the studied structures to exhibit high-intensity THG outputs. Prediction accuracies / confusion matrices for the THG resonance wavelength and the resonant THG output intensity data are shown in Figure 41(a) and Figure 41(b), respectively. Each value in the confusion

matrix shows the proportion of the associated predicted label among the associated true label. We have achieved prediction accuracies of ~ 0.7 for the THG resonance wavelengths and ~ 0.8 for the resonant THG output intensities. Both accuracies are moderately high considering that discriminating adjacent classes is challenging. The accuracy for the THG intensity is slightly higher than that for THG resonance wavelength due to that there are slightly more samples in the group of the medium THG level than those of the other two levels, while the resonance wavelength labels are more balanced in distribution. The classification of THG output intensity levels is slightly biased towards the medium level of relatively more samples and most adjacent levels. The bias can possibly increase the probability that the predicted intensity level matches the true intensity. As can be observed in Figure 41(a) and Figure 41(b), Misclassifications occur more in the adjacent classes and the error rate is considerably lower for non-adjacent classes. This also supports the fact that discriminating adjacent classes in THG resonance wavelengths and intensities is more

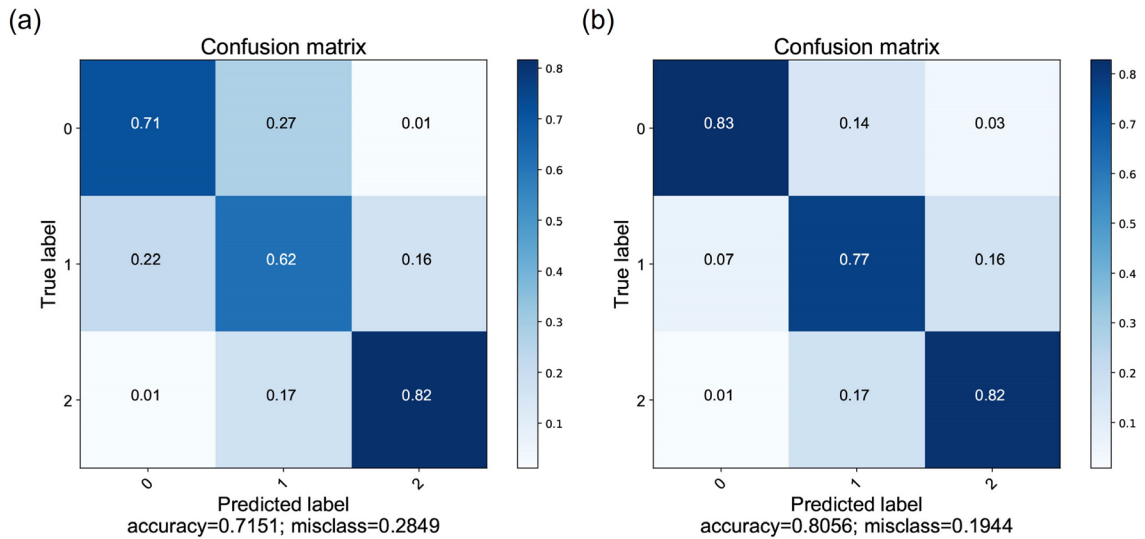


Figure 41 – Model prediction accuracies and confusion matrices for (a) the THG resonance wavelength and (b) the resonant THG output intensity data of the binary-pixelated MSs.

challenging compared to non-adjacent classes, due to larger errors in NL electromagnetic simulations compared to linear simulations overall. Therefore, the model can effectively predict the major THG characteristics of resonance wavelength and intensity for the random Si MS structures of pixelated contractible patterns in the unit cell, which facilitates the selection from the easy-to-fabricate Si MSs of given period and thickness for highly efficient output THG in specific wavelength ranges.

7.4 Conclusion and Outlook

We presented a CNN prediction method for THG resonance wavelengths and output intensities of a type of binary-pixel-patterned Si MSs of periodic contractible nano-resonators. The prediction accuracies for the THG resonance wavelengths and output intensities are ~ 0.7 and ~ 0.8 by dividing the datasets into three classes, respectively. The accuracies are moderately high that the effective classification method is promising for predictions of Si THG MSs of other unit cell dimensions, THG MSs based on plasmonic materials (e.g., Au and Ag) and/or other dielectric materials (e.g., Si_3N_4 and TiO_2), and MSs for other NL processes (e.g., SHG and FWM). While design customization of the NL MSs, including Kerr-type reconfigurable MSs, is time-consuming with conventional theoretical analysis and electromagnetic modeling, this strategy can potentially accelerate the process with expedited pattern filtration.

CHAPTER 8. EPILOGUE

8.1 Brief Summary of Contributions

In conclusion, this dissertation has successfully demonstrated a hybrid platform for wideband reconfigurable MMs. The platform is a collection of dynamic PCM-controlled devices and passive Si structures.

The first part of the platform is based on PCMs GST and Sb_2S_3 . A broadband-tunable subwavelength-scale THG device at the NIR fundamental wavelengths ranging over a 200 nm bandwidth with an asymmetric F-P cavity was numerically and experimentally demonstrated for the first time, based on both extreme and intermediate crystallinity states of the well-known PCM GST. It was extended to a numerical study of the THG band tunability of GST to a gap-SPR hybridized structure with both enhanced THG efficiency and an even wider tunability range. Intensity tunability of efficient SHG has been experimentally demonstrated with the same structure under realistic material and geometry considerations and compared with tunable SHG from a subwavelength-scale asymmetric F-P GST cavity. A high-Q Si MS of resonant nearfield responses modulated by a subwavelength F-P cavity incorporating GST has been designed, exhibiting large extinction ratios on the THG intensity in numerical and experimental demonstrations. The last study of dynamic PCM-controlled devices was a numerical demonstration of an all-dielectric linear and THG MS based on the low-loss PCM Sb_2S_3 that interchanges foci of the MS at a- Sb_2S_3 and c- Sb_2S_3 states for the FH and TH, respectively. These demonstrations of tunable frequency conversions are promising for applications such as harmonic-generation-based microscopy, imaging, and optical communications.

The second part of the platform is based on all-Si passive MSs. A type of novel bidirectional symmetry-broken MSs was numerically designed to exhibit a quasi-BIC resonance with $Q \sim 10^5$ for ultra-large field enhancement in the meta-atoms, expecting efficient THG. Optical Kerr effect has been observed and used in efficient THG (demonstrated experimentally) from the MSs, which paves the way for quasi-BIC design modifications for computing applications of all-optical switchable harmonic generation. The other work of the passive part of the platform was the demonstration of a prediction method for resonant THG characteristics of random contractible binary-pixel-patterned MSs of specific unit-cell dimensions, without NL electromagnetic simulations that are time-consuming. The unit-cell dimensions were selected for possible MS patterns to exhibit quasi-BIC. An inferred THG resonance wavelength from the linear simulation and the THG output intensity of the NL simulation at the inferred resonance wavelength for each MS pattern were labeled by the range and the level, respectively. Moderately high prediction accuracies have been achieved with an image-classification-targeted CNN, which can potentially be extended to implementations for the efficient selection of highly NL quasi-BIC MSs for all-optical switching and computing.

8.2 Future Directions

8.2.1 Optimization of Fabrication Processes

The experimentally measured nonlinear performance of the GST-based nanostructures is degraded due to their immediate exposure to air during transfer of intermediate samples between deposition tools in the fabrication processes. This is especially a major reason that THG signals from the structure in Figure 15(a) of Section

3.2.2 were not detected. Using an in-situ transfer process between the depositions to keep the intermediate samples in vacuum during the transfer can be a potential solution to the oxidation problem. The Chalcogenide Materials Sputterer could be connected to an e-beam evaporator for physical vapor deposition [214] of materials not to cover vertical sidewalls of the structure, an ALD tool for uniform deposition of ultrathin high-quality material layers, and a PECVD tool for uniform deposition of thicker material layers that do not require qualities as high as those deposited by ALD, through vacuum pressure transition channels.

The samples for the structure in Figure 15(a) are impacted by multiple fabrication imperfections. The shadowing effect in Au deposition mentioned at the end of Section 3.2.2 can be reduced by testing different settings of the e-beam evaporation (e.g., distances between the intermediate sample and the evaporation source, e-beam sweeping patterns). Besides the GST oxidation issue and the shadowing effect in Au deposition mentioned at the end of Section 3.2.2, possible coverage of GST on the sidewalls of developed e-beam resist is an undesired issue (also indicated by that the slightly larger radii of GST nano-disks than those of the Au nano-disks as seen in Figure 15(e)). Similar to the evaporation of Au, the sidewall coverage of GST can be possibly reduced by optimizing the settings of the sputtering process (e.g., the distance between the intermediate sample and the sputtering target, electric fields to the target and substrate holder).

Additionally, I observed substantial deformation of remnant HSQ in Figure 27 of Section 4.3.1 and Figure 33 of Section 6.2.2. This indicates room for improvement in pre-EBL processing, post-EBL processing, and development process of the HSQ resist. Lastly, the structure in Figure 29(a) of Section 5.2 was not fabricated due to immature processing

techniques of Sb_2S_3 . Fabrication of the device is expected in the future. All the perspectives in this section for fabrication process optimization also apply to potential extensions of the hybrid platform for wideband reconfigurable MMs.

8.2.2 *Expansion to More NL Processes*

Parametric processes in optics are light-matter interactions in which initial and final quantum-mechanical states (e.g., energy, momentum, angular momentum) of the material system are identical [92]. Besides SHG, THG, and the optical Kerr effect focused in the studies of this thesis, HHG, sum-frequency generation (SFG), difference-frequency generation (DFG), and FWM are also typical NL parametric processes [92]. Input lights of different frequencies are mixed in SFG, DFG, and FWM. Conversely, non-parametric NL processes involve different initial and final quantum-mechanical states, such as TPA and TPL.

The hybrid platform in this thesis can be potentially extended to the other NL parametric processes. Reconfigurable HHG is extremely challenging to be realized with phase-change chalcogenides like GST and Sb_2S_3 due to very high pump power requirements that could always crystallize the phase-change chalcogenides. And there is an experimental demonstration of efficient HHG from an all-Si MS [102]. Thus, the all-Si MS structures of large in-Si nearfield enhancement in this dissertation have a higher potential for HHG reconfiguration. The structures in Section 3.2 demonstrated significant SHG, especially for that in Figure 15(a) exhibiting resonances at different wavelength bands (see Figure 17(a) and Figure 17(c)). These structures can possibly be used for other second-order parametric processes like SFG and DFG. Other structures demonstrated in

this thesis, except for the structure in Section 5.2, have the potential for reconfigurable FWM, especially for input lights of similar frequencies located within the resonance band. Moreover, FWM with both input and output lights in the NIR wavelength range [103] can be more efficient than THG with λ_f in the NIR and λ_{TH} in the visible wavelength range, due to lower optical losses in the materials at the NIR than at the visible wavelengths.

The hybrid platform can also be extended to the non-parametric NL processes. Since the high-index materials in this thesis generally exhibit bandgaps smaller than the total energy of two NIR photons, I deem the structures demonstrated in this thesis with linear $Qs > 10$ (e.g., the structures in Figure 12(a) of Section 3.1.1, Figure 15(a) of Section 3.2.2, as well as Figure 31(a) and Figure 31(b) of Section 6.2.2) can be promising for TPA reconfigurations due to relatively large resonant nearfields within the NL media. The structure in Figure 15(b) has shown substantial TPL tunability in Figure 18(c) with the GST phase change. This can pave the way for investigations of TPL reconfiguration with more sophisticated PCM-based nanostructures.

All the perspectives in this section for extensions to more NL processes also apply to possible extended reconfigurable hybrid MM platforms in terms of operation wavelength ranges, materials, and device structures.

8.2.3 *Imaging and Holography Applications*

In addition to NL optical switches for potential communication applications and the optical Kerr effect for potential computing applications, the hybrid platform is promising for applications of dynamic imaging and reconfigurable holography. Recently, Schlickriede *et al.* theoretically and experimentally demonstrated THG imaging of higher-

order spatial correlations (i.e., higher resolutions) than linear imaging, by employing an all-dielectric metalens composed of Si nanopillars [16]. The higher-order spatial correlations are due to the relation $I(3\omega) \propto I(\omega)^3$, where $I(3\omega)$ and $I(\omega)$ are local optical intensities within the nanopillars at the FH and TH, respectively. A similar principle applies to high-resolution SHG imaging [74]. The Sb_2S_3 structure in Figure 29(a) of Section 5.2 can be evolved to 2D-focusing for dynamic high-resolution THG imaging. GST-based dielectric MSs have the potential for dynamic high-resolution SHG imaging at longer infrared wavelengths than those in Section 3.2, given the $\chi^{(2)}$ tunability and reduced optical loss of orderly structured GST.

Frequency conversion holography has an advantage over its linear counterparts by encoding information to another frequency. Gao *et al.* numerically designed and experimentally demonstrated high-efficiency cyan and blue THG holograms with all-dielectric MSs composed of C-shaped Si nano-antennas, by introducing full-range optical phase changes from 0 to 2π to the C elements [28]. Optical phase changes from 0 to only $2\pi/3$ are needed to be introduced by the nano-antennas for the linear regime. This greatly reduces the difficulty in designing the nano-antennas. Thus, it could be potentially applied to Sb_2S_3 meta-atoms and GST meta-atoms at longer infrared wavelengths. The perspective sheds light on the design of reconfigurable MSs for THG holography.

REFERENCES

- [1] C. M. Soukoulis and M. Wegener, "Past achievements and future challenges in the development of three-dimensional photonic metamaterials," *Nature Photonics* **5**, 523-530 (2011).
- [2] N. I. Zheludev and Y. S. Kivshar, "From metamaterials to metadevices," *Nature Materials* **11**, 917-924 (2012).
- [3] G. Li, S. Zhang, and T. Zentgraf, "Nonlinear photonic metasurfaces," *Nature Reviews Materials* **2**, 17010 (2017).
- [4] T. Pertsch and Y. Kivshar, "Nonlinear optics with resonant metasurfaces," *MRS Bulletin* **45**, 210-220 (2020).
- [5] Q. Wei, L. Huang, T. Zentgraf, and Y. Wang, "Optical wavefront shaping based on functional metasurfaces," *Nanophotonics* **9**, 987-1002 (2020).
- [6] W. Cai, U. K. Chettiar, A. V. Kildishev, and V. M. Shalaev, "Optical cloaking with metamaterials," *Nature Photonics* **1**, 224-227 (2007).
- [7] Y. Lee, S.-J. Kim, H. Park, and B. Lee, "Metamaterials and metasurfaces for sensor applications," *Sensors* **17**, 1726 (2017).
- [8] J. Garcia-Guirado, M. Svedendahl, J. Puigdollers, and R. Quidant, "Enhanced chiral sensing with dielectric nanoresonators," *Nano Letters* **20**, 585-591 (2019).
- [9] Y. Yang, W. Wang, P. Moitra, I. I. Kravchenko, D. P. Briggs, and J. Valentine, "Dielectric meta-reflectarray for broadband linear polarization conversion and optical vortex generation," *Nano Letters* **14**, 1394-1399 (2014).
- [10] P. Genevet and F. Capasso, "Holographic optical metasurfaces: a review of current progress," *Reports on Progress in Physics* **78**, 024401 (2015).
- [11] N. C. Pégard and J. W. Fleischer, "Optimizing holographic data storage using a fractional Fourier transform," *Optics Letters* **36**, 2551-2553 (2011).
- [12] M. Khorasaninejad, W. T. Chen, R. C. Devlin, J. Oh, A. Y. Zhu, and F. Capasso, "Metalenses at visible wavelengths: Diffraction-limited focusing and subwavelength resolution imaging," *Science* **352**, 1190-1194 (2016).
- [13] Q. Wang, E. T. Rogers, B. Gholipour, C.-M. Wang, G. Yuan, J. Teng, and N. I. Zheludev, "Optically reconfigurable metasurfaces and photonic devices based on phase change materials," *Nature Photonics* **10**, 60-65 (2016).

- [14] L. Jin, Z. Dong, S. Mei, Y. F. Yu, Z. Wei, Z. Pan, S. D. Rezaei, X. Li, A. I. Kuznetsov, and Y. S. Kivshar, "Noninterleaved metasurface for (2^6-1) spin-and wavelength-encoded holograms," *Nano Letters* **18**, 8016-8024 (2018).
- [15] A. E. Minovich, A. E. Miroshnichenko, A. Y. Bykov, T. V. Murzina, D. N. Neshev, and Y. S. Kivshar, "Functional and nonlinear optical metasurfaces," *Laser & Photonics Reviews* **9**, 195-213 (2015).
- [16] C. Schlickriede, S. S. Kruk, L. Wang, B. Sain, Y. Kivshar, and T. Zentgraf, "Nonlinear imaging with all-dielectric metasurfaces," *Nano Letters* **20**, 4370-4376 (2020).
- [17] A. I. Kuznetsov, A. E. Miroshnichenko, M. L. Brongersma, Y. S. Kivshar, and B. Luk'yanchuk, "Optically resonant dielectric nanostructures," *Science* **354**, aag2472 (2016).
- [18] I. Staude and J. Schilling, "Metamaterial-inspired silicon nanophotonics," *Nature Photonics* **11**, 274-284 (2017).
- [19] M. F. Limonov, M. V. Rybin, A. N. Poddubny, and Y. S. Kivshar, "Fano resonances in photonics," *Nature Photonics* **11**, 543-554 (2017).
- [20] K. Koshelev, G. Favraud, A. Bogdanov, Y. Kivshar, and A. Fratalocchi, "Nonradiating photonics with resonant dielectric nanostructures," *Nanophotonics* **8**, 725-745 (2019).
- [21] K. Koshelev, S. Lepeshov, M. Liu, A. Bogdanov, and Y. Kivshar, "Asymmetric metasurfaces with high-Q resonances governed by bound states in the continuum," *Physical Review Letters* **121**, 193903 (2018).
- [22] K. Koshelev, S. Kruk, E. Melik-Gaykazyan, J.-H. Choi, A. Bogdanov, H.-G. Park, and Y. Kivshar, "Subwavelength dielectric resonators for nonlinear nanophotonics," *Science* **367**, 288-292 (2020).
- [23] Y. Yang, I. I. Kravchenko, D. P. Briggs, and J. Valentine, "All-dielectric metasurface analogue of electromagnetically induced transparency," *Nature Communications* **5**, 5753 (2014).
- [24] P. A. Jeong, M. D. Goldflam, S. Campione, J. L. Briscoe, P. P. Vabishchevich, J. Nogan, M. B. Sinclair, T. S. Luk, and I. Brener, "High Quality Factor Toroidal Resonances in Dielectric Metasurfaces," *ACS Photonics* **7**, 1699-1707 (2020).
- [25] K. Koshelev, A. Bogdanov, and Y. Kivshar, "Meta-optics and bound states in the continuum," *Science Bulletin* **64**, 836-842 (2019).
- [26] Z. Liu, Y. Xu, Y. Lin, J. Xiang, T. Feng, Q. Cao, J. Li, S. Lan, and J. Liu, "High-Q quasibound states in the continuum for nonlinear metasurfaces," *Physical Review Letters* **123**, 253901 (2019).

- [27] M. R. Shcherbakov, P. P. Vabishchevich, A. S. Shorokhov, K. E. Chong, D.-Y. Choi, I. Staude, A. E. Miroshnichenko, D. N. Neshev, A. A. Fedyanin, and Y. S. Kivshar, "Ultrafast all-optical switching with magnetic resonances in nonlinear dielectric nanostructures," *Nano Letters* **15**, 6985-6990 (2015).
- [28] Y. Gao, Y. Fan, Y. Wang, W. Yang, Q. Song, and S. Xiao, "Nonlinear holographic all-dielectric metasurfaces," *Nano Letters* **18**, 8054-8061 (2018).
- [29] M. Esmaeili-Rad, A. Sazonov, A. Kazanskii, A. Khomich, and A. Nathan, "Optical properties of nanocrystalline silicon deposited by PECVD," *Journal of Materials Science: Materials in Electronics* **18**, 405-409 (2007).
- [30] J. Yang and J. A. Fan, "Analysis of material selection on dielectric metasurface performance," *Optics Express* **25**, 23899-23909 (2017).
- [31] D. Sell, J. Yang, S. Doshay, K. Zhang, and J. A. Fan, "Visible light metasurfaces based on single-crystal silicon," *ACS Photonics* **3**, 1919-1925 (2016).
- [32] S. Liu, G. A. Keeler, J. L. Reno, M. B. Sinclair, and I. Brener, "III–V semiconductor nanoresonators—A new strategy for passive, active, and nonlinear all-dielectric metamaterials," *Advanced Optical Materials* **4**, 1457-1462 (2016).
- [33] P. C. Wu, R. A. Pala, G. K. Shirmanesh, W.-H. Cheng, R. Sokhoyan, M. Grajower, M. Z. Alam, D. Lee, and H. A. Atwater, "Dynamic beam steering with all-dielectric electro-optic III–V multiple-quantum-well metasurfaces," *Nature Communications* **10**, 3654 (2019).
- [34] S. Liu, A. Vaskin, S. Addamane, B. Leung, M.-C. Tsai, Y. Yang, P. P. Vabishchevich, G. A. Keeler, G. Wang, X. He, Y. Kim, N. F. Hartmann, H. Htoon, S. K. Doorn, M. Zilk, T. Pertsch, G. Balakrishnan, M. B. Sinclair, I. Staude, and I. Brener, "Light-emitting metasurfaces: simultaneous control of spontaneous emission and far-field radiation," *Nano Letters* **18**, 6906-6914 (2018).
- [35] Y. Bao, Q. Lin, R. Su, Z.-K. Zhou, J. Song, J. Li, and X.-H. Wang, "On-demand spin-state manipulation of single-photon emission from quantum dot integrated with metasurface," *Science Advances* **6**, eaba8761 (2020).
- [36] B. H. Chen, P. C. Wu, V.-C. Su, Y.-C. Lai, C. H. Chu, I. C. Lee, J.-W. Chen, Y. H. Chen, Y.-C. Lan, C.-H. Kuan, and D. P. Tsai, "GaN metalens for pixel-level full-color routing at visible light," *Nano Letters* **17**, 6345-6352 (2017).
- [37] A. Zhan, S. Colburn, R. Trivedi, T. K. Fryett, C. M. Dodson, and A. Majumdar, "Low-contrast dielectric metasurface optics," *ACS Photonics* **3**, 209-214 (2016).
- [38] O. Hemmatyar, S. Abdollahramezani, Y. Kiarashinejad, M. Zandehshahvar, and A. Adibi, "Full color generation with fano-type resonant HfO₂ nanopillars designed by a deep-learning approach," *Nanoscale* **11**, 21266-21274 (2019).

- [39] Y. Che, X. Wang, Q. Song, Y. Zhu, and S. Xiao, "Tunable optical metasurfaces enabled by multiple modulation mechanisms," *Nanophotonics* **9**, 4407-4431 (2020).
- [40] L. Kang, R. P. Jenkins, and D. H. Werner, "Recent progress in active optical metasurfaces," *Advanced Optical Materials* **7**, 1801813 (2019).
- [41] W. Dong, H. Liu, J. K. Behera, L. Lu, R. J. Ng, K. V. Sreekanth, X. Zhou, J. K. Yang, and R. E. Simpson, "Wide bandgap phase change material tuned visible photonics," *Advanced Functional Materials* **29**, 1806181 (2019).
- [42] S. Abdollahramezani, O. Hemmatyar, H. Taghinejad, A. Krasnok, Y. Kiarashinejad, M. Zandehshahvar, A. Alù, and A. Adibi, "Tunable nanophotonics enabled by chalcogenide phase-change materials," *Nanophotonics* **9**, 1189-1241 (2020).
- [43] J. Zheng, Z. Fang, C. Wu, S. Zhu, P. Xu, J. K. Doylend, S. Deshmukh, E. Pop, S. Dunham, M. Li, and A. Majumdar, "Nonvolatile electrically reconfigurable integrated photonic switch enabled by a silicon PIN diode heater," *Advanced Materials* **32**, 2001218 (2020).
- [44] K. Dong, S. Hong, Y. Deng, H. Ma, J. Li, X. Wang, J. Yeo, L. Wang, S. Lou, K. B. Tom, K. Liu, Z. You, Y. Wei, C. P. Grigoropoulos, J. Yao, and J. Wu, "A Lithography-Free and Field-Programmable Photonic Metacanvas," *Advanced Materials* **30**, 1703878 (2018).
- [45] Y. Chen, X. Duan, M. Matuschek, Y. Zhou, F. Neubrech, H. Duan, and N. Liu, "Dynamic color displays using stepwise cavity resonators," *Nano Letters* **17**, 5555-5560 (2017).
- [46] H. Gehan, C. Mangeney, J. Aubard, G. Lévi, A. Hohenau, J. R. Krenn, E. Lacaze, and N. Féridj, "Design and optical properties of active polymer-coated plasmonic nanostructures," *The Journal of Physical Chemistry Letters* **2**, 926-931 (2011).
- [47] S. Song, X. Ma, M. Pu, X. Li, K. Liu, P. Gao, Z. Zhao, Y. Wang, C. Wang, and X. Luo, "Actively tunable structural color rendering with tensile substrate," *Advanced Optical Materials* **5**, 1600829 (2017).
- [48] Y. Fang, Y. Ni, S.-Y. Leo, C. Taylor, V. Basile, and P. Jiang, "Reconfigurable photonic crystals enabled by pressure-responsive shape-memory polymers," *Nature Communications* **6**, 7416 (2015).
- [49] E. Arbabi, A. Arbabi, S. M. Kamali, Y. Horie, M. Faraji-Dana, and A. Faraon, "MEMS-tunable dielectric metasurface lens," *Nature Communications* **9**, 812 (2018).
- [50] M. A. Kats, D. Sharma, J. Lin, P. Genevet, R. Blanchard, Z. Yang, M. M. Qazilbash, D. Basov, S. Ramanathan, and F. Capasso, "Ultra-thin perfect absorber

- employing a tunable phase change material," *Applied Physics Letters* **101**, 221101 (2012).
- [51] B. J. Eggleton, B. Luther-Davies, and K. Richardson, "Chalcogenide photonics," *Nature Photonics* **5**, 141-148 (2011).
 - [52] M. Wuttig, H. Bhaskaran, and T. Taubner, "Phase-change materials for non-volatile photonic applications," *Nature Photonics* **11**, 465-476 (2017).
 - [53] J. Kalb, M. Wuttig, and F. Spaepen, "Calorimetric measurements of structural relaxation and glass transition temperatures in sputtered films of amorphous Te alloys used for phase change recording," *Journal of Materials Research* **22**, 748-754 (2007).
 - [54] I. S. Kim, S. L. Cho, D. H. Im, E. H. Cho, D. H. Kim, G. H. Oh, D. H. Ahn, S. O. Park, S. W. Nam, J. T. Moon, and C. H. Chung, "High Performance PRAM Cell Scalable to sub-20nm technology with below 4F(2) Cell Size, Extendable to DRAM Applications," in *Symposium on VLSI Technology* (IEEE, 2010), pp. 203–204.
 - [55] S. Abdollahramezani, H. Taghinejad, T. Fan, M. R. Marzban, A. A. Eftekhari, and A. Adibi, "Reconfigurable multifunctional metasurfaces employing hybrid phase-change plasmonic architecture," *Nanophotonics* **11**, 3883-3893 (2022).
 - [56] M. Delaney, I. Zeimpekis, D. Lawson, D. W. Hewak, and O. L. Muskens, "A New Family of Ultralow Loss Reversible Phase-Change Materials for Photonic Integrated Circuits: Sb₂S₃ and Sb₂Se₃," *Advanced Functional Materials* **30**, 2002447 (2020).
 - [57] K. C. Gödel, B. Roose, A. Sadhanala, Y. Vaynzof, S. K. Pathak, and U. Steiner, "Partial oxidation of the absorber layer reduces charge carrier recombination in antimony sulfide solar cells," *Physical Chemistry Chemical Physics* **19**, 1425-1430 (2017).
 - [58] Y. Kim, P. C. Wu, R. Sokhoyan, K. Mauser, R. Glaudell, G. Kafaie Shirmanesh, and H. A. Atwater, "Phase modulation with electrically tunable vanadium dioxide phase-change metasurfaces," *Nano Letters* **19**, 3961-3968 (2019).
 - [59] S. Abdollahramezani, O. Hemmatyar, M. Taghinejad, H. Taghinejad, Y. Kiarashinejad, M. Zandehshahvar, T. Fan, S. Deshmukh, A. A. Eftekhari, W. Cai, E. Pop, M. El-Sayed, and A. Adibi, "Dynamic hybrid metasurfaces," *Nano Letters* **21**, 1238-1245 (2021).
 - [60] S.-Y. Lee, Y.-H. Kim, S.-M. Cho, G. H. Kim, T.-Y. Kim, H. Ryu, H. N. Kim, H. B. Kang, C.-Y. Hwang, and C.-S. Hwang, "Holographic image generation with a thin-film resonance caused by chalcogenide phase-change material," *Scientific Reports* **7**, 41152 (2017).

- [61] C. R. de Galarreta, I. Sinev, A. M. Alexeev, P. Trofimov, K. Ladutenko, S. G.-C. Carrillo, E. Gemo, A. Baldycheva, J. Bertolotti, and C. D. Wright, "Reconfigurable multilevel control of hybrid all-dielectric phase-change metasurfaces," *Optica* **7**, 476-484 (2020).
- [62] K. V. Sreekanth, Q. Ouyang, S. Sreejith, S. Zeng, W. Lishu, E. Ilker, W. Dong, M. ElKabbash, Y. Ting, C. T. Lim, M. Hinczewski, G. Strangi, K.-T. Yong, R. E. Simpson, and R. Singh, "Phase-Change-Material-Based Low-Loss Visible-Frequency Hyperbolic Metamaterials for Ultrasensitive Label-Free Biosensing," *Advanced Optical Materials* **7**, 1900081 (2019).
- [63] R. C. Miller, "Optical second harmonic generation in piezoelectric crystals," *Applied Physics Letters* **5**, 17-19 (1964).
- [64] S.-N. Zhu, Y.-Y. Zhu, and N.-B. Ming, "Quasi-phase-matched third-harmonic generation in a quasi-periodic optical superlattice," *Science* **278**, 843-846 (1997).
- [65] R. Stolen and A. Ashkin, "Optical Kerr effect in glass waveguide," *Applied Physics Letters* **22**, 294-296 (1973).
- [66] E. W. Van Stryland, H. Vanherzeele, M. A. Woodall, M. Soileau, A. L. Smirl, S. Guha, and T. F. Boggess, "Two photon absorption, nonlinear refraction, and optical limiting in semiconductors," *Optical Engineering* **24**, 244613 (1985).
- [67] E. Y. Glushko, "All-optical signal processing in photonic structures with nonlinearity," *Optics Communications* **247**, 275-280 (2005).
- [68] R. W. Eason and A. Miller, *Nonlinear Optics in Signal Processing* (Springer Science & Business Media, 2012).
- [69] M. A. Petruska, A. V. Malko, P. M. Voyles, and V. I. Klimov, "High - performance, quantum dot nanocomposites for nonlinear optical and optical gain applications," *Advanced Materials* **15**, 610-613 (2003).
- [70] S. Ma, W. Li, H. Hu, and N. K. Dutta, "High speed ultra short pulse fiber ring laser using photonic crystal fiber nonlinear optical loop mirror," *Optics Communications* **285**, 2832-2835 (2012).
- [71] S. Friberg and P. Smith, "Nonlinear optical glasses for ultrafast optical switches," *IEEE Journal of Quantum Electronics* **23**, 2089-2094 (1987).
- [72] P. C. Ray, "Size and shape dependent second order nonlinear optical properties of nanomaterials and their application in biological and chemical sensing," *Chemical Reviews* **110**, 5332-5365 (2010).
- [73] B. Champagne, A. I. Plaquet, J.-L. Pozzo, V. Rodriguez, and F. Castet, "Nonlinear optical molecular switches as selective cation sensors," *Journal of the American Chemical Society* **134**, 8101-8103 (2012).

- [74] P. J. Campagnola, A. Lewis, and L. M. Loew, "High-resolution nonlinear optical imaging of live cells by second harmonic generation," *Biophysical Journal* **77**, 3341-3349 (1999).
- [75] W. Min, C. W. Freudiger, S. Lu, and X. S. Xie, "Coherent nonlinear optical imaging: beyond fluorescence microscopy," *Annual Review of Physical Chemistry* **62**, 507-530 (2011).
- [76] A. Krasnok, M. Tymchenko, and A. Alù, "Nonlinear metasurfaces: a paradigm shift in nonlinear optics," *Materials Today* **21**, 8-21 (2018).
- [77] W. Cai, A. P. Vasudev, and M. L. Brongersma, "Electrically controlled nonlinear generation of light with plasmonics," *Science* **333**, 1720-1723 (2011).
- [78] J. Y. Ou, E. Plum, J. Zhang, and N. I. Zheludev, "Giant nonlinearity of an optically reconfigurable plasmonic metamaterial," *Advanced Materials* **28**, 729-733 (2016).
- [79] D. Pacifici, H. J. Lezec, and H. A. Atwater, "All-optical modulation by plasmonic excitation of CdSe quantum dots," *Nature Photonics* **1**, 402-406 (2007).
- [80] M. Taghinejad, H. Taghinejad, Z. Xu, Y. Liu, S. P. Rodrigues, K. T. Lee, T. Lian, A. Adibi, and W. Cai, "Hot-Electron-Assisted Femtosecond All-Optical Modulation in Plasmonics," *Advanced Materials* **30**, 1704915 (2018).
- [81] J. Wang, K. Jin, H. Yao, J. Gu, X. Xu, C. Ge, C. Wang, M. He, and G. Yang, "Temperature-dependent phase transition in barium titanate crystals probed by second harmonic generation," *Applied Physics Letters* **112**, 102904 (2018).
- [82] J. Zhang, K. F. MacDonald, and N. I. Zheludev, "Nonlinear dielectric optomechanical metamaterials," *Light: Science & Applications* **2**, e96 (2013).
- [83] S. Lan, S. Rodrigues, Y. Cui, L. Kang, and W. Cai, "Electrically tunable harmonic generation of light from plasmonic structures in electrolytes," *Nano Letters* **16**, 5074-5079 (2016).
- [84] Y.-W. Huang, H. W. H. Lee, R. Sokhoyan, R. A. Pala, K. Thyagarajan, S. Han, D. P. Tsai, and H. A. Atwater, "Gate-tunable conducting oxide metasurfaces," *Nano Letters* **16**, 5319-5325 (2016).
- [85] D. A. Smirnova, A. E. Miroshnichenko, Y. S. Kivshar, and A. B. Khanikaev, "Tunable nonlinear graphene metasurfaces," *Physical Review B* **92**, 161406 (2015).
- [86] M. R. Shcherbakov, S. Liu, V. V. Zubyuk, A. Vaskin, P. P. Vabishchevich, G. Keeler, T. Pertsch, T. V. Dolgova, I. Staude, I. Brener, and A. A. Fedyanin, "Ultrafast all-optical tuning of direct-gap semiconductor metasurfaces," *Nature Communications* **8**, 17 (2017).

- [87] T. Cao, K. Liu, Y. Tang, J. Deng, K. Li, and G. Li, "A High-Index $\text{Ge}_2\text{Sb}_2\text{Te}_5$ -Based Fabry–Perot Cavity and Its Application for Third-Harmonic Generation," *Laser & Photonics Reviews* **13**, 1900063 (2019).
- [88] F. Y. Yue, R. Piccoli, M. Y. Shalaginov, T. Gu, K. A. Richardson, R. Morandotti, J. J. Hu, and L. Razzari, "Nonlinear Mid-Infrared Metasurface based on a Phase-Change Material," *Laser & Photonics Reviews* **15**, 2000373 (2021).
- [89] Y. Zhang, J. B. Chou, J. Li, H. Li, Q. Du, A. Yadav, S. Zhou, M. Y. Shalaginov, Z. Fang, H. Zhong, C. Roberts, P. Robinson, B. Bohlin, C. Ríos, H. Lin, M. Kang, T. Gu, J. Warner, V. Liberman, K. Richardson, and J. Hu, "Broadband transparent optical phase change materials for high-performance nonvolatile photonics," *Nature Communications* **10**, 4279 (2019).
- [90] C. C. Wang, "Empirical relation between the linear and the third-order nonlinear optical susceptibilities," *Physical Review B* **2**, 2045-2048 (1970).
- [91] K. Koshelev and Y. Kivshar, "Dielectric resonant metaphotonics," *ACS Photonics* **8**, 102-112 (2020).
- [92] R. W. Boyd, *Nonlinear Optics* (Academic press, 2020).
- [93] M. W. Klein, C. Enkrich, M. Wegener, and S. Linden, "Second-harmonic generation from magnetic metamaterials," *Science* **313**, 502-504 (2006).
- [94] M. Semmlinger, M. L. Tseng, J. Yang, M. Zhang, C. Zhang, W.-Y. Tsai, D. P. Tsai, P. Nordlander, and N. J. Halas, "Vacuum ultraviolet light-generating metasurface," *Nano Letters* **18**, 5738-5743 (2018).
- [95] S. Liu, M. B. Sinclair, S. Saravi, G. A. Keeler, Y. Yang, J. Reno, G. M. Peake, F. Setzpfandt, I. Staude, T. Pertsch, and I. Brener "Resonantly enhanced second-harmonic generation using III–V semiconductor all-dielectric metasurfaces," *Nano Letters* **16**, 5426-5432 (2016).
- [96] D. Lehr, J. Reinhold, I. Thiele, H. Hartung, K. Dietrich, C. Menzel, T. Pertsch, E.-B. Kley, and A. Tünnermann, "Enhancing second harmonic generation in gold nanoring resonators filled with lithium niobate," *Nano Letters* **15**, 1025-1030 (2015).
- [97] J. Bar-David and U. Levy, "Nonlinear diffraction in asymmetric dielectric metasurfaces," *Nano Letters* **19**, 1044-1051 (2019).
- [98] L. Carletti, G. Marino, L. Ghirardini, V. F. Gili, D. Rocco, I. Favero, A. Locatelli, A. V. Zayats, M. Celebrano, M. Finazzi, G. Leo, C. D. Angelis, and D.N. Neshev, "Nonlinear goniometry by second-harmonic generation in AlGaAs nanoantennas," *ACS Photonics* **5**, 4386-4392 (2018).

- [99] M. R. Shcherbakov, D. N. Neshev, B. Hopkins, A. S. Shorokhov, I. Staude, E. V. Melik-Gaykazyan, M. Decker, A. A. Ezhov, A. E. Miroschnichenko, I. Brener, A. A. Fedyanin, and Y. S. Kivshar, "Enhanced third-harmonic generation in silicon nanoparticles driven by magnetic response," *Nano Letters* **14**, 6488-6492 (2014).
- [100] T. Shibanuma, G. Grinblat, P. Albella, and S. A. Maier, "Efficient third harmonic generation from metal-dielectric hybrid nanoantennas," *Nano Letters* **17**, 2647-2651 (2017).
- [101] Y. Yang, W. Wang, A. Boulesbaa, I. I. Kravchenko, D. P. Briggs, A. Puretzky, D. Geohagan, and J. Valentine, "Nonlinear Fano-resonant dielectric metasurfaces," *Nano Letters* **15**, 7388-7393 (2015).
- [102] H. Liu, C. Guo, G. Vampa, J. L. Zhang, T. Sarmiento, M. Xiao, P. H. Bucksbaum, J. Vučković, S. Fan, and D. A. Reis, "Enhanced high-harmonic generation from an all-dielectric metasurface," *Nature Physics* **14**, 1006-1010 (2018).
- [103] S. Liu, P. P. Vabishchevich, A. Vaskin, J. L. Reno, G. A. Keeler, M. B. Sinclair, I. Staude, and I. Brener, "An all-dielectric metasurface as a broadband optical frequency mixer," *Nature communications* **9**, 2507 (2018).
- [104] M. R. Shcherbakov, H. Zhang, M. Tripepi, G. Sartorello, N. Talisa, A. AlShafey, Z. Fan, J. Twardowski, L. A. Krivitsky, A. I. Kuznetsov, E. Chowdhury, and G. Shvets, "Generation of even and odd high harmonics in resonant metasurfaces using single and multiple ultra-intense laser pulses," *Nature Communications* **12**, 4185 (2021).
- [105] C. Brée, A. Demircan, and G. Steinmeyer, "Saturation of the all-optical Kerr effect," *Physical Review Letters* **106**, 183902 (2011).
- [106] A. Feldman, D. Horowitz, and R. Waxler, "Mechanisms for self-focusing in optical glasses," *IEEE Journal of Quantum Electronics* **9**, 1054-1061 (1973).
- [107] Z. Chai, X. Hu, F. Wang, X. Niu, J. Xie, and Q. Gong, "Ultrafast all-optical switching," *Advanced Optical Materials* **5**, 1600665 (2017).
- [108] G. Della Valle, D. Polli, P. Biagioni, C. Martella, M. Giordano, M. Finazzi, S. Longhi, L. Duo, G. Cerullo, and F. B. de Mongeot, "Self-organized plasmonic metasurfaces for all-optical modulation," *Physical Review B* **91**, 235440 (2015).
- [109] G. Grinblat, H. Zhang, M. P. Nielsen, L. Krivitsky, R. Berté, Y. Li, B. Tilmann, E. Cortés, R. F. Oulton, A. I. Kuznetsov, and S. A. Maier, "Efficient ultrafast all-optical modulation in a nonlinear crystalline gallium phosphide nanodisk at the anapole excitation," *Science Advances* **6**, eabb3123 (2020).
- [110] M. Kauranen and A. V. Zayats, "Nonlinear plasmonics," *Nature Photonics* **6**, 737-748 (2012).

- [111] M. Taghinejad, H. Taghinejad, Z. Xu, K.-T. Lee, S. P. Rodrigues, J. Yan, A. Adibi, T. Lian, and W. Cai, "Ultrafast control of phase and polarization of light expedited by hot-electron transfer," *Nano Letters* **18**, 5544-5551 (2018).
- [112] B. Jin and C. Argyropoulos, "Self-induced passive nonreciprocal transmission by nonlinear bifacial dielectric metasurfaces," *Physical Review Applied* **13**, 054056 (2020).
- [113] M. Silveirinha and N. Engheta, "Tunneling of electromagnetic energy through subwavelength channels and bends using ϵ -near-zero materials," *Physical Review Letters* **97**, 157403 (2006).
- [114] J. Wang, A. Coillet, O. Demichel, Z. Wang, D. Rego, A. Bouhelier, P. Grelu, and B. Cluzel, "Saturable plasmonic metasurfaces for laser mode locking," *Light: Science & Applications* **9**, 50 (2020).
- [115] V. V. Zubyuk, P. P. Vabishchevich, M. R. Shcherbakov, A. S. Shorokhov, A. N. Fedotova, S. Liu, G. Keeler, T. V. Dolgova, I. Staude, and I. Brener, A. A. Fedyanin, "Low-Power Absorption Saturation in Semiconductor Metasurfaces," *ACS Photonics* **6**, 2797-2806 (2019).
- [116] F. Wang, A. B. Martinson, and H. Harutyunyan, "Efficient nonlinear metasurface based on nonplanar plasmonic nanocavities," *ACS Photonics* **4**, 1188-1194 (2017).
- [117] W.-S. Zhao, R. Zhang, and D.-W. Wang, "Recent Progress in Physics-Based Modeling of Electromigration in Integrated Circuit Interconnects," *Micromachines* **13**, 883 (2022).
- [118] R. Zhang, Z. Liu, K. Yang, T. Liu, W. Cai, and L. Milor, "A library based on deep neural networks for modeling the degradation of FinFET SRAM performance metrics due to aging," *Microelectronics Reliability* **100**, 113486 (2019).
- [119] R. Zhang, Z. Liu, K. Yang, T. Liu, W. Cai, and L. Milor, "Inverse design of finFET SRAM cells," in *2020 IEEE International Reliability Physics Symposium (IRPS)*, (IEEE, 2020), 1-6.
- [120] A. M. Hammond and R. M. Camacho, "Designing integrated photonic devices using artificial neural networks," *Optics Express* **27**, 29620-29638 (2019).
- [121] D. Zibar, A. M. R. Brusin, U. C. de Moura, F. Da Ros, V. Curri, and A. Carena, "Inverse system design using machine learning: the Raman amplifier case," *Journal of Lightwave Technology* **38**, 736-753 (2019).
- [122] M. K. Chen, X. Liu, Y. Sun, and D. P. Tsai, "Artificial Intelligence in Meta-optics," *Chemical Reviews* **122**, 15356-15413 (2022).
- [123] Z. Liu, D. Zhu, L. Raju, and W. Cai, "Tackling photonic inverse design with machine learning," *Advanced Science* **8**, 2002923 (2021).

- [124] M. Zandehshahvar, Y. Kiarashinejad, M. Zhu, H. Maleki, T. Brown, and A. Adibi, "Manifold learning for knowledge discovery and intelligent inverse design of photonic nanostructures: breaking the geometric complexity," *ACS Photonics* **9**, 714-721 (2022).
- [125] Y. Kiarashinejad, S. Abdollahramezani, M. Zandehshahvar, O. Hemmatyar, and A. Adibi, "Deep learning reveals underlying physics of light-matter interactions in nanophotonic devices," *Advanced Theory and Simulations* **2**, 1900088 (2019).
- [126] Y. Kiarashinejad, S. Abdollahramezani, and A. Adibi, "Deep learning approach based on dimensionality reduction for designing electromagnetic nanostructures," *npj Computational Materials* **6**, 12 (2020).
- [127] I. Malkiel, M. Mrejen, A. Nagler, U. Arieli, L. Wolf, and H. Suchowski, "Plasmonic nanostructure design and characterization via deep learning," *Light: Science & Applications* **7**, 60 (2018).
- [128] W. Ma, F. Cheng, and Y. Liu, "Deep-learning-enabled on-demand design of chiral metamaterials," *ACS Nano* **12**, 6326-6334 (2018).
- [129] Q. Zhang, C. Liu, X. Wan, L. Zhang, S. Liu, Y. Yang, and T. J. Cui, "Machine-learning designs of anisotropic digital coding metasurfaces," *Advanced Theory and Simulations* **2**, 1800132 (2019).
- [130] R. Lin, Y. Zhai, C. Xiong, and X. Li, "Inverse design of plasmonic metasurfaces by convolutional neural network," *Optics Letters* **45**, 1362-1365 (2020).
- [131] Z. Liu, D. Zhu, S. P. Rodrigues, K.-T. Lee, and W. Cai, "Generative model for the inverse design of metasurfaces," *Nano Letters* **18**, 6570-6576 (2018).
- [132] S. So and J. Rho, "Designing nanophotonic structures using conditional deep convolutional generative adversarial networks," *Nanophotonics* **8**, 1255-1261 (2019).
- [133] W. Ma, F. Cheng, Y. Xu, Q. Wen, and Y. Liu, "Probabilistic representation and inverse design of metamaterials based on a deep generative model with semi-supervised learning strategy," *Advanced Materials* **31**, 1901111 (2019).
- [134] L. Raju, K.-T. Lee, Z. Liu, D. Zhu, M. Zhu, E. Poutrina, A. Urbas, and W. Cai, "Maximized Frequency Doubling through the Inverse Design of Nonlinear Metamaterials," *ACS Nano* **16**, 3926-3933 (2022).
- [135] J. Gu, Z. Wang, J. Kuen, L. Ma, A. Shahroudy, B. Shuai, T. Liu, X. Wang, G. Wang, J. Cai, and T. Chen, "Recent advances in convolutional neural networks," *Pattern Recognition* **77**, 354-377 (2018).

- [136] M. Zhu, S. Abdollahramezani, C. Li, T. Fan, H. Harutyunyan, and A. Adibi, "Broadband-Tunable Third-Harmonic Generation Using Phase-Change Chalcogenides," *Advanced Photonics Research* **3**, 2200064 (2022).
- [137] M. Zhu, S. Abdollahramezani, C. Li, T. Fan, H. Harutyunyan, and A. Adibi, "Broadband-Tunable Third-Harmonic Generation Using Phase-Change Chalcogenides," in *CLEO: QELS_Fundamental Science*, (Optica Publishing Group, 2021), FTu1L. 7.
- [138] L. Deng, E. W. Hagley, J. Wen, M. Trippenbach, Y. Band, P. S. Julienne, J. Simsarian, K. Helmerson, S. Rolston, and W. D. Phillips, "Four-wave mixing with matter waves," *Nature* **398**, 218-220 (1999).
- [139] L. Shi, J. R. Andrade, J. Yi, M. Marinskas, C. Reinhardt, E. Almeida, U. Morgner, and M. Kovacev, "Nanoscale broadband deep-ultraviolet light source from plasmonic nanoholes," *ACS Photonics* **6**, 858-863 (2019).
- [140] M. A. Kats, R. Blanchard, P. Genevet, and F. Capasso, "Nanometre optical coatings based on strong interference effects in highly absorbing media," *Nature Materials* **12**, 20-24 (2013).
- [141] H. Liu, Z. Zhang, Z. Shang, T. Gao, and X. Wu, "Dynamically manipulating third-harmonic generation of phase change material with gap-plasmon resonators," *Optics Letters* **44**, 5053-5056 (2019).
- [142] K.-K. Du, Q. Li, Y.-B. Lyu, J.-C. Ding, Y. Lu, Z.-Y. Cheng, and M. Qiu, "Control over emissivity of zero-static-power thermal emitters based on phase-changing material GST," *Light: Science & Applications* **6**, e16194 (2017).
- [143] H. Zhang, L. Zhou, B. Rahman, X. Wu, L. Lu, Y. Xu, J. Xu, J. Song, Z. Hu, L. Xu, and J. Chen, "Ultracompact Si-GST hybrid waveguides for nonvolatile light wave manipulation," *IEEE Photonics Journal* **10**, 1-10 (2017).
- [144] P. Pitchappa, A. Kumar, S. Prakash, H. Jani, T. Venkatesan, and R. Singh, "Chalcogenide phase change material for active terahertz photonics," *Advanced Materials* **31**, 1808157 (2019).
- [145] F. Zhang, X. Xie, M. Pu, Y. Guo, X. Ma, X. Li, J. Luo, Q. He, H. Yu, and X. Luo, "Multistate switching of photonic angular momentum coupling in phase-change metadevices," *Advanced Materials* **32**, 1908194 (2020).
- [146] C. Rios, M. Stegmaier, Z. Cheng, N. Youngblood, C. D. Wright, W. H. Pernice, and H. Bhaskaran, "Controlled switching of phase-change materials by evanescent-field coupling in integrated photonics," *Optical Materials Express* **8**, 2455-2470 (2018).
- [147] O. A. M. Abdelraouf, A. P. Anthur, Z. G. Dong, H. L. Liu, Q. Wang, L. Krivitsky, X. R. Wang, Q. J. Wang, and H. Liu, "Multistate Tuning of Third Harmonic

- Generation in Fano-Resonant Hybrid Dielectric Metasurfaces," *Advanced Functional Materials* **31**, 2104627 (2021).
- [148] A. Ahmadvand, B. Gerislioglu, and N. Pala, "Optothermally controllable multiple high-order harmonics generation by Ge₂Sb₂Te₅-mediated Fano clusters," *Optical Materials* **84**, 301-306 (2018).
 - [149] R. Boyd and G. Fischer, "Nonlinear optical materials," *Encyclopedia of Materials: Science and Technology*, 6237-6244 (2011).
 - [150] C. H. Chu, M. L. Tseng, J. Chen, P. C. Wu, Y. H. Chen, H. C. Wang, T. Y. Chen, W. T. Hsieh, H. J. Wu, G. Sun, and D. P. Tsai, "Active dielectric metasurface based on phase-change medium," *Laser & Photonics Reviews* **10**, 986-994 (2016).
 - [151] P. B. Johnson and R.-W. Christy, "Optical constants of the noble metals," *Physical Review B* **6**, 4370-4379 (1972).
 - [152] L. Gao, F. Lemarchand, and M. Lequime, "Refractive index determination of SiO₂ layer in the UV/Vis/NIR range: spectrophotometric reverse engineering on single and bi-layer designs," *Journal of the European Optical Society-Rapid Publications* **8**, 13010 (2013).
 - [153] E. Gourvest, B. Pelissier, C. Vallée, A. Roule, S. Lhostis, and S. Maitrejean, "Impact of oxidation on Ge₂Sb₂Te₅ and GeTe phase-change properties," *Journal of The Electrochemical Society* **159**, H373-H377 (2012).
 - [154] F. Wang and H. Harutyunyan, "Observation of a Giant Nonlinear Chiro-Optical Response in Planar Plasmonic-Photonic Metasurfaces," *Advanced Optical Materials* **7**, 1900744 (2019).
 - [155] H. Puell, H. Scheingraber, and C. Vidal, "Saturation of resonant third-harmonic generation in phase-matched systems," *Physical Review A* **22**, 1165-1178 (1980).
 - [156] M. Zhu, S. Abdollahramezani, and A. Adibi, "Tunable third-harmonic generation using phase-change chalcogenides," in *Nonlinear Photonics*, (Optical Society of America, 2020), NpM3E. 5.
 - [157] H. Taghinejad, S. Abdollahramezani, A. A. Eftekhar, T. Fan, A. H. Hosseinnia, O. Hemmatyar, A. E. Dorche, A. Gallmon, and A. Adibi, "ITO-based microheaters for reversible multi-stage switching of phase-change materials: towards miniaturized beyond-binary reconfigurable integrated photonics," *Optics Express* **29**, 20449-20462 (2021).
 - [158] S. Abdollahramezani, O. Hemmatyar, M. Taghinejad, H. Taghinejad, A. Krasnok, A. A. Eftekhar, C. Teichrib, S. Deshmukh, M. A. El-Sayed, E. Pop, M. Wuttig, A. Alù, W. Cai, and A. Adibi, "Electrically driven reprogrammable phase-change metasurface reaching 80% efficiency," *Nature Communications* **13**, 1696 (2022).

- [159] O. Hemmatyar, S. Abdollahramezani, I. Zeimpekis, S. Lepeshov, A. Krasnok, A. I. Khan, K. M. Neilson, C. Teichrib, T. Brown, E. Pop, D. W. Hewak, M. Wuttig, A. Alù, O. L. Muskens, and A. Adibi, "Enhanced meta-displays using advanced phase-change materials," arXiv preprint **2107**, 12159 (2021).
- [160] M. Zhu, S. Abdollahramezani, and A. Adibi, "Tunable harmonic generation using hybrid metasurfaces incorporating phase-change chalcogenides," in *Laser Science*, (Optica Publishing Group, 2020), JM6A. 20.
- [161] M. Zhu, S. Abdollahramezani, C. Li, T. Fan, H. Harutyunyan, and A. Adibi, "Dynamically tunable second-harmonic generation using hybrid nanostructures incorporating phase-change chalcogenides," *Nanophotonics* **11**, 2727-2735 (2022).
- [162] Y. Ikeda, M. Miyata, and J. Takahara, "Promoted sulfurization of a single silver nanoparticle by plasmon resonance under white light illumination," *Applied Physics Express* **10**, 042001 (2017).
- [163] M. M. Fejer, G. Magel, D. H. Jundt, and R. L. Byer, "Quasi-phase-matched second harmonic generation: tuning and tolerances," *IEEE Journal of Quantum Electronics* **28**, 2631-2654 (1992).
- [164] Y. Shen, "Surface second harmonic generation: a new technique for surface studies," *Annual Review of Materials Science* **16**, 69-86 (1986).
- [165] Y. Shen, "Optical second harmonic generation at interfaces," *Annual Review of Physical Chemistry* **40**, 327-350 (1989).
- [166] G. Bautista, M. J. Huttunen, J. M. Kontio, J. Simonen, and M. Kauranen, "Third- and second-harmonic generation microscopy of individual metal nanocones using cylindrical vector beams," *Optics Express* **21**, 21918-21923 (2013).
- [167] B. Luk'yanchuk, N. I. Zheludev, S. A. Maier, N. J. Halas, P. Nordlander, H. Giessen, and C. T. Chong, "The Fano resonance in plasmonic nanostructures and metamaterials," *Nature Materials* **9**, 707-715 (2010).
- [168] G. Sartorello, N. Olivier, J. Zhang, W. Yue, D. J. Gosztola, G. P. Wiederrecht, G. g. Wurtz, and A. V. Zayats, "Ultrafast optical modulation of second- and third-harmonic generation from cut-disk-based metasurfaces," *ACS Photonics* **3**, 1517-1522 (2016).
- [169] M. Taghinejad, Z. Xu, K.-T. Lee, T. Lian, and W. Cai, "Transient second-order nonlinear media: Breaking the spatial symmetry in the time domain via hot-electron transfer," *Physical Review Letters* **124**, 013901 (2020).
- [170] F. Yi, M. Ren, J. C. Reed, H. Zhu, J. Hou, C. H. Naylor, A. C. Johnson, R. Agarwal, and E. Cubukcu, "Optomechanical enhancement of doubly resonant 2D optical nonlinearity," *Nano Letters* **16**, 1631-1636 (2016).

- [171] Z. Gong, F. Yang, L. Wang, R. Chen, J. Wu, C. P. Grigoropoulos, and J. Yao, "Phase change materials in photonic devices," *Journal of Applied Physics* **129**, 030902 (2021).
- [172] W.-M. Pan, J.-S. Li, and C. Zhou, "Switchable digital metasurface based on phase change material in the terahertz region," *Optical Materials Express* **11**, 1070-1079 (2021).
- [173] T. Cao and M. Cen, "Fundamentals and Applications of Chalcogenide Phase - Change Material Photonics," *Advanced Theory and Simulations* **2**, 1900094 (2019).
- [174] T. Cao, R. Wang, R. E. Simpson, and G. Li, "Photonic Ge-Sb-Te phase change metamaterials and their applications," *Progress in Quantum Electronics* **74**, 100299 (2020).
- [175] S. Lepeshov and A. Krasnok, "Tunable phase-change metasurfaces," *Nature Nanotechnology* **16**, 615-616 (2021).
- [176] M. Zhu, S. Abdollahramezani, T. Fan, and A. Adibi, "Dynamically tunable third-harmonic generation with all-dielectric metasurfaces incorporating phase-change chalcogenides," *Optics Letters* **46**, 5296-5299 (2021).
- [177] Y. Meng, J. K. Behera, S. Wang, M. Jiang, J. Lin, J. Wei, Y. Wang, T. Cao, and Y. Long, "Tunable Grain Orientation of Chalcogenide Film and Its Application for Second Harmonic Generation," *ACS Applied Materials & Interfaces* **12**, 29953-29958 (2020).
- [178] T. Liu, X. Fang, and S. Xiao, "Tuning nonlinear second-harmonic generation in AlGaAs nanoantennas via chalcogenide phase-change material," *Physical Review B* **104**, 195428 (2021).
- [179] M. Taghinejad, H. Taghinejad, S. T. Malak, H. Moradinejad, E. V. Woods, Z. Xu, Y. Liu, A. A. Eftekhari, T. Lian, V. V. Tsukruk, and A. Adibi, "Sharp and Tunable Crystal/Fano-Type Resonances Enabled by Out-of-Plane Dipolar Coupling in Plasmonic Nanopatch Arrays," *Annalen der Physik* **530**, 1700395 (2018).
- [180] V. V. Arsen'ev, V. S. Dneprovskii, D. N. Klyshko, and A. N. Penin, "Nonlinear absorption and limitation of light intensity in semiconductors," *Sov. Phys. JETP* **29**, 413-415 (1969).
- [181] I. Chung, J. I. Jang, C. D. Malliakas, J. B. Ketterson, and M. G. Kanatzidis, "Strongly nonlinear optical glass fibers from noncentrosymmetric phase-change chalcogenide materials," *Journal of the American Chemical Society* **132**, 384-389 (2010).

- [182] J. Jang, S. Park, C. Harrison, D. Clark, C. Morris, I. Chung, and M. Kanatzidis, "K₄GeP₄Se₁₂: a case for phase-change nonlinear optical chalcogenide," *Optics Letters* **38**, 1316-1318 (2013).
- [183] M. Zhu, S. Abdollahramezani, Y. Tang, G. Yang, C. Li, T. Fan, X. Wu, H. Harutyunyan, and A. Adibi, "Dynamically tunable all-dielectric nonlinear metasurfaces incorporating phase-change chalcogenides," in *Photonic and Phononic Properties of Engineered Nanostructures XII*, (SPIE, 2022), PC120100F.
- [184] K. Koshelev, Y. Tang, K. Li, D.-Y. Choi, G. Li, and Y. Kivshar, "Nonlinear metasurfaces governed by bound states in the continuum," *ACS Photonics* **6**, 1639-1644 (2019).
- [185] G. Yang, S. U. Dev, M. S. Allen, J. W. Allen, and H. Harutyunyan, "Optical bound states in the continuum enabled by magnetic resonances coupled to a mirror," *Nano Letters* **22**, 2001-2008 (2022).
- [186] J. Zheng, A. Khanolkar, P. Xu, S. Colburn, S. Deshmukh, J. Myers, J. Frantz, E. Pop, J. Hendrickson, J. Doylend, N. Boechler, and A. Majumdar, "GST-on-silicon hybrid nanophotonic integrated circuits: a non-volatile quasi-continuously reprogrammable platform," *Optical Materials Express* **8**, 1551-1561 (2018).
- [187] M. Zhu, S. Abdollahramezani, O. Hemmatyar, and A. Adibi, "Linear and Nonlinear Focusing Using Reconfigurable All-Dielectric Metalens Based on Phase-Change Materials," in *Laser Science*, (Optical Society of America, 2020), JW6B. 6.
- [188] N. Yu and F. Capasso, "Flat optics with designer metasurfaces," *Nature Materials* **13**, 139-150 (2014).
- [189] M. Zhu, C. Li, T. Fan, S. Abdollahramezani, X. Wu, H. Harutyunyan, and A. Adibi, "Quasibound States in the Continuum for Bidirectional Symmetry-Breaking Nonlinear Metasurfaces," in *CLEO: QELS_Fundamental Science*, (Optica Publishing Group, 2021), FTh1M. 4.
- [190] A. Efimov, A. J. Taylor, F. G. Omenetto, J. C. Knight, W. J. Wadsworth, and P. S. J. Russell, "Phase-matched third harmonic generation in microstructured fibers," *Optics Express* **11**, 2567-2576 (2003).
- [191] J. Nold, P. Hölzer, N. Joly, G. Wong, A. Nazarkin, A. Podlipensky, M. Scharrer, and P. S. J. Russell, "Pressure-controlled phase matching to third harmonic in Ar-filled hollow-core photonic crystal fiber," *Optics Letters* **35**, 2922-2924 (2010).
- [192] R. Lemasters, M. R. Shcherbakov, G. Yang, J. Song, T. Lian, H. Harutyunyan, and G. Shvets, "Deep optical switching on subpicosecond timescales in an amorphous Ge metamaterial," *Advanced Optical Materials* **9**, 2100240 (2021).

- [193] M. Semmlinger, M. Zhang, M. L. Tseng, T.-T. Huang, J. Yang, D. P. Tsai, P. Nordlander, and N. J. Halas, "Generating third harmonic vacuum ultraviolet light with a TiO₂ metasurface," *Nano Letters* **19**, 8972-8978 (2019).
- [194] M. V. Rybin, K. L. Koshelev, Z. F. Sadrieva, K. B. Samusev, A. A. Bogdanov, M. F. Limonov, and Y. S. Kivshar, "High-Q supercavity modes in subwavelength dielectric resonators," *Physical Review Letters* **119**, 243901 (2017).
- [195] P. Moitra, B. A. Slovick, W. Li, I. I. Kravchenko, D. P. Briggs, S. Krishnamurthy, and J. Valentine, "Large-scale all-dielectric metamaterial perfect reflectors," *ACS Photonics* **2**, 692-698 (2015).
- [196] S.-D. Liu, Z.-X. Wang, W.-J. Wang, J.-D. Chen, and Z.-H. Chen, "High Q-factor with the excitation of anapole modes in dielectric split nanodisk arrays," *Optics Express* **25**, 22375-22387 (2017).
- [197] Y. Kivshar, "All-dielectric meta-optics and non-linear nanophotonics," *National Science Review* **5**, 144-158 (2018).
- [198] F. Bassani and V. Lucarini, "General properties of optical harmonic generation from a simple oscillator model," *Il Nuovo Cimento D* **20**, 1117-1125 (1998).
- [199] C. W. Hsu, B. Zhen, J. Lee, S.-L. Chua, S. G. Johnson, J. D. Joannopoulos, and M. Soljačić, "Observation of trapped light within the radiation continuum," *Nature* **499**, 188-191 (2013).
- [200] H. Friedrich and D. Wintgen, "Interfering resonances and bound states in the continuum," *Physical Review A* **32**, 3231-3242 (1985).
- [201] Y. Yang, C. Peng, Y. Liang, Z. Li, and S. Noda, "Analytical perspective for bound states in the continuum in photonic crystal slabs," *Physical Review Letters* **113**, 037401 (2014).
- [202] D. Marinica, A. Borisov, and S. Shabanov, "Bound states in the continuum in photonics," *Physical Review Letters* **100**, 183902 (2008).
- [203] S. Weimann, Y. Xu, R. Keil, A. E. Miroshnichenko, A. Tünnermann, S. Nolte, A. A. Sukhorukov, A. Szameit, and Y. S. Kivshar, "Compact surface Fano states embedded in the continuum of waveguide arrays," *Physical Review Letters* **111**, 240403 (2013).
- [204] S. Joseph, S. Pandey, S. Sarkar, and J. Joseph, "Bound states in the continuum in resonant nanostructures: an overview of engineered materials for tailored applications," *Nanophotonics* **10**, 4175-4207 (2021).
- [205] E. Bulgakov and A. Sadreev, "Formation of bound states in the continuum for a quantum dot with variable width," *Physical Review B* **83**, 235321 (2011).

- [206] C. Fang, Q. Yang, Q. Yuan, X. Gan, J. Zhao, Y. Shao, Y. Liu, G. Han, and Y. Hao, "High-Q resonances governed by the quasi-bound states in the continuum in all-dielectric metasurfaces," *Opto-Electronic Advances* **4**, 200030 (2021).
- [207] Y. He, G. Guo, T. Feng, Y. Xu, and A. E. Miroshnichenko, "Toroidal dipole bound states in the continuum," *Physical Review B* **98**, 161112 (2018).
- [208] I. S. Sinev, K. Koshelev, Z. Liu, A. Rudenko, K. Ladutenko, A. Shcherbakov, Z. Sadrieva, M. Baranov, T. Itina, J. Liu, A. A. Bogdanov, and Y. Kivshar, "Observation of ultrafast self-action effects in quasi-BIC resonant metasurfaces," *Nano Letters* **21**, 8848-8855 (2021).
- [209] M. Gandolfi, A. Tognazzi, D. Rocco, C. De Angelis, and L. Carletti, "Near-unity third-harmonic circular dichroism driven by a quasibound state in the continuum in asymmetric silicon metasurfaces," *Physical Review A* **104**, 023524 (2021).
- [210] D. Milošević, "High-order harmonic generation by a bichromatic elliptically polarized field: conservation of angular momentum," *Journal of Physics B: Atomic, Molecular and Optical Physics* **48**, 171001 (2015).
- [211] E. A. A. Pogna, M. Celebrano, A. Mazzanti, L. Ghirardini, L. Carletti, G. Marino, A. Schirato, D. Viola, P. Laporta, and C. De Angelis, "Ultrafast, all optically reconfigurable, nonlinear nanoantenna," *ACS Nano* **15**, 11150-11157 (2021).
- [212] H. Fukuda, K. Yamada, T. Shoji, M. Takahashi, T. Tsuchizawa, T. Watanabe, J.-i. Takahashi, and S.-i. Itabashi, "Four-wave mixing in silicon wire waveguides," *Optics Express* **13**, 4629-4637 (2005).
- [213] M. Zandehshahvar, Y. Kiarashi, M. Chen, R. Barton, and A. Adibi, "Inverse design of photonic nanostructures using dimensionality reduction: reducing the computational complexity," *Optics Letters* **46**, 2634-2637 (2021).
- [214] K. Weiss, S. Riedel, S. Schulz, M. Schwerd, H. Helneder, H. Wendt, and T. Gessner, "Development of different copper seed layers with respect to the copper electroplating process," *Microelectronic Engineering* **50**, 433-440 (2000).

VITA

Muliang Zhu received his B.S. degree in Applied Physics from the University of Science and Technology of China in 2014. Later, he received M.S. degrees in Electrical & Computer Engineering and in Industrial Engineering from Georgia Institute of Technology in 2017 and 2022, respectively. He is currently pursuing his Ph.D. degree in Electrical & Computer Engineering at Georgia Institute of Technology, focusing on the development of a CMOS-compatible reconfigurable nonlinear photonic metamaterial platform based on phase-change materials and silicon. He is also interested in machine learning assisted design of the hybrid platform. He was a recipient of Center for Research into Novel Computing Hierarchies (CRNCH) Ph.D. Fellowship from Georgia Institute of Technology in 2020. He has authored and co-authored more than 30 works in prestigious journals and international conferences in the areas of optics, materials science, and machine learning, including 13 first-authored works.